LOCALIZATION OF PEOPLE USING RECEIVED SIGNAL STRENGTH MEASUREMENTS IN WIRELESS SENSOR NETWORKS

by

Yang Zhao

A dissertation submitted to the faculty of
The University of Utah
in partial fulfillment of the requirements for the degree of

Doctor of Philosophy

Department of Electrical and Computer Engineering

The University of Utah

December 2012

The University of Utah Graduate School

STATEMENT OF DISSERTATION APPROVAL

The dissertation of **Yang Zhao**

has been approved by the following supervisory committee members:

Neal Patwari	, Chair	**8/14/2012** Date Approved
Cynthia Furse	, Member	**8/14/2012** Date Approved
Sneha Kasera	, Member	**8/14/2012** Date Approved
Tolga Tasdizen	, Member	**8/14/2012** Date Approved
Thomas Schmid	, Member	**8/14/2012** Date Approved

and by **Gianluca Lazzi** , Chair of

the Department of **Electrical and Computer Engineering**

and by Charles A. Wight, Dean of The Graduate School.

ABSTRACT

Location information of people is valuable for many applications including logistics, healthcare, security and smart facilities. This dissertation focuses on localization of people in wireless sensor networks using radio frequency (RF) signals, specifically received signal strength (RSS) measurements. A static sensor network can make RSS measurements of the signal from a transmitting badge that a person wears in order to locate the badge. We call this kind of localization method radio device localization. Since the human body causes RSS changes between pairwise sensor nodes of a static network, we can also use RSS measurements from pairwise nodes of a network to locate people, even if they are not carrying any radio device. We call this device-free localization (DFL).

The first contribution of this dissertation is to radio device localization. The human body has a major effect on the antenna gain pattern of the transmitting badge that the person is wearing, however, existing research on device localization ignores this effect. In this work, the gain pattern due to the effect of the human body is experimentally measured and represented by a first-order gain pattern model. A method is presented to estimate the model parameters from multiple received signal strength (RSS) measurements. An alternating gain and position estimation (AGAPE) algorithm is proposed to jointly estimate the orientation and the position of the badge using RSS measurements at known-position anchor nodes. Lower bounds on mean squared error (MSE) and experimental results are presented that both show that the accuracy of position estimates can be greatly improved by including orientation estimates in the localization system. Finally, a new tracking filter that accepts orientation estimates as input is developed, which is called the orientation-enhanced extended Kalman filter (OE-EKF). Experimental results show that this new method using the localization estimates from AGAPE algorithm improves tracking accuracy in radio device localization systems.

In the field of DFL, this dissertation has two major contributions: (1) improving the robustness of variance-based DFL methods that can locate human motion; (2) developing a new DFL system that is capable of locating both moving and stationary people without using "empty-room" offline calibration. For the first contribution, two robust estimators for variance-based radio tomographic imaging (VRTI) – subspace variance-based radio tomography (SubVRT), and least squares variance-based radio tomography (LSVRT) are proposed. Human motion in the vicinity of a wireless link causes variations in the link received signal strength (RSS). DFL systems, such as VRTI, use these RSS variations in a static wireless network to locate and track people in the area of the network. However, intrinsic motion, such as branches moving in the wind and rotating or vibrating machinery, also causes RSS variations which degrade the performance of a localization system. The first robust estimator SubVRT uses subspace decomposition, and the second estimator LSVRT uses a least squares formulation on the "empty-room" calibration measurements. Experimental results show that both estimators reduce localization root mean squared error by about 40% compared to VRTI. In addition, the Kalman filter tracking results from both estimators are more robust to large errors compared to tracking results from VRTI. The second contribution in DFL is a new localization system, which we call kernel distance-based radio tomographic imaging (KRTI). Since many DFL systems including VRTI cannot locate stationary people, we present and evaluate a system that can locate stationary and moving people, with or without calibration, by quantifying the difference between two histograms of signal strength measurements. From five experiments, we show that our KRTI localization system performs better than the state-of-the-art device-free localization systems in different non-line-of-sight environments.

CONTENTS

CHAPTERS

3. ROBUST ESTIMATORS FOR VARIANCE BASED DEVICE-FREE LOCALIZATION 47

4. HISTOGRAM DIFFERENCE-BASED DEVICE-FREE LOCALIZATION 77

LIST OF FIGURES

LIST OF TABLES

ACKNOWLEDGMENTS

This work would not have been possible without the support and help of my advisor Neal Patwari. I am very lucky to have met him during his localization experiments when I was admitted into the Electrical and Computer Engineering Department. His original device-free localization idea is so interesting to me that I cannot wait to start doing research on this topic. I have been given all the support and guidance I need since then. Every paper I publish contains thorough edits from him. I have learned not only knowledge and skills from him, but also attitude and style of doing serious research.

I am also lucky to have four other professors from my department and the School of Computing on my committee. They are world-class researchers on the electromagnetic field, computer networking, image processing, and embedded systems. They gave me classic papers to study for my PhD qualifying exam. They also gave me opportunities to review the latest top-tier journal papers. Without their help, my PhD process would not have gone so smoothly. I am also thankful to Michael Zhdanov from the Geology and Geophysics Department. I benefitted from his Inversion Theory class.

Another mentor for me is my “academic brother” Joey Wilson. He taught me all the basic expertise I needed so that I could quickly start working on a new research topic. He has great passion on open source and state-of-the-art technology, which greatly influenced and motivated me during my research. I also learned a lot from Jessica Croft, Dustin Maas and other colleagues of the department.

I also had the opportunity to collaborate and work with people from other departments, universities and research labs. In particular, I would like to thank Michael Rabbat from McGill University for his discussions and edits on my first PhD paper. I would like to thank Jeff Phillips from the School of Computing for providing an excellent mathematical tool to measure histogram difference. I am also thankful to Koji Yatani and Desney Tan for offering me a research intern position in Microsoft Research Asia.

Finally, I am very grateful to my parents. Without their support and encouragement, I would not be able to take and pass the expensive and tedious GRE and TOEFL tests, and I would not have had the opportunity to go abroad for my PhD study in the first place.

CHAPTER 1

INTRODUCTION

Wireless communication devices have become increasingly small, low-cost and common in recent years due to the advances in radio, micro-electronic and embedded system technologies. People have imagined to network thousands or tens of thousands of wireless devices together for numerous applications. The concepts of “ubiquitous computing,” “smart dust” and “wireless sensor network” are representative examples of this imagination, which have been studied extensively in academia, and which are gradually becoming developed into products in industry.

Wireless sensor networks have potential applications ranging from environmental and industrial monitoring to medical applications, smart home and facilities. For example, a network of various gas sensors can be used to monitor air pollution and send monitoring data wirelessly to a data processing center. As another example, a wireless sensor network deployed in a hospital tracks different medical equipment with radio frequency identification (RFID) tags attached for logistic purposes. Localization is one of the most important techniques for applications such as elder care, security and smart facilities [2, 3, 4]. Knowing the location information of people has significant benefits for these applications. For example, we would like to know where a physician or a patient is in a hospital. In rescue scenarios, one of the most important tasks is to find the locations of victims. While for some scenarios, we can expect people to participate in the localization system by wearing a device that can be used to locate them; for many scenarios, we cannot expect people to carry any device, such as in the rescue scenario or the intruder detection scenario.

This dissertation investigates localization of a person who is, or is not carrying a radio device, using a wireless sensor network. When people carry devices, such as mobile phones or RFID badges, human sensing and localization can be achieved by using extrinsic traits defined as traits from objects and devices carried by a person. Besides extrinsic traits, intrinsic traits of people that arise from human activity or human presence can also be used to sense and locate people. Before discussing these two different sensing and localization methods, the terms *sensor*, *localization* and *people* are first explained to define the generality of the problem in this dissertation.

First, we use standard radio devices for sensing purposes; thus *sensor* in "wireless sensor network" means commercially available off-the-shelf radio sensor. The radio sensor essentially requires only a radio transceiver plus a microcontroller for memory storage and simple processing. For example, TelosB mote [5] with a radio transceiver chip CC2420 and a microcontroller Texas Intruments (TI) MSP430 is used in many experiments in this dissertation. Also used in this dissertation is TI's USB dongle node with a system-on-chip CC2531 which integrates the functions of radio transceiver and microcontroller [6]. A wireless sensor network is composed by many such simple radio sensors, and we call them "nodes" of a network. To organize and collect data from these nodes, each node is programmed with a token passing protocol called "Spin" [7] in this dissertation.

Second, *localization* is the process of estimating the location of certain object, that is, the spatial coordinates of an object from certain measurements and certain models. We know that no measurements are perfectly accurate. For example, instrument noise exists for all kinds of measurements made by different instruments. As another example, electronic devices are affected by thermal noise. Physical models come from our observations and measurements of certain phenomena, and usually involve simplifications so that we can use mathematical tools to quantitatively describe physical variables that we are interested. In many situations, we can only use statistical models to quantify variables due to the complexity of the real-world phenomena. Thus, a localization problem is essentially an estimation problem using imperfect measurements and models. In this dissertation, we use radio signal strength measurements and statistical models to solve localization problems in a 2-D network area. All work presented in the dissertation could be extended to localization in a 3-D domain, however, that is not the focus of this dissertation.

For locating a person wearing certain radio devices, we use the received signal strength (RSS) measurements received by all sensor nodes from the device and a statistical path loss model to relate RSS with distance. We call this kind of localization "radio device localization" in this dissertation. An illustration of radio device localization is shown in Figure 1.1. The locations of all network nodes are assumed known, thus they are often called "reference nodes" or "anchor nodes." In this dissertation, we use the term anchor nodes to be consistent. For localization of people without carrying any radio devices, we use pairwise RSS measurements from all anchor nodes in a network. Since all nodes communicate with each other, a wireless mesh network is formed covering an area, as shown in Figure 1.2.

A person “disturbs” the pairwise RSS between each two nodes, and we use the changes of all pairwise RSS measurements from a network to infer the location of the person. Since the person does not need to carry any device, we call this kind of localization “device-free localization.”

Finally, this dissertation focuses on localization of *people*. While both radio device localization and device-free localization methods presented in this dissertation may be applied to locate objects like hospital equipment, we focus our attention particularly on people in this dissertation. We perform measurements to quantify the effects of the human body on RSS, and we perform experiments to locate people walking or standing motionlessly at different environments. Although all the methods presented in the dissertation are capable of locating multiple people in a sensor network, we focus on localization of a single person here.

To summarize, this dissertation focuses on estimating the location of a single person with or without carrying any radio sensor using statistical models and standard RSS measurements. The traditional radio device localization and the emerging device-free localization techniques are discussed in details next in Section 1.1. Then, the contributions of this dissertation are presented in Section 1.2. Finally, the outline of the dissertation is listed in Section 1.3.

1.1 Radio frequency localization techniques

Many sensor techniques can be used in localization of people, such as the optical camera, infrared sensor, acoustic sensor, etc. However, one common disadvantage of these sensor techniques is they are limited in line-of-sight conditions, that is, these sensing methods cannot penetrate obstacles such as walls. This dissertation is focused on RF techniques. In particular, we use standard radio nodes to sense the environment and to locate either a node worn by a person or a person without wearing any radio node. We discuss radio device localization and device-free localization in this section.

1.1.1 Radio device localization

The traditional radio device localization techniques use various measurements from radio devices for localization. Specifically, angle-of-arrival (AOA) and distance related measurements are often used in radio device localization [8]. The accuracy of AOA measurements is limited by factors such as the directivity of the antenna, the shadowing and multipath effect. Distance related measurements include one-way or roundtrip time-of-arrival (TOA) measurements, time-difference-of-arrival (TDOA) measurement and received signal strength

(RSS) measurement. While both TOA and TDOA measurements require accurate clocks and time synchronization, RSS measurement is a standard feature in most wireless devices, it does not require a highly accurate clock as required by TOA and TDOA, and requires no additional hardware like antenna array for AOA measurements.

This dissertation focuses on using RSS measurements in localization. People often use another term, "received signal strength indicator" (RSSI), which is an indication of the power level of RF signal received by the antenna. According to IEEE 802.11 standard [9], "RSSI is intended to be used in a relative manner," and has a integer value of 0 through a maximum number. Since the 802.11 standard does not define any relationship between RSSI value and RSS in dBm, wireless device manufacturers provide their own relationship. In this dissertation, we use RSS to represent received power level in dBm.

For RSS-based localization, there are generally two categories of localization methods: model-based and fingerprint-based methods. Fingerprint-based methods are also called RSS profiling [8]. It requires a radio map to be built by a person carrying a radio device at each possible location before the real-time localization operation. This map-building is called the offline training period, when all RSS measurements from links between the radio device and all anchor nodes in a network (shown as the dash lines in Figure 1.1) are recorded. Then during the online localization period, the new RSS measurements from all those links are compared with the radio map, and the location with the closest matching of RSS is chosen as the localization result. The fingerprint-based method requires extensive effort in building a radio map during the training period.

The model-based method provides an alternative. The basic idea is to relate the RSS measurement with the distance between a transmitter (TX) and a receiver (RX) based on certain statistical model. Then, certain estimation method like maximum likelihood estimation (MLE) is used to locate the radio transmitter from RSS measurements between the transmitter and all anchor nodes of a network [10]. A general model for the dBm power P_i received at anchor node i from a transmitter t, is the log-distance model [11]:

$$P_i = \Pi_0 - 10 n_p \log_{10}\left(\frac{d_i}{d_0}\right) + \zeta \tag{1.1}$$

where Π_0 is the received power in dBm at a reference distance d_0, n_p is the pathloss exponent, $d_i = \|\mathbf{z}_i - \mathbf{z}_t\|$ is the distance between anchor node i at coordinate $\mathbf{z}_i$ and transmitter badge t at coordinate $\mathbf{z}_t$, and ζ includes the model error plus measurement noise including the multipath effect. Note that for previous model-based methods, it is assumed that the antenna gain pattern is isotropic, that is, the radiation pattern of the antenna is assumed to be uniform in all directions. The isotropic antenna gain pattern is an over-simplified assumption, and this dissertation shows the research progress in removing this unrealistic assumption to improve localization accuracy.

In summary, this dissertation focuses on model-based RSS localization of a person wearing an active RFID badge. An illustration of such radio device localization is shown in Figure 1.1. RSS measurements between the RFID badge and all anchor nodes of a network are used to estimate the distances from the badge to anchor nodes from a certain model such as 1.1, and the distance estimates from RSS measurements are further used to infer the location of the RFID badge. Chapter 2 discusses the details of the radio device localization, and all symbols used in Chapter 2 and their meanings are listed in Table 1.4.

1.1.2 Device-free localization

An emerging localization technique is to use radio signal changes caused by human body to locate people who do not carry any radio devices [12, 13, 14, 15]. Since this new technique does not require people to wear any devices, people call it "device-free localization" [16], "passive localization" [14], or "sensorless sensing" [17]. In this dissertation, the term device-free localization (DFL) is used.

Like radio device-based localization, different RF measurements can be used in DFL. Ultra-wideband (UWB) measurements including the amplitude, time delay and phase of the radio signal can be used to infer the properties of a static environment and changes in the environment caused by moving people or objects. However, the UWB equipments are usually expensive, and are primarily used in military applications today. RSS measurements provide an alternative, they are inexpensive and available in standard wireless devices. Different RSS-based DFL studies have achieved localization results with surprising accuracy [14, 18, 15].

For these RSS-based DFL methods, there are two categories: fingerprint-based methods and model-based methods. Like fingerprint-based radio device localization methods, a radio map needs to be built on a training period before the real-time operation. During the training period, RSS measurements are recorded on all links in a network as a person stands in a known position, which becomes a fingerprint for a person being at that location. Fingerprints are recorded as the person is moved to each possible position in the environment. During real-time operation, the current RSS measurement is compared to all of the fingerprints, and the person is estimated to be at the position with the closest matching fingerprint [19, 20, 21].

In this dissertation, we focus on model-based DFL methods, which we also call "radio tomographic localization." The advantage of model-based methods, such as those reported in [22, 15, 23, 24, 25, 26] is that these methods do not require training, in which a person needs to stand at each possible location in an area. These methods use an elliptical model to relate people's location to different forms of RSS measurements $\mathbf{y}$. For example, [22] use the model to relate the location of a person with the absolute RSS changes from an "empty-room" calibration, in which no people are present in the network area. The model is based on the fact that if a person stands inside an elliptical area covered by a link between two nodes, the person has certain effect on the RSS link measurement; otherwise, there is no effect from the person. The model relating $\mathbf{y}$ with the image $\mathbf{x}$ that represents either human presence or human motion in an area is written as:

$$\mathbf{y} = W\mathbf{x} + \mathbf{n} \tag{1.2}$$

where $\mathbf{n}$ is an $L \times 1$ noise vector including model error and measurement noise, and W is an $L \times P$ matrix representing the weighting of each voxel in $\mathbf{x}$ on each link measurement. The model expressed in W is formulated as:

$$W_{l,p} = \frac{1}{\sqrt{d_{i_l,j_l}}} \begin{cases} \phi & \text{if } d_{i_l,p} + d_{j_l,p} < d_{i_l,j_l} + d_w \\ 0 & \text{otherwise} \end{cases} \tag{1.3}$$

where d_{i_l,j_l} is the Euclidean distance between two sensors i_l, j_l on link l located at $\mathbf{z}_{s,i_l}$ and $\mathbf{z}_{s,j_l}$; $d_{j_l,p}$ is the Euclidean distance between sensor j_l and $\mathbf{z}_p$, the center coordinate of voxel p; $d_{i_l,p}$ is the Euclidean distance between sensor i_l and voxel p; d_w is a tunable parameter controlling the ellipse width, and ϕ is a constant scaling factor.

For different radio tomographic localization methods, $\mathbf{y}$ represents different forms of RSS measurements. For example, in shadowing-based RTI [22], $\mathbf{y}$ represent the absolute RSS change from the empty-room calibration measurement. For variance-based RTI [15], it represents the RSS variance. For SubVRT [23] and LSVRT [27] discussed in Chapter 3, $\mathbf{y}$ is the RSS variance caused by extrinsic motion, which is defined as motion of people that enter and leave the environment. RSS variance caused by intrinsic motion defined as the motion of objects that are intrinsic parts of the environment is treated as noise, and not included in $\mathbf{y}$. For histogram difference-based RTI [28] discussed in Chapter 4, $\mathbf{y}$ is certain histogram difference metric such as kernel distance [29] between two RSS histograms.

Once we have the model W and certain forms of RSS measurements $\mathbf{y}$, a radio tomographic image $\hat{\mathbf{x}}$ can be estimated by solving an inverse problem, that is, estimate $\mathbf{x}$ given $\mathbf{y}$ and W. Since we focus on single person localization in this dissertation, from the radio tomographic image estimate $\hat{\mathbf{x}}$, the position of the person is estimated as the center coordinate of the pixel with maximum value. That is,

$$\hat{\mathbf{z}} = \mathbf{r}_q \quad \text{where} \quad q = \arg\max_p \hat{x}_p$$

where $\hat{x}_p$ is the pth element of vector $\hat{\mathbf{x}}$. For convenience, different notations used in Chapters 3 and 4 of this dissertation are included in Tables 1.5 and 1.6.

1.2 Contributions

This dissertation has contributions in both radio device localization and device-free localization. For radio device localization, most previous methods make the assumption that transmitter badges attached to objects or carried by people have isotropic gain patterns. However, even when a transmitter badge has an antenna that is considered isotropic, the person or object has considerable effect on the badge's radiation pattern. The major contribution of this work in radio device localization is to develop models and methods to handle, and in fact benefit from, the removal of the unrealistic isotropic gain pattern assumption. Specifically, the gain pattern of transmitter antenna due to the effect of the human body is experimentally measured and represented by a first-order model. An alternating gain and position estimation (AGAPE) algorithm is proposed to jointly estimate the orientation and the position of the badge using RSS measurements at known-position anchor nodes. Lower bounds on mean squared error (MSE) and experimental results both show that the accuracy of position estimates can be greatly improved by including orientation estimates in the localization system. Finally, a new extended Kalman filter that accepts orientation estimates as input is developed for tracking people.

For device-free localization (DFL), this dissertation has two major contributions. First, variance-based radio tomographic localization is found to be sensitive to all kinds of motion including intrinsic motion and extrinsic motion. Intrinsic motion is defined as motion from objects that are intrinsic part of the environment, while extrinsic motion is the motion from people or objects that enter and leave the environment. When the impact of the intrinsic motion is stronger than that of the extrinsic motion, the previous method in [15] does not work. Two robust estimators are proposed that use "empty-room" calibration measurements to capture the effect of intrinsic motion and then to remove or reduce its impact. The second contribution in the area of DFL is a new radio tomographic localization method which uses the histogram difference between two RSS histograms to locate people. Not like the earth mover's distance, which involves solving a transportation optimization problem, the kernel distance directly compares the difference between two histograms smoothed by a kernel function, so it can be calculated much faster and is preferred for a real-time application like RTI. The new method, called kernel distance-based radio tomographic imaging (KRTI), is capable of locating both moving and stationary people in multipath-rich environments. In addition, simple filtering of online RSS measurements allows one to keep a long-term histogram in memory without significant computational complexity, and also enables online calibration instead of offline empty-room calibration.

To summarize, the work presented in this dissertation has contributions in both radio device localization and device-free localization. The contributions are classified into the following categories, and listed below together with the reporting publication reference numbers and chapter numbers in this dissertation.

- **Observations**: Observe the bias of active RFID badge localization with isotropic gain pattern assumption ([1] and Chapter 2). Observe how intrinsic motion, such as motion of tree leaves, increases RSS variation in a way that is "noise" to a variance-based DFL system, and discover the noise has a spatial signature, which can be removed by the subspace decomposition method ([23] and Chapter 3).

- **Measurements**: Perform experiments at different environments to measure the effect of the orientation (facing direction) of a human body on the RSS from a transmitter badge worn by a person ([1] and Chapter 2). Perform experiments at indoor and outdoor environments to study the performance of different DFL methods ([23, 30, 31] and Chapters 3 and 4).

- **Model**: Based on the measurements, propose a first-order model to quantify the human body effect on the gain pattern of an RFID transmitter ([1] and Chapter 2).

- **Theory**: Derive the Bayesian Cramér-Rao bound (CRB) [32] for the joint estimation problem. Comparison with CRB derived with an isotropic gain pattern assumption [10] shows that the accuracy of position estimates can be greatly improved by including orientation estimates in the localization system ([1] and Chapter 2).

- **Signal processing algorithms**: Develop an alternating gain and position estimation (AGAPE) algorithm [1] to jointly estimate RFID badge location and badge gain pattern ([1] and Chapter 2). Develop a robust tracking algorithm, orientation-enhanced extended Kalman filter (OE-EKF) that accepts orientation estimate as input to track people wearing RFID badges in RF sensor networks ([1] and Chapter 2).

- **Statistical signal processing methods**: Propose two robust estimators, subspace variance-based radio tomography (SubVRT) [23] and least square variance-based radio tomography (LSVRT) [30] to reduce the impact of noise caused by intrinsic motion ([23], [30] and Chapter 3).
- **System**: Propose a new device-free localization system called kernel distance-based RTI (KRTI) [31], which uses the kernel distance between two RSS histograms (short-term histogram and long-term histogram) to locate both moving and stationary people. Propose to use exponentially weighted moving average (infinite impulse response filter) on long-term histogram built during online period so that KRTI does not require "empty-room" offline calibration, and can be implemented without much computational complexity ([31] and Chapter 4).
- **Demonstration**: Demonstrate the real-time implementation of SubVRT ([33] and Chapter 3) and KRTI ([28] and Chapter 4).

Two journal papers (one published and the other submitted), two conference papers (one published and the other in review), two demo abstracts and one technical report have resulted from this work. The names and reference numbers of these publications are listed as follows:

- Y. Zhao, N. Patwari, P. Agrawal, and M. G. Rabbat, "Directed by directionality: Benefiting from the gain pattern of active RFID badges," IEEE Transactions on Mobile Computing, vol. 11, pp. 865-877, May 2012. ([1])
- Y. Zhao and N. Patwari, "Noise reduction for variance-based device-free localization and tracking," in Proc. of the 8th IEEE Conf. on Sensor, Mesh and Ad Hoc Communications and Networks (SECON'11), Salt Lake City, Utah, U.S., June 2011 (acceptance rate: 27%). ([23])
- Y. Zhao and N. Patwari, "Demo abstract: Noise reduction for variance-based radio tomographic localization," in Proc. of the 8th IEEE Conf. on Sensor, Mesh and Ad Hoc Communications and Networks (SECON'11), Salt Lake City, Utah, U.S., June 2011. ([33])
- Y. Zhao and N. Patwari, "Robust estimators for variance-based device-free localization and tracking," Tech. Rep. arXive:1110.1569v1, Arxiv.org, Oct. 2011. ([27])
- Y. Zhao and N. Patwari, "Robust estimators for variance-based tag-free localization and tracking," IEEE Transactions on Signal Processing, Jan. 2012 (submitted). ([30])

- Y. Zhao and N. Patwari, "Demo abstract: Histogram distance-based radio tomographic localization," in Proc. of the 11th International Conference on Information Processing in Sensor Networks (IPSN'12), Beijing, China, April, 2012. ([28])
- Y. Zhao, N. Patwari, J. M. Phillips, and S. Venkatasubramanian, "Radio tomographic imaging and tracking of stationary and moving people via histogram difference," the 8th International Conference on emerging Networking EXperiments and Technologies (CoNEXT), June 2012 (submitted). ([31])

1.3 Outline of the dissertation

After this introduction chapter, the details of contributions of this work are presented in the following three chapters. Chapter 2 includes all work on radio based localization. A first-order model is proposed to quantify the effect of the facing direction of a human body on RSS based on results from a measurement campaign. Then the AGAPE algorithm is proposed to jointly estimate the location of a transmitter and the gain pattern of the antenna. Also included in this chapter is the Bayesian CRB, the orientation enhanced Kalman filter and experimental results. Chapter 3 discusses the improvement of variance-based DFL methods. Two robust estimators, SubVRT and LSVRT, are discussed in detail in this chapter. The new DFL method, kernel distance-based RTI, is presented in Chapter 4, and all DFL methods to date are compared. In each of the above three chapters, different experiments are performed to evaluate the performance of proposed methods. The names and descriptions of these experiments in each chapter are summarized in Tables 1.1, 1.2 and 1.3. Finally, Chapter 5 concludes this dissertation. The research contributions are summarized, and topics for future research are discussed.

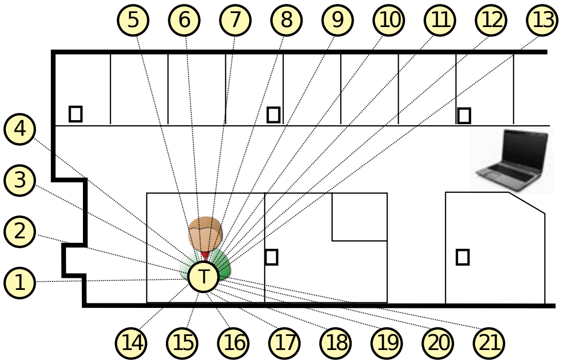

Figure 1.1: Illustration of radio device localization of a person in a sensor network.

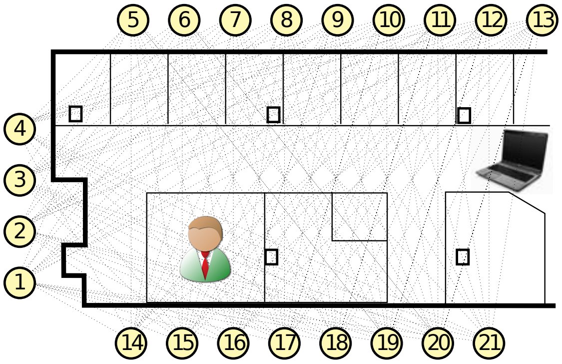

Figure 1.2: Illustration of device-free localization of a person in a sensor network.

Table 1.1: Experiments used in Chapter 2 (first reported in [1]).

Experiment name	Description
Experiment 1	Outdoor experiment with a square path
Experiment 2	Outdoor experiment with a rectangular path
Experiment 3	Outdoor experiment with a square path

Table 1.2: Experiments used in Chapter 3.

Experiment name	Description
Experiment 1	Through-wall experiment reported in [15]
Experiment 2	Through-wall experiment reported in [23]

Table 1.3: Experiments used in Chapter 4.

Experiment name	Description
Experiment 1	Through-wall experiment reported in [16]
Experiment 2	Through-wall experiment reported in [15]
Experiment 3	Through-wall experiment reported in [31]
Experiment 4	Through-wall experiment reported in [31]
Experiment 5	Indoor experiment reported in [16]

Table 1.4: Symbols used in Chapter 2.

Symbol	Meaning
P_i	Received power at anchor node i from the transmitter badge
d_i	Distance between anchor node i and the transmitter badge
n_p	Pathloss exponent
Π_0	Received power in dBm at a reference distance d_0
η	Model error plus noise in the log-distance and gain pattern model
α_i	Angle between anchor node i and the transmitter badge
$g(\alpha_i)$	Gain pattern of the transmitter badge at angle α_i
G_1	Directionality of the gain pattern
$G(k)$	Complex-valued the kth Fourier series component of $g(\alpha)$
β	Orientation of the transmitter badge
N	Number of RSS measurements received from the transmitter badge
$\mathbf{z}_t$	True location of a transmitter badge
$\hat{\mathbf{z}}$	Location estimate of a person or a badge
$\mathbf{s}$	State vector of the Kalman filter
$\mathbf{x}$	Measurement vector of the Kalman filter
$\mathbf{w}$	Measurement noise of the Kalman filter
$\mathbf{u}$	Process noise of the Kalman filter

Table 1.5: Symbols used in Chapter 3.

Symbol	Meaning
L	Number of directional links of a network
P	Number of pixels of a network area
N	Number of radio nodes of a network
m	Length of the window of a windowed variance
$s_{l,t}$	RSS measurement from link l at time t
$y_{l,t}$	RSS variance from link l at time t
$\mathbf{x}$	Vector of human motion
$\mathbf{y}_r$	Vector of L link measurements in real-time operation
$\mathbf{y}_c$	Vector of L link measurements in offline calibration
$\hat{\mathbf{y}}$	Intrinsic signal component of $\mathbf{y}$
$\tilde{\mathbf{y}}$	Extrinsic signal component of $\mathbf{y}$
$\mathbf{z}$	True location of a person
$\hat{\mathbf{z}}$	Location estimate of a person
$\mathbf{z}_{s,i_l}$	Location of sensor node i_l of link l
$\mathbf{n}$	Measurement noise plus intrinsic motion
σ_x^2	Variance of human motion
α	Regularization parameter
Q	Tikhonov matrix
k	Numbers of principal components
$\mathbf{s}$	State vector of the Kalman filter
$\mathbf{r}$	Measurement vector of the Kalman filter
$\mathbf{v}$	Measurement noise of the Kalman filter
$\mathbf{w}$	Process noise of the Kalman filter
σ_w^2	Process noise parameter in the Kalman filter
σ_v^2	Measurement noise parameter in the Kalman filter

Table 1.6: Symbols used in Chapter 4.

Symbol	Meaning
$\mathbf{h}^n$	RSS histogram at time n
y^n	RSS measurement at time n
$\mathbf{p}$	Short-term histogram
$\mathbf{q}$	Long-term histogram
L	Number of directional links of a network
M	Number of pixels of a network area
N	Number of RSS measurements in a histogram $\mathbf{h}$
β	Forgetting factor of the exponentially weighted moving average
$\mathbf{x}$	Vector of human presence
$\mathbf{d}$	Vector of histogram difference from L links
$\mathbf{z}$	True location of a person
$\hat{\mathbf{z}}$	Location estimate of a person
$\mathbf{K}$	2-D kernel matrix
$\mathbf{s}_{i_l}$	Location of the node i_l
$\mathbf{r}_i$	Center coordinate of the ith pixel
η	User-defined detection threshold
β_p	Forgetting factor for the short-term histogram
β_q	Forgetting factor for the long-term histogram
σ_E	Epanechnikov kernel width parameter
σ_G	Gaussian kernel width parameter

CHAPTER 2

RADIO DEVICE LOCALIZATION

2.1 Abstract

Tracking of people via active badges is important for location-aware computing and for security applications. However, the human body has a major effect on the antenna gain pattern of the device that the person is wearing. In this chapter, the gain pattern due to the effect of the human body is experimentally measured and represented by a first-order directional gain pattern model. A method is presented to estimate the model parameters from multiple received signal strength (RSS) measurements. An alternating gain and position estimation (AGAPE) algorithm is proposed to jointly estimate the orientation and the position of the badge using RSS measurements at known-position anchor nodes. Lower bounds on mean squared error (MSE) and experimental results are presented that both show that the accuracy of position estimates can be greatly improved by including orientation estimates in the localization system. Next, we propose a new tracking filter that accepts orientation estimates as input, which we call the orientation-enhanced extended Kalman filter (OE-EKF), which improves tracking accuracy in active RFID tracking systems. [1]

2.2 Introduction

Received signal strength (RSS)-based radio localization and tracking of people and assets has significant benefits for logistics, security, and safety [2, 4]. Most RSS-based methods make the assumption that transmitter badges attached to objects or carried by people have isotropic gain patterns. However, even when a transmitter badge has an antenna that is considered isotropic, the person or object has considerable effect on the badge's radiation by: absorbing power, altering the antenna impedance and thus its radiation efficiency, and distorting the antenna gain pattern [34, 35]. In this chapter, we develop models and

---

[1] This chapter contains copyrighted material, reprinted with permission from Y. Zhao, N. Patwari, P. Agrawal, and M. G. Rabbat, "Directed by directionality: Benefiting from the gain pattern of active RFID badges," IEEE Transactions on Mobile Computing, vol. 11, pp. 865-877, May 2012.

methods to handle, and in fact benefit from, the removal of the unrealistic isotropic gain pattern assumption.

Real-world directional gain patterns are problematic for both fingerprint-based and model-based RSS localization algorithms. In fingerprint-based localization, exhaustive calibration measurements are performed in the environment of interest, in which a person carries a transmitter to each location, and perhaps each facing direction, while its RSS is measured [2, 36]. The gain pattern that existed during the calibration period is assumed to hold for all transmitter badges, regardless of to what object or person they are attached. In model-based algorithms, a model relating RSS and path length is assumed [10] or estimated from training measurements [37]. When the gain pattern is no longer isotropic, in some directions, the RSS will increase, while in some other directions, the RSS will decrease. Based on the data, model-based algorithms will infer that the transmitter is closer to receivers which measured larger RSS and will thus produce estimates which are biased towards directions of high gain in the gain pattern. In this chapter, we focus on improving the robustness of model-based algorithms to real-world directional gain patterns.

In localization experiments, we find that position estimates are often biased because of a nonisotropic gain pattern. An example is shown in Figure 2.1. In an experiment described in Section 2.4.5.1, a person wears a transmitter badge on his chest, and is located using the model-based maximum likelihood estimation (MLE) algorithm that assumes isotropic gain pattern [10], which we call the naive MLE algorithm. When the person wearing the badge is facing North, the badge position estimate is biased to the North of its actual position; if the person is headed East, the badge position estimate is biased to the East of its actual postion, etc. Essentially, the naive MLE estimates that the badge is closer to receivers that measure more power, and receivers in the direction the person is facing receive more power than would be predicted by an isotropic model.

Previous studies have focused on characterizing the effects of a human body's location and orientation on RSS measurements [2, 38, 39, 40, 41]. However, we are unaware of research progress in the effort to include gain pattern in model-based RSS localization algorithms. We demonstrate progress in this direction.

To develop an improved model-based algorithm, we first require a model for the directionality of a transmitter badge when worn by a person or attached to an object. We focus on the problem of a transmitter badge worn by a person. However, we believe that tags attached to large objects will generally experience nonisotropic gain patterns as well, so extensions to other types of tagged objects are feasible. We perform experiments to measure the variation of RSS as a function of the person's orientation (*i.e.*, facing direction). Based on the results, we propose a first-order model to capture most of the variation in the gain pattern as a function of user orientation. We also present a method to estimate user orientation and directionality from ordinary RSS measurements collected by the network.

Next, we include the gain pattern model in the RSS-distance model to jointly estimate the position and orientation of people in RF sensor networks. An alternating gain and position estimation (AGAPE) algorithm is developed to jointly estimate the position, orientation, and gain pattern of the badge. Experimental results show that the root mean squared error (RMSE) can be greatly reduced by including the orientation estimate in the localization. For example, in one experiment, the RMSE from the naive MLE algorithm is 2.65 meters, while the RMSE from the proposed algorithm is 0.87 meters, a 67% reduction.

It is not obvious that a nonisotropic gain pattern can benefit coordinate localization, because of the required additional "nuisance" parameters which must be estimated. We provide theoretical results that show that having a gain pattern is not an impediment for localization algorithms – *the existence of a directional gain pattern can actually reduce position error.* For this result, we derive the Bayesian Cramér-Rao bound (Bayesian CRB) for joint estimation of orientation and position. The Bayesian CRB provides the lower bound on the mean squared error (MSE) of any estimator [32]. Comparison between the Bayesian CRB and CRB derived with an isotropic gain pattern assumption [10] shows that joint estimation of orientation and position may outperform (result in lower MSE) estimation of position alone in the isotropic case.

We also present results that show that tracking is improved by joint position and orientation estimation. Regardless of whether one uses the gain pattern in a localization algorithm or not, it is often important to track a badge's position over time to reduce uncertainty in an object or person's path. When a person wears a transmitter badge in a consistent location on their body, we can infer from their orientation which direction they will be moving, since people tend to walk forward (much more than backwards or sideways). We include this intuition to develop a Kalman tracking method which uses orientation estimates as input, which we call the orientation-enhanced extended Kalman filter (OE-EKF). Traditional Kalman filters and extended Kalman filters use only coordinate estimates as input, even though they are used to estimate velocity (and thus direction). Our OE-EKF is distinct because it uses estimated orientation *as an input*, in addition to providing estimated velocity. We find knowing orientation can also help improve the accuracy of tracking.

In summary, the contribution of this chapter is to show that real-world nonisotropic gain patterns of transmitter badges are not a problem to be ignored, but a means to improved localization and tracking performance. We propose a first-order gain pattern model and validate it from a set of measurements. We develop an algorithm to estimate gain pattern from RSS measurements, and an alternating gain and position estimation algorithm. The Bayesian CRB for the joint estimation problem is derived and compared to that for position estimation with isotropic gain patterns. Finally, an orientation-enhanced extended Kalman filter is implemented to track mobile users in RF sensor networks.

The rest of this chapter is organized as follows: Section 2.3 proposes a method to estimate the gain pattern of a transmitter badge. Section 2.4 investigates joint position and orientation estimation, including experimental and theoretical results. Section 2.5 investigates tracking, using standard Kalman filters and a new OE-EKF method. Related work is presented in Section 2.6, and finally we conclude in Section 2.7.

2.3 Models

Any improvement of model-based RSS localization algorithms must begin with statistical models that are based on real-world measurements. In this section, we present measurement-based models for the gain pattern of a transmitter badge worn by a person. A transmitter in close proximity to a human body is strongly affected by that proximity. Human tissue absorbs power sent in its direction and distorts the gain pattern of the transmitter [34, 35].

A general model for the dBm power P_i received at anchor node i from transmitter badge t, is the log-distance model [11]. Including the transmitter gain pattern, the dBm power P_i is modeled as

$$P_i = P_0 - 10 n_p \log_{10}\left(\frac{d_i}{d_0}\right) + g(\alpha_i) + \eta \tag{2.1}$$

where P_0 is the received power in dBm at a reference distance d_0, n_p is the pathloss exponent, $d_i = \|\mathbf{z}_i - \mathbf{z}_t\|$ is the distance between anchor node i at coordinate $\mathbf{z}_i$ and transmitter badge t at coordinate $\mathbf{z}_t$, α_i is the angle between anchor node i and the badge, $g(\alpha_i)$ is the gain pattern in dB of the transmitter badge at angle α_i, and η is the model error plus noise. In practice, we estimate n_p and P_0 using the received power measurements between pairs of anchor nodes. Assuming known anchor node coordinates, we estimate n_p and P_0 via linear regression, as in [10].

Naive model-based localization algorithms use $g(\alpha_i) = 0$ for all α_i. We propose to include a nonzero $g(\alpha_i)$ in (2.1). Note that the function must be periodic since $g(\alpha_i) = g(\alpha_i + 2\pi)$ for any α_i. Any real-world gain pattern will depend on the person and the badge, and will look somewhat random; however, we hope to capture the major features of $g(\alpha_i)$ that will be largely accurate for the average person.

Section 2.3.1 presents a measurement campaign to characterize average behavior of gain patterns. Based on these measurements, we formulate a model in Section 2.3.2 and evaluate the model in Section 2.3.3.

2.3.1 Measurements

We perform several experiments to quantify the effect of the orientation (facing direction) of a human body on the RSS measured from the transmitter that the person is wearing. We use two Crossbow TelosB nodes operating at 2.4 GHz. One node (node 1) is placed on a stand, and the other one (node 2) is worn by a person, hanging in the middle of his chest. While keeping the distance between these two nodes the same, the person wearing node 2 turns 45 degrees every 20 seconds. Node 2 transmits about 20 times per second, and the RSS at node 1 is recorded on a laptop. Thus about 400 RSS measurements are recorded for each of the eight different orientations. The above experiment is repeated eight times by five different people wearing the badge in the student recreation building and an empty parking lot at the University of Utah. The distances between the two nodes are varied from 1.5 to 5.0 meters in these eight different experiments. A total of 25,600 measurements are recorded.

As expected, individual measured gain patterns are unique. Figure 2.2(a) shows the measurements from two different experiments. In both experiments, the minimum RSS are at either 180 degrees or 145 degrees, and the maximum RSS are at 0 degrees or 315 degrees. The mean gain pattern, averaged across all experiments, is shown in Figure 2.2(b). We see that if the person's orientation is 180 degrees, *i.e.* the human body blocks the line-of-sight (LOS) path between node 1 and node 2, the gain pattern is close to the minimum. If the person is facing node 1, *i.e.*, an orientation of 0 degrees, then the gain pattern is about 20 dB higher than at its lowest point. The average gain pattern closely resembles a cosine function with period 360 degrees and amplitude 10 dB.

We note that the variation we see in received power as a function of angle due to the presence of the human is similar to results from other measurement studies [36, 40].

2.3.2 Gain pattern model

Based on the results of the measurements, we propose a model for the gain pattern $\hat{g}(\alpha)$, as a cosine function with period 360 degrees.

$$\hat{g}(\alpha) = G_1 \cos(\alpha - \beta) \tag{2.2}$$

where β is the orientation (direction of maximum gain) of the badge (see Figure 2.3), and $G_1 \geq 0$ is the magnitude of the cosine function in dB. We also refer to G_1 as the directionality, because high G_1 indicates that badge's pattern is highly directive in one direction, while $G_1 = 0$ indicates no directionality, *i.e.*, the badge is an isotropic radiator [2].

There are two main reasons to use the model of (2.2). First, the model represents the two most important characteristics observed in the measurements, regardless of path length or person wearing the badge: that the gain is higher in the direction the person is facing, and lower in the direction opposite. In an RF sensor network with several anchor nodes, suppose a user wearing a badge stands halfway between node j and node k facing node k, as shown in Figure 2.3. Then, based on our measurements, the mean RSS value of node k would be greater than that of node j, although the distances between the badge and these two nodes are the same.

The second reason to use (2.2) is that it is a first-order model for any periodic function, and for these data in particular, the measurements show a single order captures the vast majority of the angular variation. Any function with period 2π has a Fourier series representation as a sum of sines and cosines at frequencies that are integer multiples of $\frac{1}{2\pi}$:

$$g(\alpha) = \frac{1}{2\pi} \sum_{k=-\infty}^{\infty} G(k) e^{j2\pi k \alpha}$$

where $G(k)$ are the complex-valued Fourier series components [43]. When $g(\alpha)$ is purely real, then $G(-1)$ and $G(1)$ are complex conjugates, and thus $G(-1) + G(1) = 2\mathbb{R}\{G(1)\}$, where $\mathbb{R}$ is the real operator. As a result,

$$g(\alpha) = \frac{1}{2\pi} G(0) + \frac{1}{\pi} \mathbb{R}\left\{ \sum_{k=1}^{\infty} G(k) e^{j2\pi k \alpha} \right\}. \tag{2.3}$$

The model of (2.2) is simply the first harmonic of an arbitrary gain pattern measurement. That is, we include only the $k = 1$ term in (2.3).

2.3.3 Gain pattern model evaluation

When measuring the gain pattern at discrete values of $\alpha_i, i = 0, 1, ...N-1$, we require the discrete Fourier transform (DFT) instead of the Fourier series. However, the same principle applies – the cosine with period 2π is the first-order approximation of the gain function.

---

[2] The standard definition of directivity is related to the maximum gain across both elevation and azimuth angles; here we consider only azimuth angles, effectively assuming the maximum directive gain is along the azimuth [42].

Specifically, for the gain pattern at angle α_i, the discrete-time exponential representation is given by

$$\begin{aligned} g(\alpha_i) &= \frac{1}{N}\sum_{k=0}^{N-1} G(k)e^{j\alpha_i k} \\ &= \frac{1}{N}G(0) + \frac{2}{N}\mathbb{R}\left\{\sum_{k=1}^{M} G(k)e^{j\alpha_i k}\right\} \\ &= \frac{1}{N}G(0) + \frac{2}{N}\sum_{k=1}^{M}|G(k)|\cos\left(\angle G(k) + \alpha_i k\right) \end{aligned} \tag{2.4}$$

where $M = \dfrac{N}{2}$, and $\alpha_i = \dfrac{2\pi i}{N}$, for N equally spaced measurements. In the measurement experiments, we had $N = 8$.

The mean gain $G(0)$ is simply the average of all of the differences (which we call the model error) between P_i and the log-distance path loss model, that is, $P_0 - 10n_p \log_{10}(d_i/d_0)$. Because n_p and P_0 are determined by linear regression, they tend to make the model error zero mean. Thus we assume that $G(0) = 0$ dB because any mean model error would have been removed by the linear regression. Then, the gain pattern from an M order model can be estimated as:

$$\hat{g}_M(\alpha_i) = \frac{2}{N}\sum_{k=1}^{M}|G(k)|\cos\left(\angle G(k) + \alpha_i k\right). \tag{2.5}$$

The first-order model including only the $k = 1$ term in (2.5), is

$$\hat{g}(\alpha_i) = \frac{2}{N}|G(1)|\cos(\angle G(1) + \alpha_i). \tag{2.6}$$

To evaluate the first-order model for the gain pattern at discrete values, we use it to recover the mean gain pattern (shown in Figure 2.2(b)) obtained from eight experiments of the measurement campaign. We also use the zero-order model, *i.e.*, with only DC component $G(0)$ in (2.4), and the second, third, fourth order models to recover the actual gain pattern. The relative approximation errors are shown in Figure 2.4. We see that if we only use the DC component $G(0)$, the relative approximation error is 100%. If we use the first-order model, the relative error decreases dramatically to less than 30%. If we use higher order models, the relative error continues to decrease, but only decreases slightly as more DFT terms $G(k)$ are added. We note that, using a zero-order model with $G(0) = 0$ is equivalent to using an isotropic gain pattern assumption. Figure 2.4 shows that the approximation error from the first-order model is about 70% less than that from the zero-order model. So the first-order model is much more accurate than the zero-order model with isotropic gain pattern assumption. Although using higher order models can further reduce the approximation error, the reduction of error is not so significant compared to the reduction from the zero-order model to the first-order model. Using higher order models also requires more parameters, which increases the problem of overfitting. Thus, we propose to use the first-order sinusoidal model to quantify the effect of the human body orientation on RSS measurements.

2.4 Localization using orientation

2.4.1 Problem statement

In this section, we focus on 2-D position estimation using RSS measurements. For a network with N anchor nodes and one badge (we use one badge to simplify notation, but extension to multiple badges is possible), the position estimation problem corresponds to the estimation of the coordinates of the badge $\mathbf{z}_t = [x_t, y_t]^T$. However, from (2.2), two parameters in the gain pattern model must be estimated. So we include these two parameters as nuisance parameters, and the unknown parameter vector $\boldsymbol{\theta}$ becomes:

$$\boldsymbol{\theta} = [\mathbf{z}_t^T, \beta, G_1]^T \tag{2.7}$$

where β is the orientation of the badge, and G_1 is the directionality of the gain pattern.

2.4.2 Baseline algorithm

To estimate both the badge position and the gain pattern, a baseline algorithm – 4-D maximum likelihood estimation (MLE) algorithm is introduced here for algorithm comparison and analysis.

As discussed in Section 2.3, the received dBm power P_i is modeled as (2.1). Assuming the RSS values P_i are independent Gaussian with variance σ^2, and mean $\mu(\boldsymbol{\theta}) = P_0 - 10n_p \log_{10}(d_i/d_0) + g(\alpha_i)$, one can show that the MLE of the badge position is:

$$\hat{\boldsymbol{\theta}}_{MLE} = \arg\max_{\theta} \sum_{i=0}^{N-1} (P_i - \mu(\boldsymbol{\theta}))^2. \tag{2.8}$$

One way to find the MLE solution is to use the grid search method. For example, the TI CC2431 uses a 2-D grid search method to find the MLE coordinate estimate for the isotropic gain pattern case [44]. However, as the dimension of the estimation parameter vector $\boldsymbol{\theta}$ increases, the computation time of grid search increases exponentially. Since we have four parameters in $\boldsymbol{\theta}$, a 4-D grid search method can be used to obtain the MLE solution for analysis, but the high computation cost prohibits it from real time applications. To jointly estimate the position and the gain pattern, a different algorithm must be used.

2.4.3 Gain pattern estimator

Before we propose the algorithm to jointly estimate the position and the gain pattern, we first introduce a gain pattern estimator, assuming we know the badge position $\mathbf{z}_t$.

By comparing (2.6) and (2.2) in Section 2.3, we find the two model parameters β and G_1 of the gain pattern can be calculated as:

$$\begin{aligned} \beta &= -\angle G(1) \\ G_1 &= \frac{2}{N}|G(1)|. \end{aligned} \tag{2.9}$$

Thus to estimate the gain pattern, the DFT term $G(1)$ needs to be calculated first.

In the measurement experiments discussed in Section 2.3.1, it was possible to measure the gain at equally spaced angles. In real deployments, anchor nodes will make measurements at a variety of nonequally spaced angles α_i, depending on badge and anchor node positions. The most common way to estimate the spectral content in a signal using nonequally spaced samples is simply to apply the DFT to the available samples [45]. Thus we estimate $G(k)$ as:

$$G(k) = \sum_{i=0}^{N-1} g(\alpha_i) e^{-j\alpha_i k}. \tag{2.10}$$

To calculate $g(\alpha_i)$ in (2.10), rewriting (2.1), we have:

$$g(\alpha_i) = P_i - P_0 + 10 n_p \log_{10} \frac{d_i}{d_0} \tag{2.11}$$

where α_i is the angle between anchor node i and badge

$$\alpha_i = \operatorname{atan}\left(\frac{y_i - y_t}{x_i - x_t}\right).$$

Note we need only $G(1)$ for the first-order model of (2.2). This calculation of $G(1)$ requires only N complex multiplies and adds, where N is the number of RSS measurements received for a badge. This low complexity is important to minimize the computational complexity of the localization algorithm.

2.4.4 Alternating gain and position estimator

In the gain pattern estimator, we assumed known badge position, which in general, is unknown. For joint position and gain pattern estimation, in this section, we propose an alternating gain and position estimation (AGAPE) algorithm to efficiently estimate both the position and orientation of the user wearing a badge in an RF sensor network.

The basic idea of this algorithm is to first estimate the position of the badge, and take advantage of the first-order sinusoidal model to calculate the gain pattern parameters.

Given the gain pattern, we use the RSS-distance model (2.1) to reestimate the position of the badge. The algorithm iterates until a misfit function is minimized. We note that the proposed AGAPE algorithm is a form of alternating minimization method [46].

The flowchart of the AGAPE algorithm is shown in Figure 2.5, and the detailed procedure is discussed here. For the first step, assuming the gain pattern is isotropic, we use the naive MLE method to estimate the badge position based on the RSS-distance model in [10]. The MLE solution can be found via a conjugate gradient algorithm [10], here, we use a 2-D grid search method in the position estimation step to avoid the local minima problem from a numerical method. Again, we note that 2-D MLE grid search can be accomplished quickly in hardware [44]. The output of the position estimation step, we refer to as $\hat{\mathbf{z}}_t$.

The next step is the orientation estimation step. Given an estimated position, we calculate the gain pattern $g(\alpha_i)$ from the RSS-distance model (2.1)

$$g(\alpha_i) = P_i - P_0 + 10 n_p \log_{10} \frac{\|\hat{\mathbf{z}}_t - \mathbf{z}_i\|}{d_0}. \tag{2.12}$$

And then, $G(1)$ is calculated from (2.10). After that, the orientation β is estimated from the phase angle of $G(1)$, and the directionality G_1 is estimated from the magnitude of $G(1)$, as given in (2.9). Finally, we use the estimated $\hat{\beta}$ and $\hat{G_1}$ in the RSS-distance model to estimate the position of the badge $\hat{\mathbf{z}}_t$ again.

The steps of position estimation and orientation estimation repeat until the following misfit function is minimized:

$$\Phi = \sum_{i=1}^{N} \left(P_i - \hat{P_i} \right)^2 \tag{2.13}$$

where $\hat{P_i}$ is the RSS estimate at anchor node i, which is calculated from the RSS-distance model (2.1) using estimated badge position $\hat{\mathbf{z}}_t$, and estimated gain parameters $\hat{\beta}$ and $\hat{G_1}$. We do not study convergence results for the AGAPE algorithm. Since minimizing (3.12) corresponds to a nonlinear least squares problem, we expect that AGAPE will be trapped in local minima. To avoid reporting local minima, we rerun the algorithm from different initial conditions. We fix the initial values of G_1 to a nonzero value, set the initial values of β to a combination of four different orientations, *i.e.*, 0, 90, 180, and 270 degrees, perform AGAPE for each initial condition and choose the result with the minimum misfit function as the final result.

2.4.5 Experiment and results

2.4.5.1 Experiment description

Three localization experiments are performed in a 6.4 m by 6.4 m area outside the Merrill Engineering Building of the University of Utah. This grassy area is near trees and 3 m away from the building wall. The area is surrounded by 28 TelosB anchor nodes deployed at known locations on stands at 1 m height. The nodes are programmed with TinyOS program Spin [7] to allow collection and recording of pairwise RSS measurements.

First, we measure pairwise RSS measurements between anchor nodes. Since the locations of the anchor nodes are known, we use the measured RSS and the link length to estimate the n_p and P_0 parameters of the log-distance model of (2.1). Then, a person wears a TelosB node in the middle of his chest, and walks on a marked path at a constant speed of about 0.5 m/s. We ensure a constant speed using a metered path and a metronome. For example, in one experiment (Experiment 1), a person walks twice around a marked square path. Since the square path is marked and the person walks at a constant speed, the actual positions of the person are known at all times. Also, the person always walks forward in a straight line along each side of the square path, so the orientation of the badge is always identical to his walking direction. In the other two experiments (Experiments 2 and 3), another TelosB node is worn by another person. He walks on a marked rectangular path and a marked square path, respectively in Experiments 2 and 3. The actual positions and orientations of the badge during these experiments are both known, so we can compare them with the position and orientation estimates from the AGAPE algorithm.

2.4.5.2 Experimental results

For Experiment 1, the estimated orientations are shown in Figure 2.6, together with the actual walking directions (badge orientations). The orientation estimates generally agree well with the actual orientations. The deviations from the actual orientations are generally less than 30 degrees. However, sometimes when the person is turning, the bias is larger than 30 degrees. This may be due to the fact that the algorithm uses RSS measurements from 28 anchor nodes to estimate the person's orientations, and at the turning points, RSS measurements may be a mix of those recorded before, after and during turning.

The cumulative distribution function (CDF) of the orientation estimation error is shown in Figure 2.7. The median error from the AGAPE algorithm is about 10 degrees, and more than 90% errors are below 30 degrees. Also shown in Figure 2.7 is the CDF of orientation error from the MLE 4-D grid search method. The MLE 4-D grid search method searches every 10 degrees for the MLE solution of the orientation. While the grid search method takes much more time (on the order of 10 times more than the AGAPE algorithm in our Python implementation), the estimates are not more accurate than those from AGAPE. The median error from the grid search method is also 10 degrees.

Besides the orientation of the badge, another nuisance parameter G_1 is also estimated. The average value of the estimated G_1 is 12, which suggests that the directionality of the gain of the transmitter badge worn by this particular person in this particular environment is about 12 dB. This value is consistent with the results from our measurement campaign discussed in Section 2.3.1.

The most important result that we are interested in is the performance of position estimation. The CDF of the position estimation error is shown in Figure 2.8. The median error of the position estimates is about 0.61 m, and about 90% of the estimation error is below 1.22 m. However, for the naive MLE method, the median error is 2.60 m, which is about 4.3 times larger than that from AGAPE. From the comparison of the CDFs, we see that significant improvement is made if we include the orientation estimate in the localization.

We also compare the root mean squared error (RMSE) of the position estimates, which is defined as:

$$RMSE = \sqrt{\frac{1}{K}\sum_{k=0}^{K-1}(\hat{x_t}^{(k)} - x_0)^2 + (\hat{y_t}^{(k)} - y_0)^2} \tag{2.14}$$

where $\hat{x_t}^{(k)}$, $\hat{y_t}^{(k)}$ are estimated coordinates at time k, and x_0, y_0 are actual coordinates.

The RMSEs from the AGAPE algorithm of all three experiments are listed in Table 2.1. Also listed are the RMSEs from the naive MLE 2-D method, and the RMSEs from the MLE 4-D grid search method. We see that for Experiment 1, the RMSE from AGAPE is 0.87 m, which is similar to the MLE 4-D grid search method. However, the MLE 4-D grid search method, due to its computational complexity, is not a real time algorithm. The RMSE from the naive MLE 2-D method with an isotropic gain pattern assumption is 2.64 m. So for Experiment 1, the RMSE from AGAPE is reduced by 67.2% compared to the MLE 2-D method. For Experiments 2 and 3, the RMSEs are reduced by 65.4% and 68.9%, respectively.

2.4.5.3 Effect of number of anchor nodes

In the three experiments discussed above, we use 28 anchor nodes to locate a badge in a 6.4 m by 6.4 m square area. In some applications, we may not be able to have so many anchor nodes. To see the effect of node number on the localization accuracy of the AGAPE algorithm, we perform the following tests by using RSS measurements from only a fraction of all anchor nodes.

In the first test – Test 1, we use RSS measurements from different numbers of equally spaced anchor nodes to locate the badge. For example, using the data collected in Experiment 2, we first choose the RSS measurements from four anchor nodes at each corner of the square area. As expected, the localization is not very accurate, the RMSE of the position estimate is 3.36 m, and the RMSE of the orientation estimate is 40 degrees. Next, we use the RSS measurements from those anchor nodes whose ID numbers are multiples of 1, 2, 3 and 4 (since the anchor nodes are placed in a numerically increasing order around the experimental area, these anchor nodes are equally spaced). The RMSEs of the position and orientation estimates are shown as dots (•) in Figure 2.9(a) and (b), respectively. We see that as the node number increases, the RMSEs of position and orientation estimates both decrease. When the node number increases to fourteen, the RMSE of the position estimate decreases to 1.30 m, and the RMSE of the orientation estimate decreases to 18 degrees. Further increase of anchor nodes will continue to decrease the RMSEs; however, there are diminishing returns.

In practical scenarios, anchor nodes may not be equally spaced. Thus in Test 2, we use RSS measurements from randomly chosen anchor nodes. For example, we randomly choose four anchor nodes, and run AGAPE using the RSS measurements from these nodes. We repeat the above procedure 100 times, and each time calculate the RMSEs of the position and orientation estimates. Similarly, we randomly choose seven, ten, fourteen and twenty anchor nodes. The average RMSEs are shown as squares (■), and the RMSE standard deviations are shown as error bars in Figure 2.9. From Figure 2.9(b), we see that the average orientation RMSEs in Test 2 are all larger than the RMSEs in Test 1. For position RMSEs shown in Figure 2.9(a), the average RMSEs in Test 2 are generally larger than the RMSEs in Test 1, except for the extreme case when the number of anchor nodes is four. Thus, the AGAPE algorithm generally performs better if the anchor nodes are equally spaced. However, the AGAPE algorithm is not very sensitive to the effect of anchor nodes being nonequally spaced. In fact, the differences between the position RMSEs in Test 1 and the average position RMSEs in Test 2 are always less than 0.4 m.

Finally, we compare the performance of the naive MLE 2-D method with the AGAPE algorithm using randomly chosen nodes. As shown in Figure 2.9(a), the MLE 2-D method is not very sensitive to the number of anchor nodes. However, the average position RMSEs from the MLE 2-D method are always larger than those from the AGAPE algorithm for different numbers of anchor nodes.

2.4.6 Estimator lower bounds

One might think that the introduction of an additional unknown gain pattern model would increase the lower bound of the variance of an estimator. To see if that is true, we derive the Bayesian CRB [32] by including the gain pattern model parameters as nuisance parameters. We use the Bayesian CRB, because we have prior knowledge of the gain directionality G_1. We show that the CRB with an isotropic gain pattern assumption derived in [10] is a special case of the Bayesian CRB derived in this chapter. Then we compare the Bayesian CRB with and without isotropic gain pattern assumption. Our comparison shows that the introduction of a gain pattern model decreases the lower bound on the variance of a position estimator.

2.4.6.1 Bayesian CRB

The gain pattern model expressed in (2.2) can be rewritten as:

$$g(\alpha_i) = G_I \cos\alpha_i + G_Q \sin\alpha_i \tag{2.15}$$

where $G_I = G_1 \cos\beta$, $G_Q = G_1 \sin\beta$.

To derive the Bayesian CRB, we assume that the orientation of the badge β is uniformly distributed in the range of 0 to 2π, because the orientation of the person wearing the badge is arbitrary. Next, we assume the in-phase component G_I and quadrature component G_Q of G_1 are i.i.d. Gaussian distributed with zero means and variance σ_G^2. G_I and G_Q are affected by many different aspects of the person's shape and size, and the badge placement, and thus may, by a central limit argument, be close to Gaussian. This assumption is equivalent to the assumption that G_1 is Rayleigh distributed [47], which agrees with our prior knowledge of G_1: (1) G_1 must be nonnegative and thus cannot be modeled as Gaussian or any distribution with infinite negative support; (2) G_1 may be small but is unlikely to be exactly zero for a person wearing a badge; and (3) G_1 is very unlikely to have very large values, since gain is related to (human) size. Improvement upon this distributional assumption must come from a population study with many participants, which we suggest for future research.

The Bayesian CRB is also called the Van Trees bound, or the MSE bound [32], it is given by:

$$\mathrm{var}(\boldsymbol{\theta}) \geq (I_D + I_P)^{-1} \tag{2.16}$$

where $\boldsymbol{\theta} = [\mathbf{z}_t^T, G_I, G_Q]^T$, I_D is the Fisher information matrix, and I_P is the prior information matrix [32]. Note that we only include the prior information of the gain pattern, no prior information of the badge position is included in the derivation of the Bayesian CRB.

All the elements in I_D can be expressed as:

$$[I_D]_{mn} = -E_P\left[E_D\left(\frac{\partial^2 \ln f_D}{\partial\boldsymbol{\theta}_m\partial\boldsymbol{\theta}_n}\right)\right] \tag{2.17}$$

where E_D is the expectation with respect to data, E_P is the expectation with respect to prior information of $\boldsymbol{\theta}$, and f_D is the joint PDF of measurements P_i, which are assumed to be independent Gaussian with mean $\mu(\boldsymbol{\theta})$ and variance σ^2.

The elements of I_P can be written as:

$$[I_P]_{mn} = -E_P\left(\frac{\partial^2 \ln f_P}{\partial\boldsymbol{\theta}_m\partial\boldsymbol{\theta}_n}\right) \tag{2.18}$$

where f_P is the PDF of the prior information of $\boldsymbol{\theta}$.

As shown in the supplemental material, the information matrix $I_D + I_P$ can be written as:

$$I_D + I_P = I_{\boldsymbol{\theta}} = \begin{bmatrix} A_{11} & A_{12} \\ A_{21} & A_{22} \end{bmatrix} \tag{2.19}$$

where

$$A_{11} = \begin{bmatrix} J_{xx} + M_{xy} & J_{xy} + N_{xy} \\ J_{xy} + N_{xy} & J_{yy} + M_{yx} \end{bmatrix} \tag{2.20}$$

$$A_{12} = A_{21} = \begin{bmatrix} K_{xx} & K_{xy} \\ K_{xy} & K_{yy} \end{bmatrix} \tag{2.21}$$

$$A_{22} = \begin{bmatrix} L_{xx} & L_{xy} \\ L_{xy} & L_{yy} \end{bmatrix} \tag{2.22}$$

where $J_{xx} = J(\Delta x_{it}, \Delta x_{it})$, $K_{xx} = K(\Delta x_{it}, \Delta x_{it})$, $L_{xx} = L(\Delta x_{it}, \Delta x_{it})$, $M_{xx} = M(\Delta x_{it}, \Delta x_{it})$, $N_{xx} = N(\Delta x_{it}, \Delta x_{it})$, and $\Delta x_{it} = x_i - x_t$, and

$$J(u,v) = \frac{c^2}{\sigma^{2N}} \sum_{i=0}^{N-1} \frac{u}{d_{it}^2} \frac{v}{d_{it}^2} \tag{2.23}$$

$$K(u,v) = \frac{c}{\sigma^{2N}} \sum_{i=0}^{N-1} \frac{uv}{d_{it}^3} \tag{2.24}$$

$$L(u,v) = \frac{1}{\sigma^{2N}} \sum_{i=0}^{N-1} \frac{u}{d_{it}} \frac{v}{d_{it}} + \frac{1}{\sigma_G^2} \tag{2.25}$$

$$M(u,v) = \frac{\sigma_G^2}{\sigma^{2N}} \sum_{i=0}^{N-1} \left(\frac{1}{d_{it}^2} + \frac{u^4}{d_{it}^6} + \frac{u^2v^2}{d_{it}^6} - 2\frac{u^2}{d_{it}^4}\right) \tag{2.26}$$

$$N(u,v) = \frac{\sigma_G^2}{\sigma^{2N}} \sum_{i=0}^{N-1} \left(\frac{u^3v}{d_{it}^6} + \frac{v^3u}{d_{it}^6} - 2\frac{uv}{d_{it}^4}\right) \tag{2.27}$$

where $c = \dfrac{10n_p}{\ln 10}$.

2.4.6.2 Comparison with related literature

In related literature [10], a CRB is derived assuming the gain pattern is isotropic. In terms of the Bayesian CRB derived in this chapter, the gain pattern term in the RSS-distance model is assumed to be zero. Since the RSS-distance model used in [10] can be considered as a special case of the RSS-distance model used here with $g(\alpha_i) = 0$, the Bayesian CRB derived here should be the same as the CRB derived in [10] when σ_G^2 approaches zero. This is shown next.

By using the blockwise matrix inversion, the inverse of the Fisher Information matrix can be written as:

$$I_{\boldsymbol{\theta}}^{-1} = \begin{bmatrix} F_{11}^{-1} & -A_{11}^{-1}A_{12}F_{22}^{-1} \\ -F_{22}^{-1}A_{21}A_{11}^{-1} & F_{22}^{-1} \end{bmatrix} \tag{2.28}$$

where $F_{11} = A_{11} - A_{12}A_{22}^{-1}A_{21}$ and $F_{22} = A_{22} - A_{21}A_{11}^{-1}A_{12}$.

In the limit as $\sigma_G^2 \to 0$, M_{xy}, M_{yx}, N_{xy} all become zero, so we have:

$$\lim_{\sigma_G^2 \to 0} A_{11} = \begin{bmatrix} J_{xx} & J_{xy} \\ J_{xy} & J_{yy} \end{bmatrix} \triangleq J \tag{2.29}$$

$$\lim_{\sigma_G^2 \to 0} A_{22} = \begin{bmatrix} L_{xx} & L_{xy} \\ L_{xy} & L_{yy} \end{bmatrix} = \infty. \tag{2.30}$$

Thus, $F_{11} = A_{11}$, and $F_{22}^{-1} = 0$. So the inverse of the Fisher information matrix becomes:

$$\lim_{\sigma_G^2 \to 0} I_{\boldsymbol{\theta}}^{-1} = \begin{bmatrix} J^{-1} & 0 \\ 0 & 0 \end{bmatrix}. \tag{2.31}$$

Notice that (2.29) is the same as (10) in [10], which assumes isotropic gain pattern. This proves that the CRB derived in [10] is a special case of the Bayesian CRB derived here, and if σ_G^2 approaches zero, the Bayesian CRB converges to the CRB derived previously.

2.4.6.3 Discussion

From (2.23) to (2.27), we see that the Bayesian CRB not only depends on radio channel parameters n_p and σ^2, but also depends on gain pattern parameter σ_G^2. Once we have these three parameters, we can calculate the Bayesian CRB for an L m by L m square area surrounded by four anchor nodes located at each corner.

Using the same channel parameters as [10] ($n_p/\sigma = 1.7$), the Bayesian CRBs with two different σ_G^2 are shown in Figure 2.10. As expected, if σ_G^2 is very close to zero, *e.g.*, $\sigma_G^2 = 0.0001$, the Bayesian CRB is identical to the CRB derived in [10], as shown in Figure 2.10(a). If σ_G^2 is not close to zero, *e.g.*, $\sigma_G^2 = 1$, the Bayesian CRB is shown in Figure 2.10(b). From the comparison of Figure 2.10(a) and (b), we see that the maximum value and minimum value of Bayesian CRB are both lower than the CRB with an isotropic gain pattern assumption. If we introduce the "average RMSE bound" as the average value of the square root of the Bayesian CRB bounds over this L m by L m area, the average RMSE bound for $\sigma_G^2 = 1$ is 0.29 m, which is also lower than the 0.30 m average RMSE bound with $\sigma_G^2 = 0.0001$.

Further, the average RMSE bounds with different σ_G^2 are shown in Figure 2.11. Since higher σ_G^2 represents higher directionality G_1, we see that the RMSE bound is lower if the directionality of the gain pattern is higher. Note that we assume the number of anchor nodes that can receive the signal transmitted from the badge stays fixed for all σ_G^2.

In sum, we conclude that the RMSE bound with a directional gain pattern assumption could be lower than the RMSE bound with an isotropic gain pattern assumption. For the directional gain pattern case, we would benefit more, *i.e.*, have a lower RMSE bound from a gain pattern with a higher directionality, if the number of nodes that can hear the badge stays fixed.

2.5 Tracking

In this section, we introduce an improved tracking method that takes advantage of the user's orientation estimate from the AGAPE algorithm, and that people generally walk in the direction they are facing. We develop a novel Kalman filter which additionally tracks user orientation, and uses this to further improve coordinate tracking. Traditional Kalman filters and extended Kalman filters use only coordinate estimates as input, even though they are used to estimate velocity (and thus direction). Our orientation enhanced extended Kalman filter (OE-EKF) is distinct because it uses estimated orientation *as an input*, in addition to providing estimated velocity. We also compare the tracking results from traditional Kalman filters and our OE-EKF. The results show that without any additional measurements, the OE-EKF is noticeably more robust to large errors.

2.5.1 Kalman filter

In the traditional Kalman filter, the current state vector, which in this case includes both mobile's position and velocity, is related with the previous state by the following model:

$$\mathbf{s}[n] = A\mathbf{s}[n-1] + \mathbf{u}[n] \tag{2.32}$$

where the state vector $\mathbf{s} = [P_x, P_y, V_x, V_y]^T$, the driving noise $\mathbf{u} = [0, 0, u_x, u_y]^T$, and matrix A is:

$$A = \begin{bmatrix} 1 & 0 & 1 & 0 \\ 0 & 1 & 0 & 1 \\ 0 & 0 & 1 & 0 \\ 0 & 0 & 0 & 1 \end{bmatrix}. \tag{2.33}$$

For the traditional Kalman filter without orientation in the measurement vector, the observation model is:

$$\mathbf{x}[n] = H\mathbf{s}[n] + \mathbf{w}[n] \tag{2.34}$$

where the measurement vector $\mathbf{x} = [\hat{x_t}, \hat{y_t}]^T$ is from the coordinate estimates from the AGAPE algorithm. The measurement noise $\mathbf{w} = [w_x, w_y]^T$, and the observation matrix H is:

$$H = \begin{bmatrix} 1 & 0 & 0 & 0 \\ 0 & 1 & 0 & 0 \end{bmatrix}. \tag{2.35}$$

2.5.2 Orientation-enhanced extended Kalman filter

As discussed in Section 2.4.4, the AGAPE algorithm can produce both position and orientation estimates of a mobile person. Here, we propose a novel Kalman filter that uses the output of the AGAPE algorithm as input to the tracking algorithm. If we include the mobile person's orientation in the Kalman filter, the state model (2.32) remains the same. However, the observation model becomes nonlinear, because the orientation cannot be explicitly expressed as a linear function of the state vector. Thus the extended Kalman filter must be used. Since we add orientation information in the measurement vector, we call it orientation-enhanced extended Kalman filter (OE-EKF).

The observation model of the OE-EKF is:

$$\mathbf{x}[n] = \mathbf{h}(\mathbf{s}[n]) + \mathbf{w}[n] \tag{2.36}$$

where $\mathbf{h}$ is the nonlinear function relating state vector $\mathbf{s}$ to measurement vector $\mathbf{x}$.

If the mobile person is moving forward, then the orientation β of that person can be expressed as the arctangent of the ratio of Y component of velocity to X component of velocity. If the mobile person is moving backward, then there is a 180 degrees difference between β and the arctangent function. Because in most situations people move forward, his or her orientation can be expressed as:

$$\beta = \text{atan}\left(\frac{V_y}{V_x}\right) \tag{2.37}$$

where V_y and V_x are Y component and X component of velocity, respectively.

To avoid the ambiguity of π or $-\pi$ from arctangent function, instead of directly using β, we use $\cos\beta$ and $\sin\beta$ in the measurement vector. So for the extended Kalman filter, the measurement vector becomes:

$$\mathbf{x} = [P_x, P_y, \cos\beta, \sin\beta]^T . \tag{2.38}$$

Accordingly, $\mathbf{h}(\mathbf{s})$ in the new measurement model equation becomes:

$$\mathbf{h}(\mathbf{s}) = \left[P_x, P_y, \frac{V_x}{\sqrt{V_x^2 + V_y^2}}, \frac{V_y}{\sqrt{V_x^2 + V_y^2}}\right]^T . \tag{2.39}$$

Then the Jacobian matrix can be written as:

$$J = \frac{\partial \mathbf{h}(\mathbf{s})}{\partial \mathbf{s}} = \begin{bmatrix} 1 & 0 & 0 & 0 \\ 0 & 1 & 0 & 0 \\ 0 & 0 & J_{33} & J_{34} \\ 0 & 0 & J_{43} & J_{44} \end{bmatrix} \tag{2.40}$$

where

$$\begin{aligned} J_{33} &= \tfrac{\partial}{\partial V_x}\left(V_x/\sqrt{V_x^2 + V_y^2}\right) \\ J_{34} &= \tfrac{\partial}{\partial V_y}\left(V_x/\sqrt{V_x^2 + V_y^2}\right) \\ J_{43} &= \tfrac{\partial}{\partial V_x}\left(V_y/\sqrt{V_x^2 + V_y^2}\right) \\ J_{44} &= \tfrac{\partial}{\partial V_y}\left(V_y/\sqrt{V_x^2 + V_y^2}\right) . \end{aligned}$$

Once we have the Jacobian matrix, the OE-EKF is implemented following the basic equations in [48].

2.5.3 Experimental results

Using the same data collected from the outdoor experiments discussed in Section 2.4.5.2, and using the output of the AGAPE algorithm, we apply the Kalman filter and OE-EKF to track the person wearing the badge.

For Experiment 1, the position tracking results from the Kalman filter and OE-EKF are shown in Figure 2.12. We see that due to the lack of previous measurements, the first position tracking result is more than 1 meter away from the actual position for both the Kalman filter and the OE-EKF. However, as more and more measurements are available, the tracking errors become generally less than 0.5 meters.

From the comparison of the Kalman filter and OE-EKF tracking results, we see that with the help of orientation estimates from the AGAPE algorithm, the position tracking from the OE-EKF is more accurate than that from the Kalman filter. We note that if the variance of orientation estimate is set to be a very large number, then the tracking result from the OE-EKF is almost identical to that of the Kalman filter. That is, if little weight is given to the observation of the orientation, our OE-EKF is simplified to the Kalman filter.

The orientation tracking results from the OE-EKF are shown in Figure 2.13. Compared to the orientation estimates from the AGAPE algorithm, the estimated orientations from the OE-EKF are closer to the actual orientation when the user is walking along a straight line. However, at each corner of the square path, when the user changes direction suddenly by 90 degrees, the OE-EKF needs several measurements to adjust orientation estimates to the correct directions. This overshoot problem at points of high acceleration is very common for a Kalman filter tracking method, and can be minimized with more complicated models of movement dynamics and measurement noise [49], however, these are not in the scope of this dissertation.

To quantify the improvement that the gain pattern and the orientation estimate from the AGAPE algorithm can make in tracking, the RMSEs from the following three tracking methods are listed in Table 2.2.

- KF without gain: the Kalman filter using position estimate from the naive MLE method with an isotropic gain pattern assumption.
- KF with gain: the Kalman filter using position estimate from AGAPE.
- OE-EKF: the extended Kalman filter using both position and orientation estimates from AGAPE.

From Table 2.2, we see that the RMSEs from KF without gain method are all above 2.0 m for three experiments. For KF with gain method, which only uses position estimates from AGAPE as input, the average RMSE of the three experiments is 0.53 m. Since both the position estimate and orientation estimate from the AGAPE algorithm are used in OE-EKF, the RMSEs from OE-EKF method are further reduced compared to KF with gain method for all three experiments.

The CDFs of the position tracking errors from these three tracking methods are shown in Figure 2.14. The median error for KF without gain method is about 2.3 m, while the median errors for KF with gain and OE-EKF methods are both about 0.4 m. However, OE-EKF method has 95% of tracking errors less than 0.76 m, while KF with gain method has 95% of tracking errors less than 0.90 m. In this case, OE-EKF shows 16.7% improvement. Using the 95 percentile of errors shows the robustness to large errors. The experimental results show that OE-EKF is more robust to large errors without any additional measurements.

In OE-EKF, we assume that people walk forward with the badge on their front. If badges were consistently worn on a different side, that side could be estimated and the tracking algorithm adjusted accordingly. If this assumption was often violated (*e.g.*, if the person walked backwards or sideways), KF with gain method would likely perform better than OE-EKF.

2.6 Related work

In wireless sensor network localization, many kinds of measurements can be used: angle of arrival (AOA), time of arrival (TOA), time difference of arrival (TDOA), received signal strength (RSS), etc [8]. This work uses estimated angle (orientation) of the badge in the position estimation; however, it is not like the AOA-based localization. In AOA-based localization, anchor nodes measure the angle from which power arrives at a receiver using a directional antenna. We do not use any directional antenna – anchor nodes only measure RSS. Moreover, we estimate a user's facing direction (orientation), not the direction to any other device. For RSS-based localization, many algorithms have been proposed to improve the localization accuracy [3, 37, 50]. The performance of RSS-based localization algorithms are limited by the irregularities in measured RSS. Variation in RSS is caused by the presence of multipath, shadowing caused by the presence of obstacles in the environment, and also nonuniformity of the antenna gain pattern [51, 52]. Little effort has been made towards including gain pattern in model-based RSS localization algorithms.

Many localization studies have already shown the effect of human body orientation on RSS measurements [2, 38, 39, 40]. Kaemarungsi and Krishnamurthy [40] examine the effects of the human body orientation on RSS measurements using four different user's orientations (facing North, West, South and East). Their experiments show that the mean RSS of one orientation, at which the user body blocks the LOS could be more than 9.0 dB lower than that of another orientation. Experiments performed by [36] measure the RSS every 45 degrees while a person carrying a mobile device turns around. Their experimental results show that the RSS increases nearly 15 dB in case of a direct LOS between a receiver and an access point. In this chapter, we also perform a measurement campaign to study the variation of RSS as a function of user orientation. The results of our measurement campaign agree with the findings of [36], and we further provide a model that quantifies RSS measurements as a function of user orientations.

Other research has independently determined that user orientation is significant in improving the localization accuracy [53, 54]. However, these methods determine the effect of the user orientation based on a separate training campaign, which consumes significant human effort and time. This chapter provides a statistical model to quantify the effect of human body orientation on RSS, which could simplify the fingerprint database construction. Thus our work can improve model-based localization, and is also complementary to fingerprint-based localization.

2.7 Conclusion

In this chapter, we model the variation of RSS due to the human body as a cosine function of the orientations of the body, and we propose a first-order sinusoidal model that is useful for user orientation estimation from multiple RSS measurements. We implement the AGAPE algorithm to estimate both the position and the orientation of the user. We also implement an OE-EKF by including orientation estimate in tracking. Experimental results show that estimating the nonisotropic gain pattern can greatly improve both localization and tracking of people in RF sensor networks.

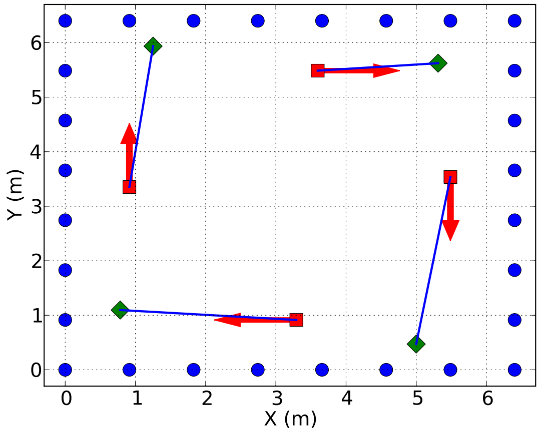

Figure 2.1: Position estimate error due to nonisotropic gain pattern (anchor node positions (●); actual badge positions (■); MLE estimates (♦); walking directions (⇒)).

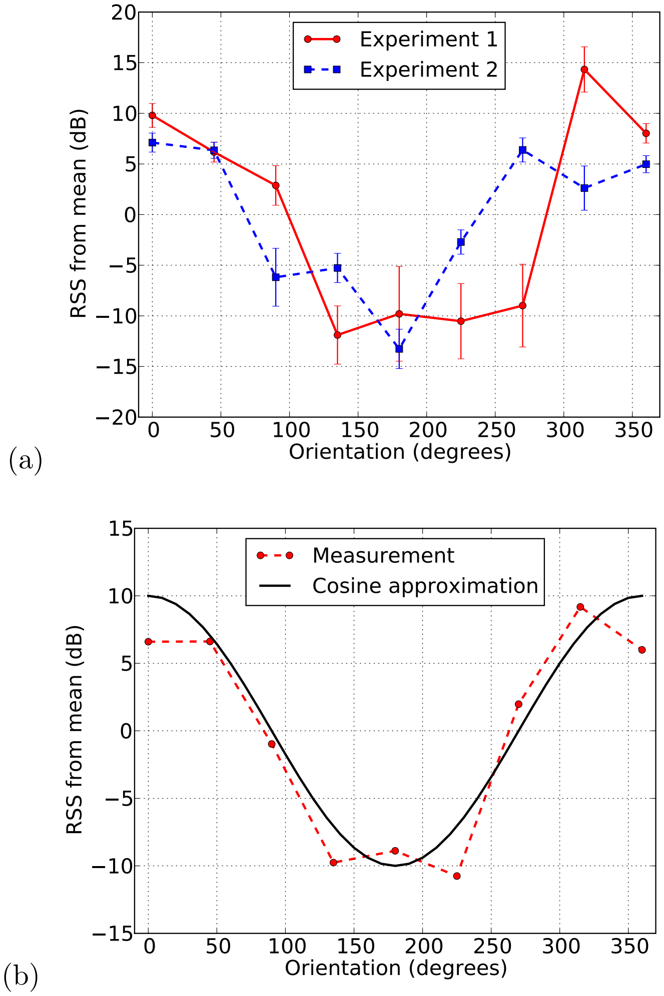

Figure 2.2: Human body effect on gain pattern (RSS from mean). (a) Measured gain patterns and $1-\sigma$ error bars in two different experiments (Gain pattern at each orientation is averaged over about 400 measurements during a period of 20 seconds); (b) Average over all measured data (Gain pattern is maximum when person is facing 0 degrees to the other sensor).

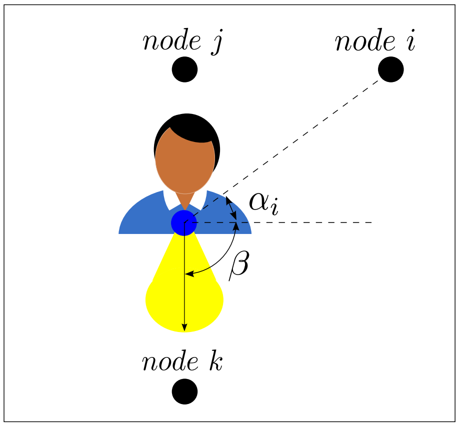

Figure 2.3: Gain pattern of a badge in a network.

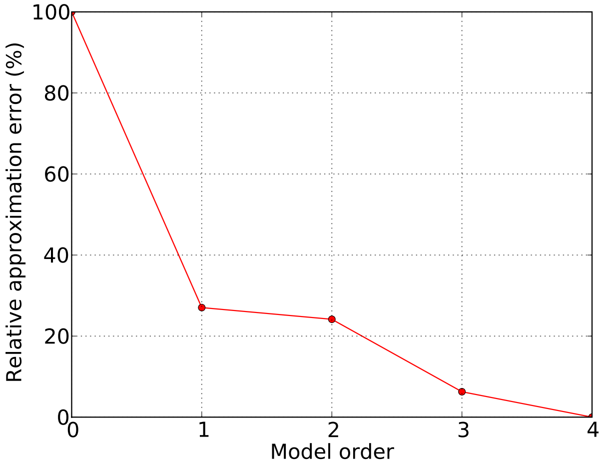

Figure 2.4: Relative approximation error vs. model order (number 0 corresponds to the isotropic gain model, number 1 corresponds to the first-order model; the approximation error is relative to the error of the isotropic gain model).

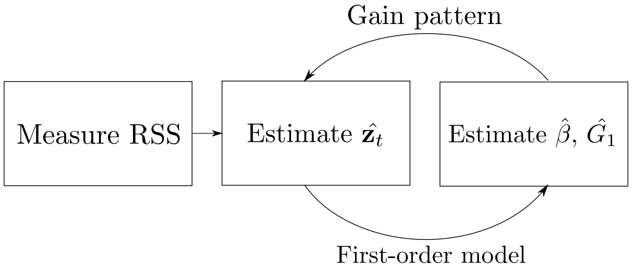

Figure 2.5: Flowchart of the AGAPE algorithm.

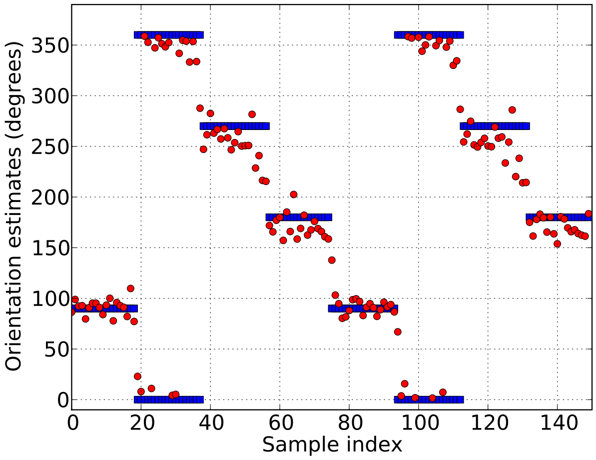

Figure 2.6: Mobile's actual orientations (■) and orientation estimates (●) (time for each sample is about 0.4 seconds).

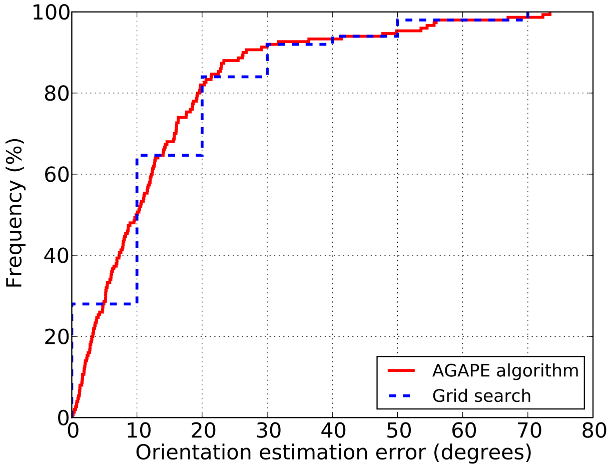

Figure 2.7: CDF of orientation estimation error.

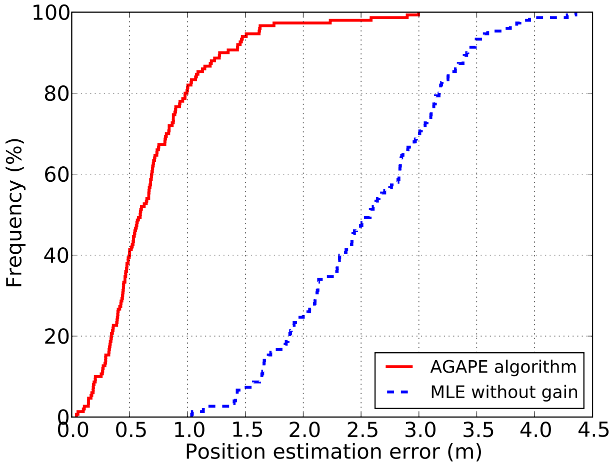

Figure 2.8: CDF of position estimation error.

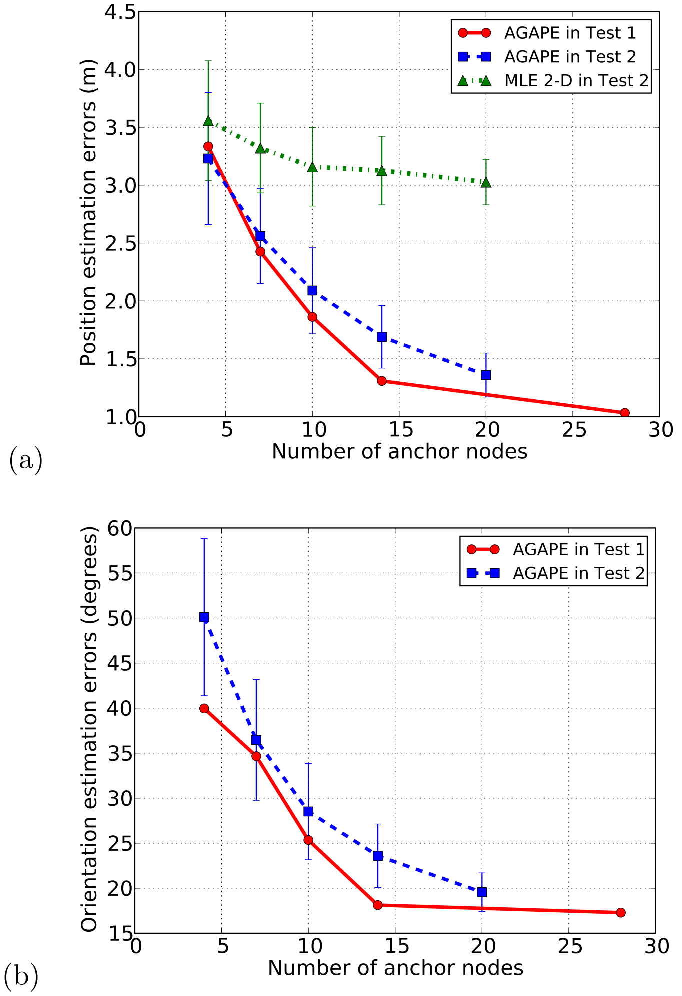

Figure 2.9: Effect of node number on estimation error. (a) Position estimation error; (b) Orientation estimation error. (Test 1 uses equally spaced anchor nodes, and Test 2 uses randomly chosen anchor nodes)

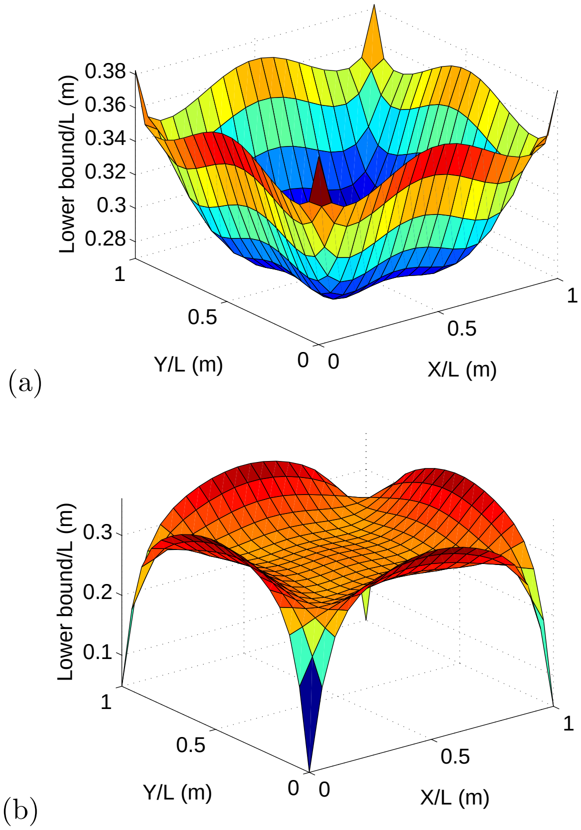

Figure 2.10: Lower bounds. (a) Lower bound with $\sigma_G^2 = 0.0001$ (minimum value: 0.27, maximum value: 0.38); (b) Lower bound with $\sigma_G^2 = 1$ (minimum value: 0.05, maximum value: 0.36).

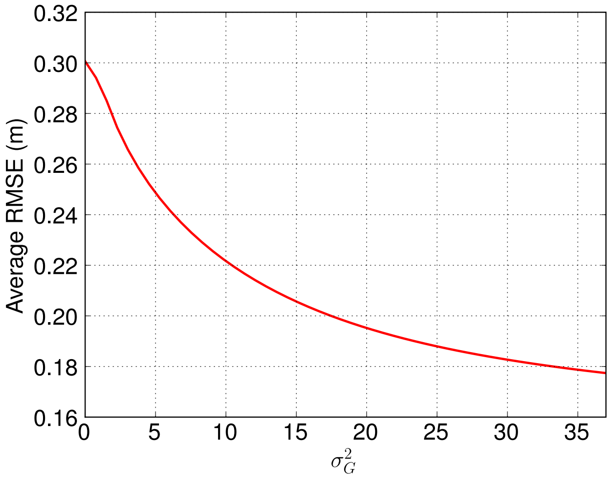

Figure 2.11: RMSE bounds as a function of σ_G^2.

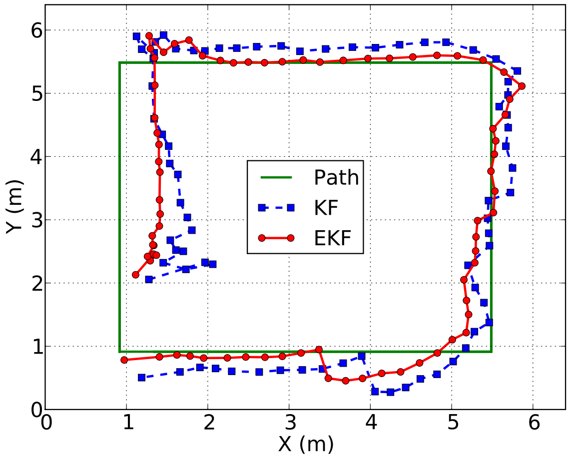

Figure 2.12: Position estimates (a) from KF (■); (b) from OE-EKF (●) (Only the first round tracking results from Experiment 1 are shown here).

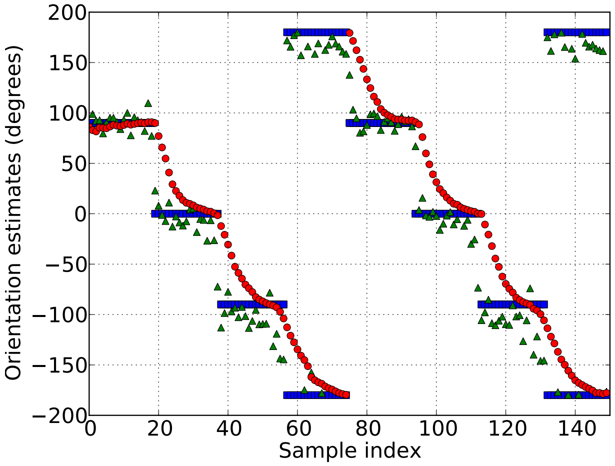

Figure 2.13: Orientation estimates (a) from OE-EKF (●); (b) from AGAPE (▲).

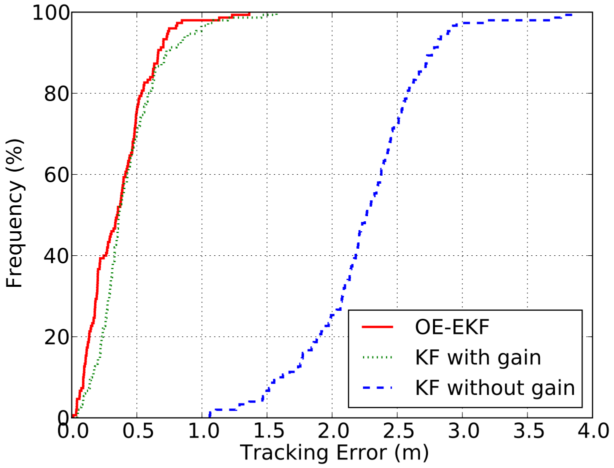

Figure 2.14: CDFs comparison of different tracking methods using data from Experiment 1.

Table 2.1: Experimental localization results: RMSEs from MLE (2-D), MLE (4-D) and AGAPE.

RMSE (in meter)	MLE (2-D)	MLE (4-D)	AGAPE
Experiment 1	2.64	0.92	0.87
Experiment 2	2.98	0.98	1.03
Experiment 3	2.80	0.86	0.87

Table 2.2: Experimental tracking results: RMSEs from KF without gain, KF with gain and OE-EKF.

RMSE (in meter)	KF without gain	KF with gain	OE-EKF
Experiment 1	2.25	0.50	0.44
Experiment 2	2.63	0.57	0.56
Experiment 3	2.37	0.52	0.46

CHAPTER 3

ROBUST ESTIMATORS FOR VARIANCE BASED DEVICE-FREE LOCALIZATION

3.1 Abstract

Human motion in the vicinity of a wireless link causes variations in the link received signal strength (RSS). Tag-free localization systems, such as variance-based radio tomographic imaging (VRTI), use these RSS variations in a static wireless network to locate and track people in the area of the network, even through walls. However, intrinsic motion, such as branches moving in the wind and rotating or vibrating machinery, also causes RSS variations which degrade the performance of a localization system. In this chapter, we propose and evaluate two estimators to reduce the impact of the variations caused by intrinsic motion. One estimator uses subspace decomposition, and the other estimator uses a least squares formulation. Experimental results show that both estimators reduce localization root mean squared error by about 40% compared to VRTI. In addition, the Kalman filter tracking results from both estimators have errors less than 1.3 m, 97% of the time, more than 60% improvement compared to tracking results from VRTI. [1]

3.2 Introduction

As an emerging technology, tag-free localization using radio frequency (RF) sensor networks has potential application in detecting intruders in industrial facilities, and helping police and firefighters track people inside a building during an emergency [55]. In these scenarios, people to be located cannot be expected to participate in the localization system by carrying radio tags, thus standard radio localization techniques are not useful for these applications.

---

[1] This chapter contains copyrighted material, reprinted with permission from Y. Zhao and N. Patwari, "Noise reduction for variance-based device-free localization and tracking," in Proc. of the 8th IEEE Conf. on Sensor, Mesh and Ad Hoc Communications and Networks (SECON'11), Salt Lake City, Utah, U.S., June 2011 and Y. Zhao and N. Patwari, "Robust estimators for variance-based device-free localization and tracking," Tech. Rep. arXive:1110.1569v1, Arxiv.org, Oct. 2011.

Various RF measurements including ultra-wideband (UWB) and received signal strength (RSS) have been proposed and applied to detect, locate and track objects and people who do not carry radio tags in an environment [12, 13, 56, 14, 57, 15]. Compared to cameras and infrared sensing methods, RF sensors have the advantage of penetrating nonmetal walls and smoke [55]. While UWB measurements are expensive, RSS measurements are inexpensive and available in standard wireless devices, and have been used in different tag-free localization studies with surprising accuracy [14, 18, 15]. These RSS-based localization methods essentially use a windowed variance of RSS measured on static links. For example, [15] deploys an RF sensor network around a residential house and uses sample variance during a short window to track people walking inside the house; [18] places RF sensors on the ceiling of a room, and track people using the RSSI dynamic, which is essentially the variance of RSS measurements, with and without people moving inside the room. In this chapter we focus on using RSS measurements to locate and track human motion. We use windowed variance to describe the various functions of RSS measurements recently used in different localization studies [14, 18, 15, 58, 59], and we call these methods variance-based tag-free localization methods.

For variance-based localization methods, variance can be caused by two types of motion: *extrinsic motion* and *intrinsic motion*. Extrinsic motion is defined as the motion of people and other objects that enter and leave the environment. Intrinsic motion is defined as the motion of objects that are intrinsic parts of the environment, objects which cannot be removed without fundamentally altering the environment. If a significant amount of windowed variance is caused by intrinsic motion, then it may be difficult to detect extrinsic motion. For example, rotating fans, leaves and branches swaying in wind, and moving or rotating machines in a factory all may impact the RSS measured on static links. Also, if RF sensors are vibrating or swaying in the wind, their RSS measurements change as a result. Even if the receiver moves by only a fraction of its wavelength, the RSS may vary by several orders of magnitude as a result of small-scale fading [60, 61]. We call variance caused by intrinsic motion and extrinsic motion, the *intrinsic signal* and *extrinsic signal*, respectively. We consider the intrinsic signal to be "noise" because it does not relate to extrinsic motion which we wish to detect and track.

This work is motivated by our inability to achieve the performance of 0.6 m average tracking error reported in [15] in a repeat of the identical experiment in May, 2010. Our new experiment was performed at the same location and using the identical hardware, number of nodes, and software. Yet, in the new experiment, variance-based radio tomographic imaging (VRTI) does not always locate the person walking inside the house as accurately as reported in [15]. Sometimes the position estimate error is as large as six meters, as shown in Figure 3.8. Investigation of the experimental data quickly indicates the reason for the degradation: periods of high wind. Consider the RSS measurements recorded during the calibration period, when no people are present inside the house. From the calibration measurements of [15], the standard deviations of RSS measurements are generally less than 2 dB. However, the RSS measurements from our May 2010 experiment are quite variable, as shown in Figure 3.1. The RSS standard deviation can be up to 6 dB in a short time window. Considering there is no person moving inside the house, that is, no extrinsic motion during the calibration period, the high variations of RSS measurements must be caused by intrinsic motion, in this case, wind-induced motion.

The variance caused by intrinsic motion can affect both model-based and fingerprint-based localization methods. To apply various tag-free localization methods in practical applications, the intrinsic signal needs to be identified and removed or reduced. Since intrinsic motion is an intrinsic part of an environment, we assume calibration measurements contain the type of intrinsic motion that we experience during the real-time operation. We use calibration measurements and propose two methods to improve the robustness of VRTI. The first method uses the subspace decomposition method, which has been used in spectral estimation, sensor array processing, and network anomaly detection [62, 63, 64, 65]. We apply this method to VRTI, which leads to a new estimator we refer to as subspace variance-based radio tomography (SubVRT) [23]. Inspired by the fact that SubVRT makes use of the covariance matrix of link measurement and significantly reduces the impact of intrinsic motion, in this chapter, we formulate a least squares (LS) solution [66] for VRTI which uses the inverse of the covariance matrix. We call this method least squares variance-based radio tomography (LSVRT). While both SubVRT and LSVRT are significantly more robust to intrinsic motion than VRTI, the advantage of LSVRT over SubVRT is that it can change its parameters automatically from calibration measurements, thus we do not need to manually tune any parameter, like k must be tuned in SubVRT.

The contribution of this chapter is to propose and compare two estimators – SubVRT and LSVRT to reduce the impact of intrinsic motion in tag-free localization systems. Experimental results show that both estimators reduce the root mean squared error (RMSE) of the location estimate by more than 40% compared to VRTI. Further, we use the Kalman filter to track people using localization estimates from SubVRT and LSVRT. The cumulative distribution functions (CDFs) of the tracking errors show that the tracking results from

SubVRT have 97% of errors less than 1.4 m, a 65% improvement compared to VRTI, while 97% of tracking errors from LSVRT are less than 1.2 m, a 70% improvement.

The rest of this chapter is organized as follows: Section 4.3 discusses the subspace decomposition method and least squares method for noise reduction in tag-free localization. Section 4.4 describes the experiments, Section 4.5 shows the experimental results, and Section 3.5 investigates the Kalman filter tracking. Related work is presented in Section 3.6, and the conclusion is given in Section 4.6.

In this section, we formulate a variance-based tag-free localization problem, introduce the subspace decomposition method, and propose our SubVRT estimator. After that, we use the measurement covariance matrix in a least squares (LS) formulation and propose another estimator, LSVRT. Finally, we discuss the connection between these two estimators.

3.2.1 Problem statement

For an RF sensor network with N sensors (radio transceivers) deployed at static locations, we use $\mathbf{z}_{s,j}$ to denote the coordinate of sensor j. Each sensor makes an RSS measurement with many other sensors, and we use $s_{l,t}$ to denote the RSS measured at node i_l sent by node j_l at time t, where i_l and j_l are the receiver and transmitter number for link l, respectively. Time t is discretized, thus $t \in \mathbb{Z}$. We assume constant transmitter power so that changes in $s_{l,t}$ are due to the channel, not to the transmitter. Then we denote the windowed RSS variance as:

$$y_{l,t} = \frac{1}{m-1} \sum_{i=0}^{m-1} (\bar{s}_{l,t} - s_{l,t-i})^2 \tag{3.1}$$

where m is the length of the window, and $\bar{s}_{l,t} = \frac{1}{m} \sum_{i=0}^{m-1} s_{l,t-i}$ is the sample average in this window period.

Consider that the network has L directional links on which we measure signal strength (in general, $L \leq N(N-1)$). We let $\mathbf{y}^{(t)} = [y_{1,t}, y_{2,t}, \cdots, y_{L,t}]^T$ be the vector of windowed RSS variance from all L links at time t. If we do not need to represent time, we simplify the notation to $\mathbf{y} = [y_1, y_2, \cdots, y_L]^T$. Then we use $\mathbf{y}_c$ to denote the calibration measurements collected during the calibration period, when no people are present in the environment; and we use $\mathbf{y}_r$ to denote the measurements from the real-time operation period. The goal of tag-free localization is to locate people during real-time operation.

For VRTI, a model-based localization method, the presence of human motion within P voxels of a physical space is denoted by $\mathbf{x} = [x_1, x_2, ..., x_P]^T$, where $x_i = 1$ if extrinsic motion occurs in voxel i, and $x_i = 0$ otherwise. Work in [15] has shown the efficacy of a linear model that relates the motion image $\mathbf{x}$ to the RSS variance $\mathbf{y}_r$:

$$\mathbf{y}_r = W\mathbf{x} + \mathbf{n} \tag{3.2}$$

where $\mathbf{n}$ is an $L \times 1$ noise vector including intrinsic motion and measurement noise, and W is an $L \times P$ matrix representing the weighting of motion in each voxel on each link measurement. The weighting of voxel p on link l is formulated as [15]:

$$W_{l,p} = \frac{1}{\sqrt{d_{i_l,j_l}}} \begin{cases} \phi & \text{if } d_{i_l,p} + d_{j_l,p} < d_{i_l,j_l} + d_w \\ 0 & \text{otherwise} \end{cases} \tag{3.3}$$

where d_{i_l,j_l} is the Euclidean distance between two sensors i_l, j_l on link l located at $\mathbf{z}_{s,i_l}$ and $\mathbf{z}_{s,j_l}$; $d_{j_l,p}$ is the Euclidean distance between sensor j_l and $\mathbf{z}_p$, the center coordinate of voxel p; $d_{i_l,p}$ is the Euclidean distance between sensor i_l and voxel p; d_w is a tunable parameter controlling the ellipse width, and ϕ is a constant scaling factor.

Once we have the forward model, the localization problem becomes an inverse problem: to estimate P dimensional position vector $\mathbf{x}$ from L dimensional link measurement vector $\mathbf{y}_r$. Certain regularization methods are necessary for this ill-posed inverse problem, and it is shown in [15] that submeter localization accuracy can be achieved by using the Tikhonov regularization. Thus, we use the Tikhonov regularized VRTI solution, which is given as:

$$\begin{aligned} \hat{\mathbf{x}} &= \Pi_1 \mathbf{y}_r \\ \Pi_1 &= (W^T W + \alpha Q^T Q)^{-1} W^T \end{aligned} \tag{3.4}$$

where Q is the Tikhonov matrix, and α is a regularization parameter.

3.2.2 Subspace decomposition method

3.2.2.1 Subspace decomposition

The subspace decomposition method has been widely used in spectral estimation, sensor array processing, etc. [62, 65] to improve estimation performance in noise. It is closely related to principal component analysis (PCA), which is widely used in finding patterns in high dimensional data [67].

From the L-dimensional calibration measurement vector $\mathbf{y}_c$, we may estimate its covariance matrix $C_{\mathbf{y}_c}$ as:

$$C_{\mathbf{y}_c} = \frac{1}{M-1} \sum_{t=0}^{M-1} (\mathbf{y}_c^{(t)} - \boldsymbol{\mu}_c)(\mathbf{y}_c^{(t)} - \boldsymbol{\mu}_c)^T = AA^T \tag{3.5}$$

where M is the number of sample measurements, $\mathbf{y}_c^{(t)}$ is the calibration measurement vector $\mathbf{y}_c$ at time t, $\boldsymbol{\mu}_c = \frac{1}{M}\sum_{t=0}^{M-1}\mathbf{y}_c^{(t)}$ is the sample average, and $A = \frac{1}{\sqrt{M-1}}[\mathbf{y}_c^{(0)} - \boldsymbol{\mu}_c, \cdots, \mathbf{y}_c^{(M-1)} - \boldsymbol{\mu}_c]$ is an $L \times M$ matrix.

Instead of directly performing singular value decomposition (SVD) on $C_{\mathbf{y}_c}$, we perform SVD on an $M \times M$ matrix $A^T A$ [68]:

$$A^T A \mathbf{v}_i = \gamma_i \mathbf{v}_i \tag{3.6}$$

where $\mathbf{v}_i$ is the eigenvector corresponding to the eigenvalue γ_i. Right multiplying A on both sides of (3.6), we obtain [68]:

$$A A^T A \mathbf{v}_i = \gamma_i A \mathbf{v}_i \tag{3.7}$$

From (3.7), we see $\mathbf{u}_i = A\mathbf{v}_i$ is the ith eigenvector and γ_i is the ith eigenvalue of $C_{\mathbf{y}_c}$.

If the eigenvalues are in descending order, the first principal component $\mathbf{u}_1$ points in the direction of the maximum variance in the measurement, the second principal component $\mathbf{u}_2$ points in the direction of the maximum variance remaining in the measurement, and so on. If the first few eigenvalues are much larger than the others, then most of the variance in the measurements can be captured by these principal components.

We perform PCA on calibration measurements from two sets of experiments as described in Section 4.4. The eigenvalues of $C_{\mathbf{y}_c}$ from these experiments are shown in Figure 3.6. Because there is more intrinsic motion in Experiment 2, we see that the largest eigenvalue from Experiment 2 is almost twice as large as that from Experiment 1. We also see that for Experiment 1, the first four eigenvalues are much larger than the other eigenvalues, thus the corresponding eigenvectors can capture most of the variation in the measurements. However, for Experiment 2, there are more large-valued eigenvalues, and more eigenvectors are necessary to represent the major variation in the measurements. From the scree plot, we decide how many principal components, k, are necessary to capture the majority of the variations. Then, we use a lower dimensional space spanned by these principal components to represent the space containing the majority of the intrinsic signal measurements. This is the basic idea of the subspace decomposition method, which we discuss next.

In subspace decomposition, we divide all the principal components into two sets: $\hat{U} = [\mathbf{u}_1, \mathbf{u}_2, \cdots, \mathbf{u}_k]$ and $\tilde{U} = [\mathbf{u}_{k+1}, \mathbf{u}_{k+2}, \cdots, \mathbf{u}_L]$. Then, we decompose the measurement space into two lower dimensional subspaces spanned by $\hat{U}$ and $\tilde{U}$. Since the variance during the calibration period is caused by intrinsic motion, that is, the variance captured by $\hat{U}$ is intrinsic signal, we call the subspace spanned by $\hat{U}$ the intrinsic subspace, and the other subspace spanned by $\tilde{U}$ the extrinsic subspace. Once the two subspaces are constructed, we can decompose the measurement vector $\mathbf{y}$ into two components – intrinsic signal component $\hat{\mathbf{y}}$ and extrinsic signal component $\tilde{\mathbf{y}}$:

$$\mathbf{y} = \hat{\mathbf{y}} + \tilde{\mathbf{y}} \tag{3.8}$$

Since the principal components are orthogonal, the intrinsic signal component $\hat{\mathbf{y}}$ and the extrinsic signal component $\tilde{\mathbf{y}}$ can be formed by projecting $\mathbf{y}$ onto the intrinsic subspace and the extrinsic subspace, respectively:

$$\hat{\mathbf{y}} = \Pi_I \mathbf{y} = \hat{U}\hat{U}^T \mathbf{y} \tag{3.9}$$

$$\tilde{\mathbf{y}} = \Pi_E \mathbf{y} = (I - \hat{U}\hat{U}^T)\mathbf{y} \tag{3.10}$$

where $\Pi_I = \hat{U}\hat{U}^T$ is the projection matrix for the intrinsic subspace, and $\Pi_E = I - \Pi_I$ is the projection matrix for the extrinsic subspace.

Using the procedures discussed above, we decompose the windowed RSS variance measurements $\mathbf{y}_c$ from the calibration period of Experiment 2 into intrinsic signal component $\hat{\mathbf{y}}_c$ and extrinsic signal component $\tilde{\mathbf{y}}_c$. We test a range of principal component number k in constructing the intrinsic subspace. The decomposed intrinsic and extrinsic signal components for measurement on one link $l = 588$ using different k are shown in Figure 3.3. We see that if all principal components are used in constructing $\hat{U}$, that is, $k = L$, then $\hat{\mathbf{y}}_c$ is equivalent to the original measurement $\hat{\mathbf{y}}_c = \mathbf{y}_c$, while $\tilde{\mathbf{y}}_c$ is zero. If the first 100 principal components are used, since they capture most of the variance in the measurement, from Figure 3.3(b) we see $\hat{\mathbf{y}}_c$ is almost the same as the original measurement. If we only use the first 40 eigenvectors, $\hat{\mathbf{y}}_c$ still matches the original measurement, as shown in Figure 3.3(a). That is, the first 40 principal components are sufficient to capture the majority of the variations in the measurements. Since each of the principal components used to construct the intrinsic subspace is an eigenvector of the covariance matrix of the network measurements, and each element in an eigenvector is from an individual link, we refer these eigenvectors as “eigen-networks.”

In the above subspace decomposition derivation, we perform SVD on the matrix $A^T A$ instead of AA^T. For a network with N sensors, there are $O(N^2)$ pairwise links, and the covariance matrix $C_{\mathbf{y}_c}$ is an $N^2 \times N^2$ matrix. Since the computational complexity of performing SVD on a $L \times L$ matrix is $O(L^3)$ [69], that is, $O(N^6)$ for $C_{\mathbf{y}_c}$, directly performing SVD on high dimensional covariance matrix requires too much computation that increases quickly with N. Since the number of sample measurements is generally much lower than the number of links, $M < N^2$, this method greatly reduces the computational complexity of performing SVD from $O(N^6)$ to $O(M^3)$.

3.2.2.2 SubVRT algorithm

The key idea of SubVRT is to use the decomposed extrinsic signal component of the measurements in VRTI. We project the real-time measurement vector $\mathbf{y}_r$ onto the extrinsic subspace to obtain the extrinsic signal component $\tilde{\mathbf{y}}_r = (I - \hat{U}\hat{U}^T)\mathbf{y}_r$. Then, we replace $\mathbf{y}_r$ in (3.4) with $\tilde{\mathbf{y}}_r$ and obtain the solution of SubVRT:

$$\hat{\mathbf{x}} = \Pi_2 \mathbf{y}_r \quad \text{where } \Pi_2 = (W^T W + \alpha Q^T Q)^{-1} W^T \Pi_E \tag{3.11}$$

From (3.11), we see that the solution is a linear transformation of the measurement vector. The transformation matrix Π_2 is the product of the transformation matrix Π_1 in (3.4) with the projection matrix for the extrinsic subspace Π_E: $\Pi_2 = \Pi_1 \Pi_E$. Since the transformation matrix Π_2 does not depend on instantaneous real-time measurements, it can be pre-calculated, and it is easy to implement SubVRT for real-time applications.

We note that a major difference from VRTI is that SubVRT needs calibration, which results in Π_E that is unique to the environment. However, calibration only requires that no extrinsic motion is present in the environment. In contrast to fingerprint-based DFL methods, SubVRT does not require *training*, *i.e.*, that a person (or combinations of people) stands at all possible locations. Possible online calibration of SubVRT, and the trade-offs between calibration duration and localization accuracy, are left as future research topics.

3.2.3 Least squares method

SubVRT performs SVD on the calibration measurement covariance matrix. Here, we introduce our LSVRT estimator formulated as a least squares (LS) solution, which uses the inverse of the covariance matrix.

3.2.3.1 Formulation

To derive the least squares solution to the linear model expressed in (3.2), the cost function can be written as [66]:

$$\begin{aligned} J(\mathbf{x}) &= \|W\mathbf{x} - \mathbf{y}_r\|^2_{C_\mathbf{n}} + \|\mathbf{x} - \mathbf{x}_a\|^2_{C_\mathbf{x}} \\ &= (\mathbf{y}_r - W\mathbf{x})^T C_\mathbf{n}^{-1} (\mathbf{y}_r - W\mathbf{x}) + (\mathbf{x} - \mathbf{x}_a)^T C_\mathbf{x}^{-1} (\mathbf{x} - \mathbf{x}_a) \end{aligned} \tag{3.12}$$

where $\|\mathbf{n}\|^2_{C_\mathbf{n}}$ indicates weighted quadratic distance $\mathbf{n}^T C_\mathbf{n}^{-1} \mathbf{n}$, $C_\mathbf{n}$ is the covariance matrix of $\mathbf{n}$, $\mathbf{x}_a$ is the prior mean of $\mathbf{x}$, and $C_\mathbf{x}$ is the covariance matrix of $\mathbf{x}$.

Taking the derivative of (3.12) and setting it to zero results in the LSVRT solution:

$$\hat{\mathbf{x}}_{LS} = (W^T C_\mathbf{n}^{-1} W + C_\mathbf{x}^{-1})^{-1} (W^T C_\mathbf{n}^{-1} \mathbf{y}_r + C_\mathbf{x}^{-1} \mathbf{x}_a). \tag{3.13}$$

Since the prior information $\mathbf{x}_a$ can be included in the tracking period, here we assume $\mathbf{x}_a$ is zero, then (3.13) becomes:

$$\begin{aligned}\hat{\mathbf{x}}_{LS} &= \Pi_3 \mathbf{y}_r \\ \Pi_3 &= (W^T C_{\mathbf{n}}^{-1} W + C_{\mathbf{x}}^{-1})^{-1} W^T C_{\mathbf{n}}^{-1}.\end{aligned} \tag{3.14}$$

The LSVRT formulation can be also justified from a Bayesian perspective. If we assume $\mathbf{y}_r$ conditioned on $\mathbf{x}$ is Gaussian distributed with mean $W\mathbf{x}$ and covariance matrix $C_{\mathbf{n}}$, and $\mathbf{x}$ is Gaussian distributed with mean $\mathbf{x}_a$ and covariance matrix $C_{\mathbf{x}}$, maximizing the posteriori distribution $p(\mathbf{x}|\mathbf{y}_r)$ is equivalent to minimizing the cost function in (3.12). Thus the LS solution (3.13) can also be seen as the maximum a posteriori (MAP) solution under the Gaussian assumptions.

3.2.3.2 Covariance matrix $C_{\mathbf{n}}$

From the LSVRT solution (3.13), we see that the inverse of the covariance matrix $C_{\mathbf{n}}$ (a.k.a., the precision matrix) is needed. We may use the sample covariance matrix if the sample size M of the calibration measurements is greater than the number of link measurements L. However, for an RF sensor network with L (on the order of thousand) directional links, M (on the order of hundred) is typically less than L. Thus, for high dimensional problems, the sample covariance matrix becomes an ill-posed estimator, it cannot be inverted to compute the precision matrix.

For high dimensional covariance matrix estimation problems, many types of regularized covariance matrix estimators have been proposed [70, 71]. Here, we use the Ledoit-Wolf estimator, which is a linear combination of the sample covariance matrix and a scaled identity matrix, and is shown to be asymptotically optimal for any distribution [70]:

$$C_{\mathbf{n}} = \nu\mu I + (1-\nu) C_{\mathbf{n}}^{*} \tag{3.15}$$

where $C_{\mathbf{n}}^{*}$ is the sample covariance matrix, μ is the scaling parameter for the identity matrix I, and ν is the shrinkage parameter that shrinks the sample covariance towards the scaled identity matrix. Since there is no extrinsic motion during calibration period, that is, $\mathbf{x} = 0$, thus $\mathbf{y}_c = \mathbf{n}$, and we approximate $C_{\mathbf{n}}^{*} = C_{\mathbf{y}_c}$. Then we follow the procedures in [70] to calculate parameters ν and μ from the calibration measurements. From the Bayesian perspective, this covariance matrix estimator can be seen as the combination of the prior information and sample information of the covariance matrix.

3.2.3.3 Covariance matrix $C_{\mathbf{x}}$

The LSVRT solution also requires the covariance matrix $C_{\mathbf{x}}$. As a means to generate a general statistical model for $C_{\mathbf{x}}$, we assume that the positions of people in the environment can be modeled as a Poisson process. Poisson processes are commonly used for modeling the distribution of randomly arranged points in space.

Analysis of Poisson point processes leads to a covariance function that is approximately exponentially decaying [72], and the exponential spatial covariance model is shown to be effective to locate people in an RF sensor network [15]. Thus, in this chapter, we use an exponentially-decaying function as the covariance matrix of the human motion.

$$C_{\mathbf{x}} = \frac{\sigma_x^2}{\delta} \exp\left(-\frac{\|\mathbf{x}_j - \mathbf{x}_i\|_{l_2}}{\delta}\right) \tag{3.16}$$

where σ_x^2 is the variance of the human motion, δ is a space constant, and $\|\mathbf{x}_j - \mathbf{x}_i\|_{l_2}$ is the Euclidian distance between $\mathbf{x}_i$ and $\mathbf{x}_j$.

3.2.4 Discussion

The SubVRT estimator and the LSVRT estimator are closely related. LSVRT needs to calculate the inverse of the covariance matrix $C_{\mathbf{n}}$, while SubVRT needs to perform SVD on the sample covariance matrix $C_{\mathbf{y}_c}$. In this section, we show connections between these two estimators.

First, for SubVRT, once we choose the parameter k, we can find a diagonal matrix $S = \text{diag}\left\{\underbrace{0, 0, \cdots, 0}_{k}, 1, 1, \cdots, 1\right\}$ such that $USU^T = I - \hat{U}\hat{U}^T$. Then, the project matrix for the SubVRT solution can be rewriten as:

$$\Pi_2 = (W^T W + \alpha Q^T Q)^{-1} W^T U S U^T. \tag{3.17}$$

For the LSVRT solution (3.14) and the Ledoit-Wolf covariance estimator in (3.15), if we approximate $C_{\mathbf{n}}^* = C_{\mathbf{y}_c}$, then the inverse of $C_{\mathbf{n}}$ can be written as:

$$C_{\mathbf{n}}^{-1} = \frac{1}{\nu\mu} I + \frac{1}{1-\nu} C_{\mathbf{y}_c}^{-1}. \tag{3.18}$$

Substituting (3.5) in (3.18), we express $C_{\mathbf{n}}^{-1}$ in terms of Λ:

$$C_{\mathbf{n}}^{-1} = U c_1 (\Lambda^{-1} + c_2 I) U^T \tag{3.19}$$

where $c_1 = \frac{1}{1-\nu}$, and $c_2 = \frac{1-\nu}{\nu\mu}$. Replacing the second $C_{\mathbf{n}}^{-1}$ in (3.14) by (3.19), the project matrix for the LSVRT solution becomes:

$$\Pi_3 = (W^T C_{\mathbf{n}}^{-1} W + C_{\mathbf{x}}^{-1})^{-1} W^T U c_1 (\Lambda^{-1} + c_2 I) U^T. \tag{3.20}$$

Now we compare the two projection matrices (3.17) and (3.20) in the SubVRT and LSVRT solutions. From the latter part of (3.20), we see that LSVRT uses $c_1(\Lambda^{-1} + c_2 I)$ to give less weights to the linear combinations of measurements in the eigen-space with high variance (large eigenvalues). For SubVRT, the diagonal matrix S in (3.17) is used to directly remove eigenvectors that correspond to the first k largest eigenvalues. From the former part of (3.17) and (3.20), we see that the inverse of the covariance matrix $C_{\mathbf{x}}^{-1}$ in the LSVRT solution plays the same role of regularization as the term $\alpha Q^T Q$ in the SubVRT solution. We also see that the LSVRT estimator includes the precision matrix $C_{\mathbf{n}}^{-1}$ as a weight matrix in $W^T C_{\mathbf{n}}^{-1} W$, while the SubVRT estimator just uses $W^T W$.

3.3 Experiments

We use measurements from two sets of experiments in this chapter. We use the data set from the measurements conducted in March, 2009 reported by [15]. We call this data set Experiment 1. The second experiment is a new experiment performed in May, 2010 at the same residential house, which we call Experiment 2. In both experiments, 34 TelosB nodes are deployed outside the living room of the house. As shown in Figure 3.5, eight nodes are placed on the table in the kitchen, six nodes are placed on boards extended outside the windows of the living room. The other 20 nodes are all placed on polyvinyl chloride (PVC) stands outside the house. All 34 nodes are programmed with TinyOS program Spin [7], and a basestation connected to a laptop is used to collect pairwise RSS measurements from these nodes.

Both experiments are performed using the following procedure. Before people start to walk in the living room, a calibration is performed with no people (no extrinsic motion) in the experimental area. The duration of the calibration period of Experiment 1 is about 47 seconds, and $M = 140$ measurements are recorded for each link; while for Experiment 2, $M = 170$ measurements are recorded for each link during a 57 second calibration period. Compared to $L = 1122$ directional links, M is much smaller than L. Next, a person walks around a marked path (A-B-C-D as shown in Figure 3.17) in the living room at a constant speed of about 0.5 m/s, using a metronome and a metered path so that the position of the person at any particular time is known. Note that the transmission interval between two nodes is set by the Spin protocol so that three link measurements are recorded each second to match the speed of human motion. For faster human motion, we can increase the transmission frequency at the cost of more power consumption.

These two through-wall experiments use the same hardware and software, and are performed following the same procedure. However, the main difference between these two experiments is the season. Experiment 1 is performed on a clear winter day, while Experiment 2 is performed on a windy day in late spring. As shown in our video [73] (a snapshot is shown in Figure 3.4(a)), there are no leaves on branches and no wind is observed during Experiment 1. However, from the video recorded during Experiment 2 (one snapshot is shown in Figure 3.4(b)), we observe that wind causes grass, leaves and branches to sway [73]. The wind also causes the PVC stands supporting the nodes to move. The swaying of leaves and branches and the movement of the PVC stands are intrinsic parts of the environment, which cannot be avoided, even when no people are present in the environment. Thus, the difference between Experiments 1 and 2 is that Experiment 2 has more intrinsic motion.

3.4 Results

3.4.1 Eigenvalues and eigen-networks

First, we perform PCA as described in Section 3.2.2 on calibration measurements from Experiments 1 and 2. The eigenvalues of $C_{\mathbf{y}_c}$ from these two experiments are shown in Figure 3.6. Because there is more intrinsic motion in Experiment 2, we see that the largest eigenvalue from Experiment 2 is almost twice as large as that from Experiment 1. We also see that for Experiment 1, the first four eigenvalues are much larger than the other eigenvalues, thus the corresponding eigenvectors can capture most of the variation in the measurements. However, for Experiment 2, there are more large-valued eigenvalues, and more eigenvectors are necessary to represent the major variation in the measurements.

Since each of the principal components used to construct the intrinsic subspace is an eigenvector of the covariance matrix of the network measurements, and each element in an eigenvector is from an individual link, we refer these eigenvectors $\mathbf{u}_i$ as “eigen-networks.” The first eigen-network $\mathbf{u}_1 = [u_{11}, u_{12}, \cdots, u_{1L}]^T$ points in the direction of the maximum variance of the calibration measurements $\mathbf{y}_c$, we show the first eigen-network $\mathbf{u}_1$ graphically in Figure 3.7. We see the links with u_{1l} values higher than 30% of the maximum value are all in the lower right side of the house. This is consistent with our observation that the intrinsic motion of the leaves and branches on the tree located to the right side of the house causes significant variations in the RSS measured on links likely to have RF propagation through the branches and leaves. Note that links with high u_{1l} values all have at least one end point near the tree. In particular, links which are likely to see significant diffraction around the bottom-right corner of the house have high u_{1l} values. The leaves and branches almost touch this corner, as seen in Figure 3.4(b). Not only do these links measure high RSS variance during the calibration period, they do so simultaneously. That is, the fact that these links have high positive u_{1l} values indicates that when one of these links experiences increased RSS variance, the other links also measure increased RSS variance. Thus, the first eigen-network $\mathbf{u}_1$ becomes a spatial signature for intrinsic motion-induced RSS variance. When we see this linear combination in $\mathbf{y}_r$, we should attribute it to intrinsic, rather than extrinsic motion. These observations about the source of RSS variance on links support the idea that intrinsic motion in the environment causes increased RSS variance simultaneously on multiple links.

3.4.2 Localization results

Now, we evaluate VRTI, SubVRT and LSVRT using measurements from Experiments 1 and 2. From these three estimators, we obtain reconstructed motion images, and the position of the moving person can be estimated by finding the center coordinate of the voxel with maximum value. Specifically, a localization estimate is defined as:

$$\hat{\mathbf{z}} = \mathbf{z}_q \quad \text{where} \quad q = \arg\max_p \hat{x}_p$$

where $\mathbf{z}_q$ is the center coordinate of voxel q, and $\hat{x}_p$ is the pth element of the estimate $\hat{\mathbf{x}} = [\hat{x}_1, \hat{x}_2, ..., \hat{x}_P]^T$ from (3.4), (3.11) or (3.14). Then, the localization error is defined as: $e_{loc} = \|\hat{\mathbf{z}} - \mathbf{z}\|_{l_2}$, where $\mathbf{z}$ is the actual position of the person, and l_2 indicates the Euclidean norm.

The VRTI estimates of Experiment 2 are shown in Figure 3.8. For clarity, we only show the actual/estimated positions when the person walks the last round of the square. We find that due to the impact of intrinsic motion, some estimates of VRTI are greatly biased to the right side of the experimental area (i.e., five estimates with more than 4.0 m error, as shown in Figure 3.8). However, for SubVRT and LSVRT, the impact of intrinsic motion is greatly reduced. As shown in Figure 3.9 and Figure 3.10, the estimates from SubVRT and LSVRT are more accurate than VRTI. There are no estimate errors larger than 2.0 m. Note that for both VRTI and SubVRT, some estimates are outside the house. The algorithms presented do not include any prior information of the house map or physical barriers which would prevent certain trajectories. Incorporation of prior knowledge of an indoor environment might be used to obtain better estimates, but at the expense of requiring more information to deploy the system.

Quantatively, we compare the localization errors from VRTI, SubVRT and LSVRT for the full data set. The comparison between VRTI and SubVRT is shown in Figure 3.11, and the comparison between VRTI and LSVRT is shown in Figure 3.12. The localization errors from SubVRT are all below 1.8 m. For VRTI, there are several estimates with errors above 3.0 m. These large errors are due to the impact of intrinsic motion on static link measurements. Specifically, we compare the localization errors during a period with strong wind, from sample index 205 to 221, as shown in the inset of Figure 3.11. During this period, the average localization error from VRTI is 3.0 m, while the average error from SubVRT is 0.62 m, a 79% improvement, and for LSVRT, it is only 0.50 m, a 83% improvement. Note that these two experiments only last for several minutes. For long-term deployment, environmental conditions may change and the performance of our system may degrade. Thus, periodical re-calibration may be necessary to capture environmental changes during a long-term deployment.

We also compare the RMSE of the estimates, which is defined as the square root of the average squared localization error over the course of the entire experiment. The RMSEs from the two experiments are summarized in Table 3.1. For Experiment 1, the RMSE from VRTI is 0.70 m, while the RMSE from SubVRT is 0.65 m, a 7.0% improvement and the RMSE from LSVRT is 0.63 m, a 9.6% improvement. Note that there is not much intrinsic motion in Experiment 1, our SubVRT and LSVRT estimators still outperform VRTI. This shows that these two estimators are robust to other noise effects, such as RSS measurement noise due to nonideal hardware components. For Experiment 2, the RMSE from VRTI is 1.26 m, while SubVRT and LSVRT are more robust to impact of intrinsic motion. The RMSE from SubVRT is 0.74 m, a 41.3% improvement, and the RMSE from LSVRT is 0.69 m, a 45.3% improvement.

3.4.3 Discussion

The parameters that we use in VRTI, SubVRT and LSVRT are listed in Table 3.2. We show the effect of the number of nodes on these three algorithms. We also discuss the effects of the number of principal components k and the covariance matrix parameter σ_x^2 on the performances of SubVRT and LSVRT, respectively.

To see the effect of node numbers on the localization performance, we run VRTI, SubVRT and LSVRT algorithms using RSS measurements from only a randomly chosen subset N less than the 34 total nodes used in Experiment 1. For example, when we use $N = 20$ nodes, we randomly choose 20 of the measured nodes, and then run our algorithms using the RSS measurements collected between pairs of these 20 nodes. For each N, we repeat the above procedure 100 times, and each time calculate the RMSEs of the position estimates. The average RMSEs and the RMSE standard deviations of the three algorithms from Experiment 1 are shown in Figure 3.13, for $N = 20$ to 34 (a node density of 0.27 per m^2 to 0.47 per m^2). We find if we only use 26 nodes ($L = 650$) to cover this 9 m by 8 m area, the average RMSEs from three algorithms are all above 2 m. Comparing results from $N = 26$ vs. $N = 32$, the RMSE reduces by a factor of $3 - 3.6$ for the three methods. For all methods, increasing N may lead to diminishing returns beyond $N = 32$. We also find that the performance of LSVRT is consistently better than SubVRT and VRTI independent of numbers of nodes.

An important parameter for SubVRT is the number of principal components used to construct the intrinsic subspace. As discussed in Section 3.2.2, the first k components are used to calculate the projection matrix for the intrinsic subspace Π_I. If $k = 0$, $\Pi_I = 0$, then $\Pi_1 = \Pi_2$, SubVRT is simplified to VRTI. The RMSEs of SubVRT using a range of k are shown in Figure 3.14. Since the first eigen-network $\mathbf{u}_1$ captures the strongest intrinsic signal, when $k = 1$, the RMSE of Experiment 2 decreases substantially from 1.26 m to 0.82 m. Since Experiment 1 has less intrinsic motion, the RMSE decreases from 0.70 m when $k = 0$ to 0.65 m when $k = 4$, a less substantial decrease. We note that as k increases, more and more information in the measurement is removed, and the RMSE stops decreasing dramatically, and even increases, at certain k. This is because when k becomes very large, the information removed also contains a great amount of signal caused by extrinsic (human) motion. Thus, the performance of SubVRT could be degraded if k is chosen to be too large. The parameter k is a tradeoff between removing intrinsic motion impact and keeping useful information from extrinsic motion. For experiments without much intrinsic motion, such as Experiment 1, we choose a small k. However, for Experiment 2, with strong impact from intrinsic motion, we use a large k. As listed in Table 3.2, we use $k = 4$ and $k = 36$ for Experiments 1 and 2, respectively.

An advantage of LSVRT over SubVRT is that LSVRT can change its parameters automatically based on calibration measurements, thus we do not need to manually tune parameters like k in SubVRT. Thus, we only investigate parameter σ_x^2 in LSVRT, which plays the same role of the regularization parameter α in SubVRT. From Figure 3.15, we see the RMSE from LSVRT reaches the minimum at 0.63 m, when $\sigma_x^2 = 0.001$ and $m = 4$. However, the RMSEs from LSVRT are shallow functions of σ_x^2 in the range from 10^{-4} to 10^{-1}. That is, LSVRT is not sensitive to this parameter in a wide range.

3.5 Tracking

In this section, we apply a Kalman filter to the localization estimates shown in Section 3.4.2 to better estimate moving people's positions over time. Then, we compare the tracking results from VRTI with those from SubVRT and LSVRT, and show that the Kalman filter tracking results from SubVRT and LSVRT are more robust to large localization errors.

3.5.1 Kalman filter

In the state transition model of the Kalman filter, we include both position (P_x, P_y) and velocity (V_x, V_y) in the Cartesian coordinate system in the state vector $\mathbf{s} = [P_x, P_y, V_x, V_y]^T$, and the state transition model is:

$$\mathbf{s}[t] = G\mathbf{s}[t-1] + \mathbf{w}[t] \tag{3.21}$$

where $\mathbf{w} = [0, 0, w_x, w_y]^T$ is the process noise, and G is:

$$G = \begin{bmatrix} 1 & 0 & 1 & 0 \\ 0 & 1 & 0 & 1 \\ 0 & 0 & 1 & 0 \\ 0 & 0 & 0 & 1 \end{bmatrix}. \tag{3.22}$$

The observation inputs $\mathbf{r}[t]$ of the Kalman filter are the localization estimates from VRTI, SubVRT or LSVRT at time t, and the observation model is:

$$\mathbf{r}[t] = H\mathbf{s}[t] + \mathbf{v}[t] \tag{3.23}$$

where $\mathbf{v} = [v_x, v_y]^T$ is the measurement noise, and H is:

$$H = \begin{bmatrix} 1 & 0 & 0 & 0 \\ 0 & 1 & 0 & 0 \end{bmatrix}. \tag{3.24}$$

In the Kalman filter, v_x and v_y are zero-mean Gaussian with variance σ_v^2, w_x and w_y are zero-mean Gaussian with variance σ_w^2 [48]. The parameters σ_v^2 and σ_w^2 of the measurement noise and process noise are listed in Table 3.2.

3.5.2 Tracking results

We use the Kalman filter described above to track the positions of the person. The cumulative distribution functions (CDFs) of the tracking errors from Experiment 2 are shown in Figure 3.16. We see that the Kalman filter tracking results from VRTI have many more large errors than SubVRT and LSVRT. 97% of the tracking errors from VRTI are less than 3.91 m, while 97% of the tracking errors from SubVRT are less than 1.36 m, a

65.2% improvement, and 97% of the errors from LSVRT are less than 1.15 m, a 70.6% improvement. We use the 97^{th} percentile of errors to show the robustness of the tracking algorithm to large errors, and the CDFs show the tracking results from SubVRT and LSVRT are more robust to these large errors.

We also compare the RMSEs of the tracking results from VRTI, SubVRT and LSVRT, which are listed in Table 3.3. For Experiment 1, the tracking RMSEs from SubVRT and LSVRT are both 0.57 m, a 13.6% improvement compared to the RMSE of 0.66 m from VRTI. For Experiment 2, the tracking RMSE from SubVRT is reduced by 40.5% to 0.72 m compared to 1.21 m RMSE from VRTI, and the RMSE from LSVRT is reduced by 45.5% to 0.66 m. We note that the tracking RMSEs from VRTI, SubVRT and LSVRT of Experiment 2 are both larger than Experiment 1 due to the impact of intrinsic motion. However, for VRTI the tracking RMSE from Experiment 2 has a 83.3% increase compared to Experiment 1, while for SubVRT and LSVRT, they only increases 26.3% and 15.8%, respectively. The tracking RMSEs from SubVRT and LSVRT are more robust to the impact of intrinsic motion. Finally, the Kalman filter tracking results of Experiment 2 from SubVRT and LSVRT are shown in Figure 3.17. For Experiment 2 with significant intrinsic motion, the Kalman filter results using SubVRT and LSVRT estimates can still track a person with submeter accuracy.

3.5.3 Discussion

In the Kalman filter, the process noise parameter σ_w^2 should be chosen according to the dynamics of the movement. For example, for tracking vehicles, σ_w^2 should be set to a large value. The measurement noise parameter σ_v^2 depends on how accurate the observation inputs are. Here, we choose σ_w^2 based on the speed of moving people in typical homes, and we test the effect of using different σ_v^2 on the tracking errors. The tracking RMSEs from SubVRT for Experiments 1 and 2 are shown as functions of σ_v^2 in Figure 3.18. If σ_v^2 is too large, the Kalman filter gives very small weights to observation inputs. On the other hand, for very small measurement noise parameter, the system dynamic model contributes little to the Kalman filter. Thus, the RMSE reaches the minimum when an appropriate balance between observation inputs and dynamic model is found. We also note from Figure 3.18 that for both Experiments, the RMSEs are shallow functions of σ_v^2 in a wide range from 0.001 to 20. That is, if we give sufficient weights to the observation inputs, which are the localization estimates from SubVRT and LSVRT, our Kalman filter tracking results are not very sensitive to the measurement noise parameter.

3.6 Related work

For localization and mapping in wireless sensor networks, different measurements, algorithms and frameworks have been proposed [14, 18, 58, 15, 16, 74]. For RSS-based localization methods, there are essentially two types of algorithms: fingerprint-based algorithms and model-based algorithms. Like fingerprint-based real-time location service (RTLS) systems, fingerprint-based tag-free localization methods use a database of training measurements, and estimate people's locations by comparing the measurements during the online phase with the training measurements [18, 58, 20]. Since a separate training measurement dataset is necessary, fingerprint-based method needs substantial training effort. As the number of people to be located increases, the training requirement increases exponentially. Since fingerprint-based methods need a "radio map" from training period, it is not applicable for emergency scenarios, in which training data may not be available.

Model-based algorithms [15, 22, 25] provide another approach. A forward model is used to relate measurements with unknown people's positions, and the localization problem can be solved as an inverse problem. An advantage of a model-based algorithm is that it does not need training measurements, however, sufficient link measurements are necessary to solve the inverse problem. The mean-based radio tomographic imaging (RTI) uses the attenuation effect of the human body to locate stationary and moving people in outdoor environments [22]. However, this method does not perform well in nonLOS multipath-rich environments. For indoor environments where multipath is common, variance-based radio tomographic imaging (VRTI) [15] can locate moving people without any training or calibration measurements. Thus, VRTI can be used in emergency situations for police and firefighters. However, VRTI cannot locate people if they stand still without any motion, and it is sensitive to other motion in the environment.

Our SubVRT and LSVRT estimators are proposed to improve the robustness of a variance-based localization method. Both estimators need offline calibration when no people are present in the environment to capture the intrinsic motion. From our experience over many experiments, a trained eye can look at an unlabelled plot of RSS over time on a link and identify when a human was obstructing the link vs. when no human was present. Thus, we believe that one may develop online algorithms to identify time periods as either with or without extrinsic motion, for example, by solving a hidden Markov model [75]. Using such algorithms, we could build models for intrinsic motion during online operation. Finally, the subspace decomposition and least squares-based formulations similar to those presented in this chapter may be used to improve the performance of mean-based RTI. We leave this for future research.

3.7 Conclusion

In this chapter, we propose to use subspace decomposition and least squares estimation to reduce noise in RSS variance-based tag-free localization and tracking. We discuss how intrinsic motion, such as moving leaves, increase measured RSS variance in a way that is “noise” to a localization system. The signal caused by intrinsic motion has a spatial signature, which can be removed by the subspace decomposition method. We apply the subspace decomposition method to the variance-based localization method, a new estimator we call SubVRT. We also propose an LSVRT estimator that does not need manually tuning parameters as in SubVRT. Experimental results show that SubVRT and LSVRT can reduce localization RMSE by more than 40%. We further apply a Kalman filter on SubVRT and LSVRT estimates for tracking. We find the tracking results from SubVRT and LSVRT are much more robust to large errors.

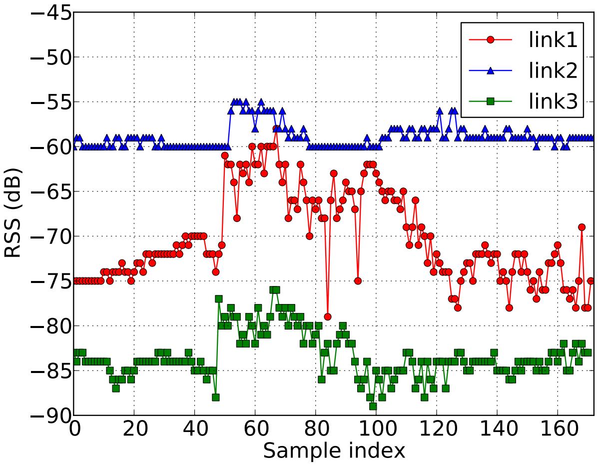

Figure 3.1: Intrinsic signal measurements: RSS measurements from three links during the calibration period (when no people are present in the environment) of one experiment, in which we observe significant wind-induced intrinsic motion.

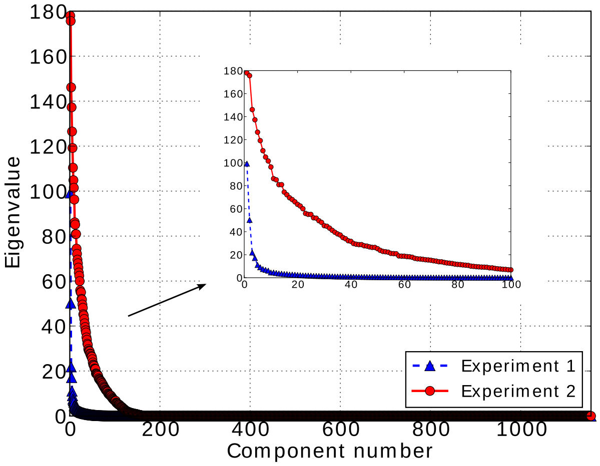

Figure 3.2: Scree plot.

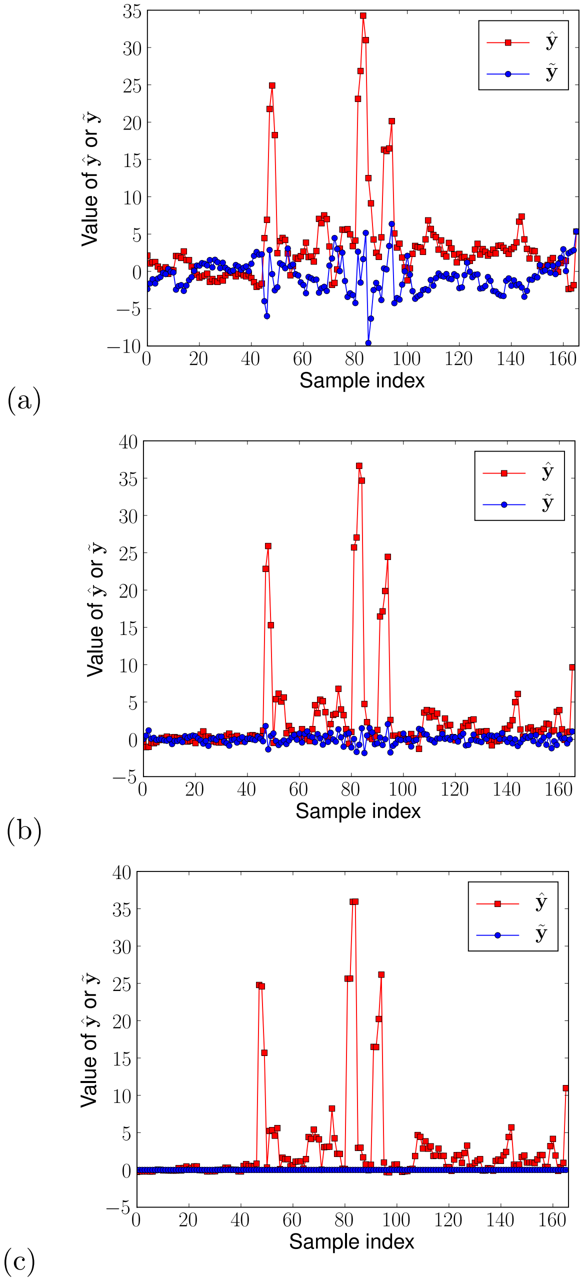

Figure 3.3: Effect of principal component number, k, on noise reduction (a) $k = 40$; (b) $k = 100$; (c) $k = L$. As k increases, more of the measurement on link $l = 588$ is attributed to noise, until at $k = L$, all of the measurement is considered to be noise.

Figure 3.4: Pictures of two experiments (a) Experiment 1 and (b) Experiment 2.

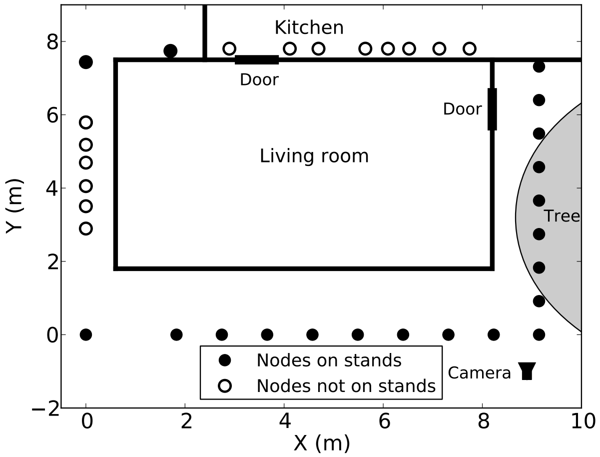

Figure 3.5: Experimental layout of Experiment 2. The shade area is covered by tree branches and leaves. All 34 nodes are outside the living room with four walls, seven nodes are in the kitchen, the other nodes are outside the house.

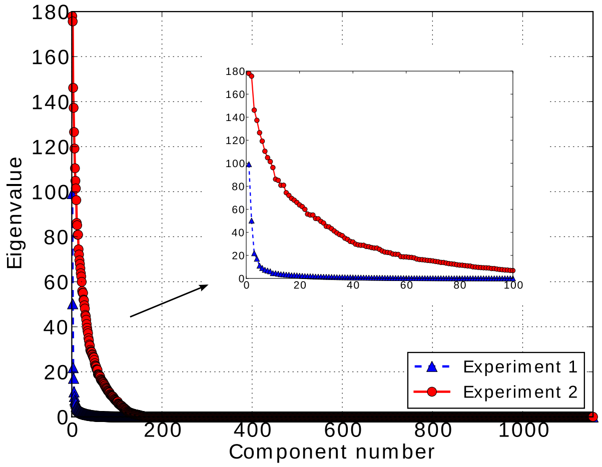

Figure 3.6: Scree plot.

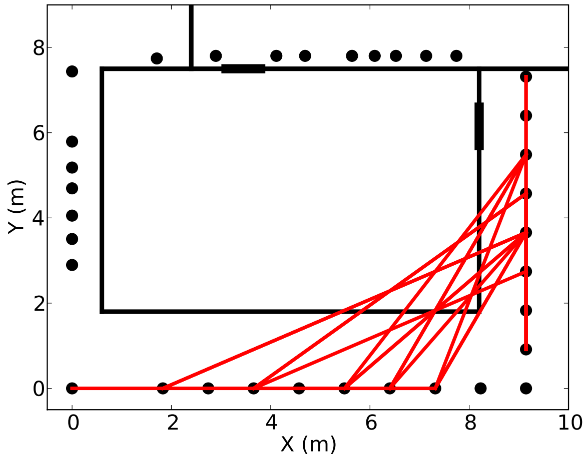

Figure 3.7: First eigen-network: Links with $u_{1l} > 30\%$ of $\max_l u_{1l}$.

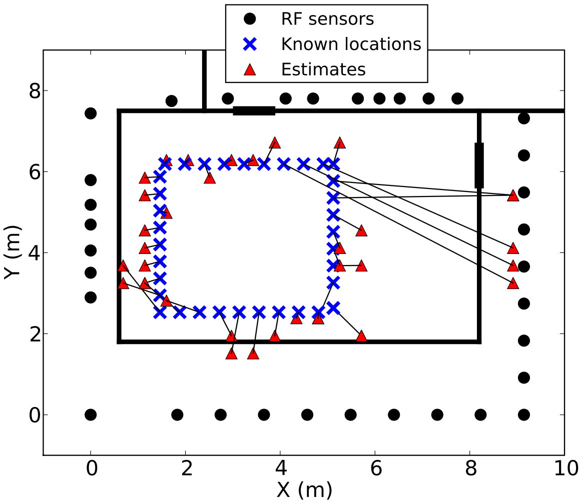

Figure 3.8: Estimates from VRTI using measurements recorded when a person walks the last round of the square path in Experiment 2.

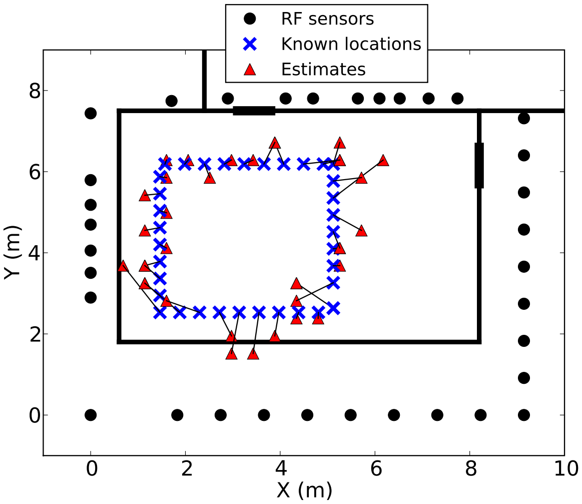

Figure 3.9: Estimates from SubVRT using the same measurements as used in Figure 3.8.

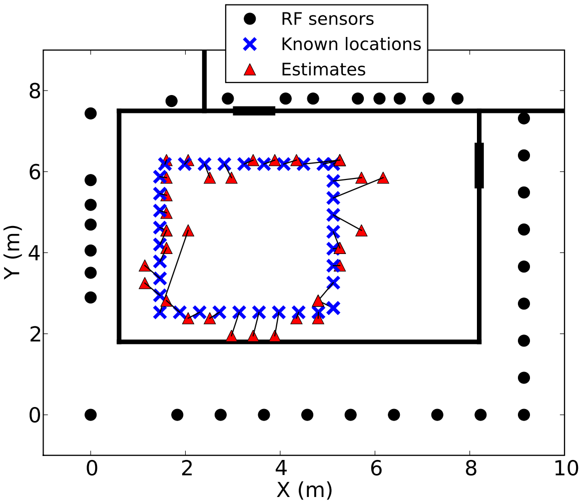

Figure 3.10: Estimates from LSVRT using the same measurements as used in Figure 3.8.

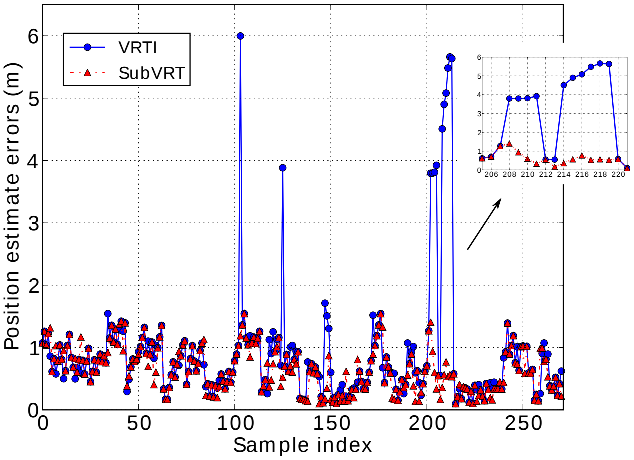

Figure 3.11: Estimate errors from VRTI and SubVRT.

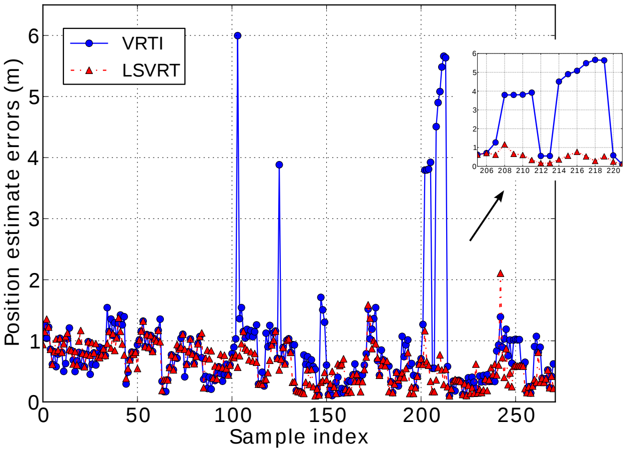

Figure 3.12: Estimate errors from VRTI and LSVRT.

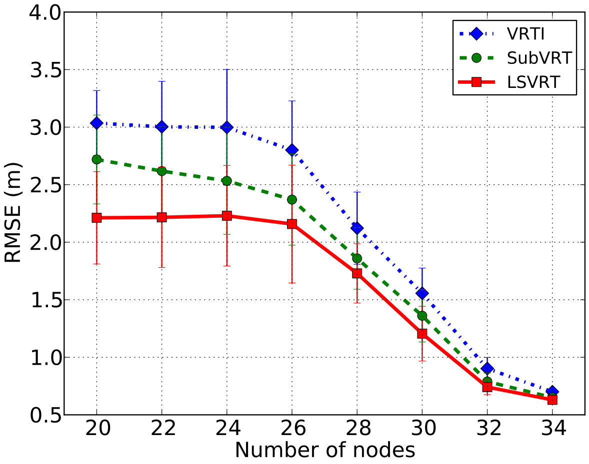

Figure 3.13: Localization RMSEs from Experiment 1 vs. numbers of nodes.

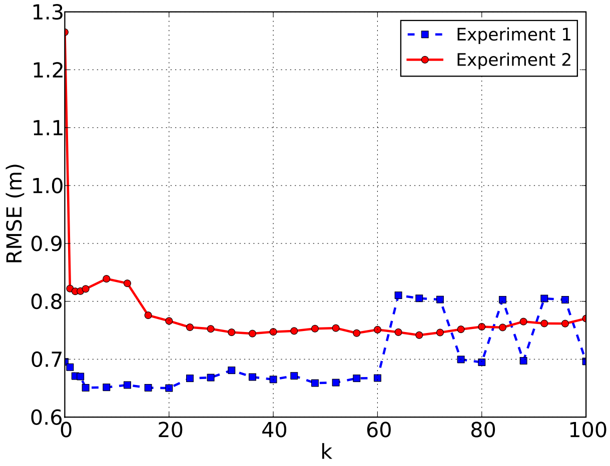

Figure 3.14: Localization RMSEs vs. principal component number k.

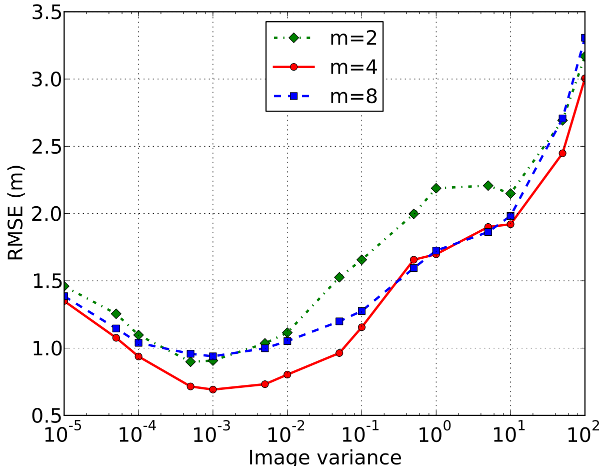

Figure 3.15: Localization RMSEs vs. σ_x^2.

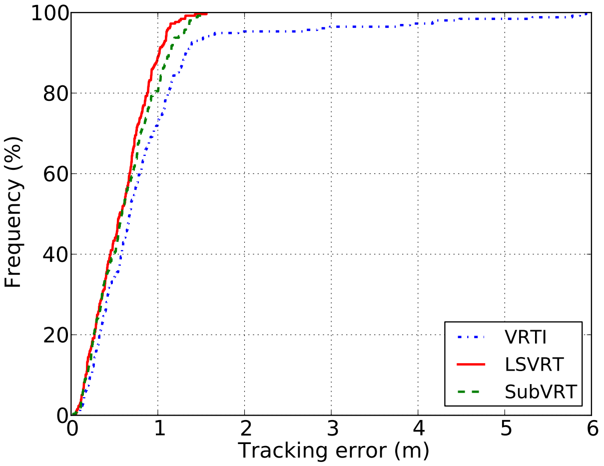

Figure 3.16: CDFs of tracking errors.

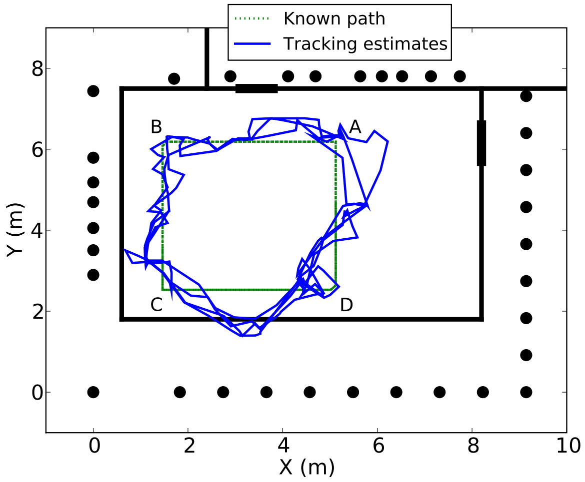

(a)

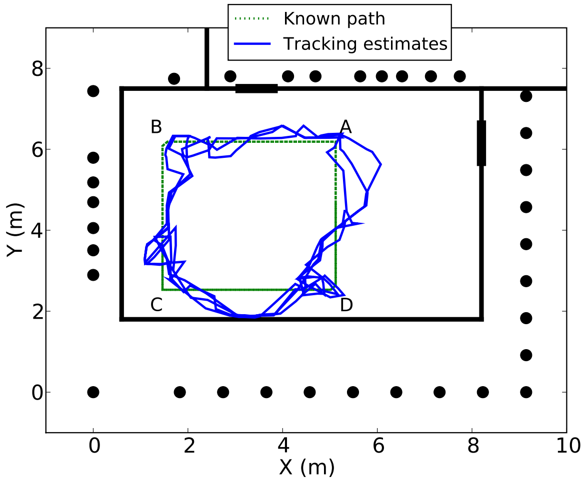

(b)

Figure 3.17: Kalman filter tracking results of Experiment 2 from SubVRT (a) and LSVRT (b).

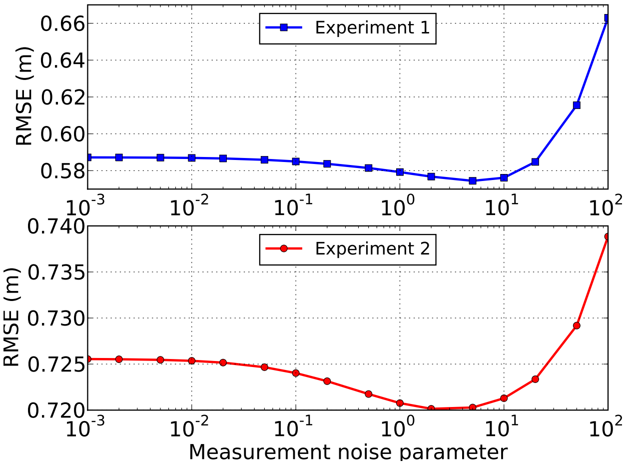

Figure 3.18: Tracking RMSE vs. measurement noise parameter σ_v^2.

Table 3.1: Localization RMSEs from VRTI, SubVRT and LSVRT.

Methods	VRTI	SubVRT		LSVRT	
Results	RMSE	RMSE	Improvement	RMSE	Improvement
Exp. 1	0.70	0.65	7.0%	0.63	9.6%
Exp. 2	1.26	0.74	41.3%	0.69	45.3%

Table 3.2: Parameters in VRTI, SubVRT, LSVRT and Kalman filter.

Parameter	Value	Description
α	100	Regularization parameter
m	4	Window length to calculate variance
k	$4, 36$	Numbers of principal components in Exp. 1, 2
σ_x^2	0.001	Variance of human motion
σ_w^2	2	Process noise parameter
σ_v^2	5	Measurement noise parameter

Table 3.3: Tracking RMSEs from VRTI, SubVRT and LSVRT.

Methods	VRTI	SubVRT		LSVRT	
Results	RMSE	RMSE	Improvement	RMSE	Improvement
Exp. 1	0.66	0.57	13.6%	0.57	13.6%
Exp. 2	1.21	0.72	40.5%	0.66	45.5%

CHAPTER 4

HISTOGRAM DIFFERENCE-BASED DEVICE-FREE LOCALIZATION

4.1 Abstract

Device-free localization systems pinpoint and track people in buildings using changes in the signal strength measurements made on wireless devices in the building's wireless network. It has been shown that such systems can locate people who do not participate in the system by wearing any radio device, even through walls, because of the changes that moving people cause to the static wireless network. However, many such systems cannot locate stationary people. We present and evaluate a system that can locate stationary or moving people, with or without calibration, by quantifying the difference between two histograms of signal strength measurements. From five experiments, we show that our kernel distance-based radio tomographic localization system performs better than the state-of-the-art device-free localization systems in different non-line-of-sight environments.

4.2 Introduction

Localization of people using wireless sensor networks has significant benefits in elder care, security, and smart facility applications [2, 4, 55]. Standard "radio localization" systems locate a transmitter tag, or allow a receiver to estimate its position [2, 8]. For these mentioned applications, it is critical to be able to locate all people, regardless of whether they carry a radio device. In this chapter, we explore "network RF environment sensing" (NRES), that is, using a static wireless network to create an image map of the people and objects and thus locate them in an area of interest based on the changes they cause in the radio frequency (RF) environment. An extensive review of reported NRES research can be found in [55]. NRES is also called "device-free localization" [16], "passive localization" [14], or "sensorless sensing" [17]. Unlike infrared or thermal, RF penetrates nonmetal walls, and thus NRES is useful for emergency applications. For example, in a hostage situation, police could deploy wireless devices outside of the building and learn in real time where people are located in the building, information that may save live.

An emerging NRES technique is to monitor the received signal strength (RSS) on links in a deployed static network and to use the changes in RSS to infer the location of the people in the deployment area [12, 13, 14, 15]. As opposed to multistatic ultra-wideband (UWB) radar [12] or MIMO radar [57], RSS-based NRES requires no specialized radar hardware, and thus can be implemented with standard wireless networks and devices. We focus on such RSS-based NRES systems in this chapter.

Although different NRES systems have been reported and tested, existing methods fail in particular situations. A common method is to use the change in mean in RSS on a link to indicate the shadowing from a person obstructing the link [76]. Shadowing-based radio tomographic imaging (RTI) uses links' changes in RSS mean values to estimate the shadowing loss field in the area of the wireless network [77, 22, 26, 24]. Shadowing-based RTI works well in line-of-sight (LOS) environments. In non-LOS areas, the assumption that RSS will decrease when a person is on the line between transmitter and receiver (the *link line*) fails. On a non-LOS link, the RSS may increase, decrease, or both, while a person is located on the link line [15], thus shadowing-based RTI fails in non-LOS environments.

Variance-based NRES methods use the variance of RSS measurements to locate human motion [18, 15]. These methods perform well even in non-LOS environments because a moving person changes the RSS of links as she crosses through them, increasing the RSS variance, even when the change in mean of RSS is close to zero. However, a stationary person does not change the RSS, thus variance-based methods cannot locate her.

One contribution of this work is to use *histogram difference* to quantify the change in RSS distribution caused by a person, rather than the change in mean or variance. Using histogram difference allows us to locate a person who is stationary or moving, and who is in a LOS environment or non-LOS environment. In short, mean and variance are just two aspects of a random variable; a good histogram difference quantifies the changes in mean, variance and other distribution features, in one metric. There are many histogram difference metrics available. In information theory, the Kullback-Leibler divergence (KLD), also known as relative entropy, is a nonsymmetric measure of the difference between two distributions. From its expression, we see that it is essentially the average of the logarithmic difference between two probability distributions. However, it is not symmetric, that is, the KLD from distribution p_1 to p_2 is generally not the same as that from p_2 to p_1. And also, when a distribution has zero-valued elements in the denominator, this metric suffers from the divide-by-zero problem. As another metric, the earth mover's distance (EMD) is a symmetric distance measure of histogram difference. Intuitively, if the two histograms are interpreted as two ways of moving a certain amount of earth, the EMD is the minimum work of changing from one way to the other. Thus, it involves solving a transportation optimization problem, and it requires high computation complexity. Finally, the kernel distance is another symmetric distance metric, which has many nice mathematical properties. The kernel distance is essentially an empirical estimate of a statistic called maximum mean discrepancy (MMD) defined in [78]. A conceptual explanation of MMD is that it is the least upper bound of the difference between two function means. The key aspect of the kernel distance is that it can be interpreted as an L_2 distance between two histograms or two sets of points embedded in a vector space, i.e., a Hilbert space. Thus, it is relatively easy to calculate without much computatoinal cost. In this chapter, we explore histogram difference metrics including the Kullback-Leibler divergence (KLD) [79] and the kernel distance [29].

Some fingerprint-based methods use histograms of RSS for purposes of NRES [19, 20]. During calibration, RSS histograms are recorded on all links in a network as a person stands in a known position, which becomes a fingerprint for a person being at that location. Fingerprints are recorded as the person is moved to each possible position in the environment (and the "empty-room" case, when no person is in the environment). During operation, the current RSS histogram is compared to all of the fingerprints, and the person is estimated to be at the position with the closest matching fingerprint [19, 20]. These methods require calibration at each possible person location (or each combination of persons' locations in the case of multiple people), which may be extensive. In contrast, shadowing-based RTI requires only a single empty-room calibration, and variance-based methods do not require any calibration.

In general, histogram difference-based NRES methods require a single empty-room calibration, similar to shadowing-based RTI methods. However, a second main contribution of this work, we show that for our proposed NRES system, an empty-room calibration can be replaced with a "long-term histogram" which is calculated during operation, regardless of the presence or absence of people. By enabling online calibration, we allow the NRES system to operate without any empty-room calibration, and thus be used for emergency applications in which operators do not know *a priori* whether an area is empty or not. We show that simple filtering of online RSS measurements using an IIR filter allows one to keep a long-term histogram in memory without significant computational complexity. This filtered long-term histogram is close enough to the histogram which would have been measured in an empty-room calibration to perform as well as with empty-room calibration. In fact, in situations in which the environment has changed since the empty-room calibration, the long-term histogram is *closer* to a true empty-room measurement, and NRES performs *better* with it than with the offline empty-room calibration. Compared to an FIR filter that requires more memory to store filter coefficients, the IIR filter used in this work only requires two coefficients. Besides, by using the iterative formulation of the IIR filter in the calculation of kernel distance, the computation complexity of kernel distance is reduced from $\mathcal{O}\left(N^2\right)$ to $\mathcal{O}\left(N\right)$ where N is the range of the RSS histogram.

In sum, the contribution of this chapter is to provide a complete framework for RSS-based environmental inference, including real-time calibration, that enables localization of both moving and stationary people in both LOS and non-LOS environments. We explore this framework using reported measurement sets and new measurement sets we collected for this purpose. We evaluate detection, imaging, and tracking using our framework.

The results show that some links' RSS measurements do not change while a person crosses the link line, so using any single link for NRES is unreliable. However, in an N-node wireless network, there is redundancy from the $\mathcal{O}\left(N^2\right)$ links in the network, and one can reliably locate people in the environment. We formulate a new NRES method that estimates a map of human presence from kernel distances in the network, which we call kernel distance-based radio tomographic imaging (KRTI). We then test tracking a single person in the area using a Kalman filter. Experimental results show that KRTI can locate moving people more accurately than VRTI [15] and SubVRT [23]. For localization of stationary people, KRTI also outperforms a sequential Monte Carlo method [16] both in localization accuracy and computational efficiency.

The rest of the chapter is organized as follows. Section 4.3 first introduces two types of RSS histograms and defines two histogram differences, then describes how we use these metrics to detect, map and track a person in the area of a wireless network. Section 4.4 describes experiments used in this chapter, and Section 4.5 shows the detection, localization and tracking results. We conclude in Section 4.6.

4.3 Methods

In this section, we first describe how we calculate short-term and long-term RSS histograms, and show human presence could increase the difference between these two histograms. Then we define two metrics to measure histogram difference, and we formulate detection, imaging, localization and tracking via histogram difference.

Commercial wireless devices return a discrete-valued RSS value with each received packet. We denote the RSS of the ith packet as y^i. We assume there is a finite set of possible RSS values, of size N. For example, if a device measures RSS in a range from y_{min} to y_{max} dBm and quantization is 1 dBm, then $N = y_{max} - y_{min} + 1$. Without loss of generality, we refer to the RSS integer as a number in the range $0, \ldots, N-1$.

We assume that there is a network with L links, and packets are transmitted repeatedly and regularly on each link, so that RSS measurements can be made.

4.3.1 Short-term and long-term histograms

In our proposed method, a link is characterized by a histogram $\mathbf{h}$ of its recent RSS measurements. The kth element of vector $\mathbf{h}$, that is, h_k, is the proportion of time that RSS integer k is measured on the link. At time n, we denote this histogram as $\mathbf{h}^n$, and calculate it as a filtered version, or weighted average, of RSS measurements:

$$\mathbf{h}^n = \sum_i w_{n,i} \mathbf{I}_{y^i} \tag{4.1}$$

where y^i is the RSS at time i, $\mathbf{I}$ is an N-length indicator vector, and $w_{n,i}$ is the weight for $\mathbf{I}_{y^i}$. The indicator vector $\mathbf{I}_{y^i}$ is one in element corresponding to the RSS integer y^i and zero in all other elements. Essentially, $\mathbf{I}_{y^i}$ is an instantaneous histogram based only on the current measurement, and $\mathbf{h}^n$ is a weighted average or filtered version of past instantaneous histograms.

We test two different weighting schemes to compute $\mathbf{h}^n$, an offline uniform window, or an exponentially weighted moving average (EWMA). The EWMA scheme has weights,

$$w_{n,i} = \begin{cases} \beta(1-\beta)^{n-i} & i \leq n \\ 0 & \text{otherwise} \end{cases}, \tag{4.2}$$

where $0 < \beta < 1$ is the forgetting factor. A higher β increases the importance of the most recent measurements in the histogram estimate. The EWMA is an infinite impulse response (IIR) filter, in which $\mathbf{h}^n$ is calculated as,

$$\mathbf{h}^n = (1-\beta)\mathbf{h}^{n-1} + \beta \mathbf{I}_{y^n}. \tag{4.3}$$

In this way, only the current RSS value y^n and previous histogram $\mathbf{h}^{n-1}$ are necessary to calculate the current histogram. Further, computation of (4.3) requires N multiplies and a single add. Thus we use the EWMA scheme for all histograms that are computed online, to minimize computational and memory complexity.

A histogram is *short-term* or *long-term* based on the chosen weights $w_{n,i}$. For the EWMA filter, the long-term histogram (LTH) would use a lower β, thus providing more weight to past measurements, than the short-term histogram (STH). In the next sections, we denote the LTH as $\mathbf{q}$ and the STH as $\mathbf{p}$.

The offline uniform window has weight $w_{n,i}$ given as,

$$w_{n,i} = \begin{cases} \frac{1}{T} & 0 \leq i \leq T \\ 0 & \text{otherwise} \end{cases}. \tag{4.4}$$

If we substitute (4.4) into (4.1), we see that the first T RSS values are given equal weight to calculate the histogram. As is clear from the fact that $w_{n,i}$ is not a function of current time n, the histogram computed from offline empty-room calibration does not change over time. We use (4.4) to implement the empty-room calibration, that is, we compute the long-term histogram $\mathbf{q}$ from (4.4) when we want to test how our system would have performed if calibrated using data from an initial test period (from 0 to T) when no person was in the area. The offline uniform window is used purely to compare results when using the proposed online LTH vs. the offline empty-room LTH.

Examples shown in Figure 4.1 show how the STH and LTH differ for two example links. The empty-room LTH, computed from $T = 141$ and the offline uniform window, shows a consistent value of -64 dBm on the link in Figure 4.1(a). Two online STHs are shown, both computed with $\beta = 0.9$, when a person is present on the link line and when no person is on the link line. With no person present, the STH is nearly identical to the empty-room LTH. When a person stands still on the link line, the STH shows a consistent RSS of -68 dBm. In Figure 4.1(b), a similar effect is seen — the STH with no person on the link line is nearly the same as the empty-room LTH. Note also the "STH with person" in this figure is from a time when the person is moving across (rather than standing still on) the link line, and two different RSS values are present in the STH.

Finally, note that Figure 4.1(b) shows the similarity between the online (EWMA-based) LTH and the offline empty-room LTH. The online LTH, computed from EWMA with a forgetting factor $\beta = 0.05$ does show some nonzero probabilities of other RSS values (e.g., -41, -43, -45, $\ldots$), however, the probabilities of these values are very close to zero. It is the fact that these LTHs are very similar which allows us to replace the empty-room calibration, which requires knowing that no person is in the area for a period of time, with an LTH calculated online while people are present and moving in the area.

Next, we formalize our discussion of the differences between histograms by defining two histogram difference metrics.

4.3.2 Histogram difference

There are many ways to measure the difference $D(\mathbf{p}, \mathbf{q})$ between two histograms $\mathbf{p}$ and $\mathbf{q}$. The earth mover distance is a popular way of comparing two histograms. However, it involves solving an optimal transportation problem and thus is too computationally expensive for a real-time NRES system. Here, we choose another well known metric, the Kullback-Leibler divergence (KLD) [79]. We also propose to use the kernel distance, which has been recently applied in computational geometry [80].

4.3.2.1 Definitions

The Kullback-Leibler divergence between two histograms $\mathbf{p}$ and $\mathbf{q}$ can be calculated as [79]:

$$D_{KL}(\mathbf{p}, \mathbf{q}) = \sum_k p_k \log \frac{p_k}{\tilde{q}_k}, \tag{4.5}$$

where $\tilde{q}_k = \frac{\max(\epsilon, q_k)}{\sum_k \max(\epsilon, q_k)}$, and ϵ is a small number that we use to avoid any divide-by-zero. Note that we investigate the effect of ϵ later in Section 4.5.4.

The kernel distance between $\mathbf{p}$ and $\mathbf{q}$ is calculated as [29]:

$$D_K(\mathbf{p}, \mathbf{q}) = \mathbf{p}^T \mathbf{K} \mathbf{p} + \mathbf{q}^T \mathbf{K} \mathbf{q} - 2\mathbf{p}^T \mathbf{K} \mathbf{q}, \tag{4.6}$$

where $\mathbf{K}$ is an N by N kernel matrix from a 2-D kernel function, and $()^T$ indicates transpose. There are two commonly used kernel functions. One commonly used kernel is the Gaussian kernel, defined as:

$$\mathbf{K}(y_j, y_k) = \exp\left(-\frac{|y_j - y_k|^2}{\sigma_G^2}\right), \tag{4.7}$$

where y_j and y_k are the jth and kth elements, and σ_G^2 is the kernel width parameter. Another common kernel is the Epanechnikov kernel, which is optimal in the sense that it minimizes asymptotic mean integrated squared error [81],

$$\mathbf{K}(y_j, y_k) = \frac{3}{4}\left(1 - \frac{|y_j - y_k|^2}{\sigma_E^2}\right) I_{|y_j - y_k| \leq \sigma_E}, \tag{4.8}$$

where I_a is the indicator function, $I_a = 1$ where a is true and zero otherwise, and σ_E^2 is the kernel width parameter. We investigate both kernel functions, and they achieve similar performance.

4.3.2.2 Efficient implementation

The computation of (4.6) has $\mathcal{O}\left(N^2\right)$ multiplication and add operations. We show in the following that the kernel distance can be calculated with only $\mathcal{O}\left(N\right)$ operations. First, we use the fact that $\mathbf{K}^{\frac{1}{2}}$ is a symmetric matrix $\mathbf{K}^{\frac{1}{2}} = (\mathbf{K}^{\frac{1}{2}})^T$ to change formulation (4.6) to the standard Euclidean distance:

$$\begin{aligned} D_K(\mathbf{p},\mathbf{q}) &= (\mathbf{K}^{\frac{1}{2}}\mathbf{p})^T\mathbf{K}^{\frac{1}{2}}\mathbf{p} + (\mathbf{K}^{\frac{1}{2}}\mathbf{q})^T\mathbf{K}^{\frac{1}{2}}\mathbf{q} - 2(\mathbf{K}^{\frac{1}{2}}\mathbf{p})^T\mathbf{K}^{\frac{1}{2}}\mathbf{q} \\ &= \|\mathbf{K}^{\frac{1}{2}}\mathbf{p} - \mathbf{K}^{\frac{1}{2}}\mathbf{q}\|^2, \end{aligned} \tag{4.9}$$

where $\|\cdot\|$ indicates the Euclidean distance. Letting $\mathbf{u} = K^{\frac{1}{2}}\mathbf{p}$, $\mathbf{v} = K^{\frac{1}{2}}\mathbf{q}$, we obtain,

$$D_K(\mathbf{p},\mathbf{q}) = \|\mathbf{u} - \mathbf{v}\|. \tag{4.10}$$

Now, consider the online computation of the kernel distance at time n, that is, $D_K(\mathbf{p}^n, \mathbf{q}^n)$, where both LTH and STH are calculated using the EWMA method in (4.3). Instead of updating $\mathbf{p}^n$ and $\mathbf{q}^n$ each time n, we can reduce computational complexity by instead updating $\mathbf{u}^n$ and $\mathbf{v}^n$, that is, $\mathbf{u}$ and $\mathbf{v}$ at time $n > 0$, using the same EWMA method:

$$\begin{aligned} \mathbf{u}^n &= (1-\beta_p)\mathbf{u}^{n-1} + \beta_p\mathbf{K}^{\frac{1}{2}}\mathbf{I}_{y^n} \\ \mathbf{v}^n &= (1-\beta_q)\mathbf{v}^{n-1} + \beta_q\mathbf{K}^{\frac{1}{2}}\mathbf{I}_{y^n}, \end{aligned} \tag{4.11}$$

where y^n is the RSS at time n, β_p is the forgetting factor for $\mathbf{u}$, and β_q is the factor for $\mathbf{v}$. The term $\mathbf{K}^{\frac{1}{2}}\mathbf{I}_{y^n}$ is simply the kth column of matrix $\mathbf{K}^{\frac{1}{2}}$, where k is the index of the RSS y^n in the histogram, and thus does not require any multiplications. Thus (4.11) requires $\mathcal{O}\left(N\right)$ multiplies and adds.

Note that initial values $\mathbf{v}_0$ and $\mathbf{u}_0$ must be given. We assume that the system has been running prior to $n = 0$ and use the LTH histogram of these initial measurements to initialize $\mathbf{v}_0$ and $\mathbf{u}_0$. The current kernel distance at time n is calculated as,

$$D_K(\mathbf{u}^n, \mathbf{v}^n) = \|\mathbf{u}^n - \mathbf{v}^n\|. \tag{4.12}$$

This formula for d^n is identical to $D_K(\mathbf{p}^n, \mathbf{q}^n)$ except that it requires $\mathcal{O}\left(N\right)$, rather than $\mathcal{O}\left(N^2\right)$, multiplies and adds.

4.3.2.3 Examples

Consider the example histograms in Figure 4.1. For Figure 4.1(a), $D_K(\mathbf{p},\mathbf{q}) = 0.83$ between the LTH and the STH with a person on the link line, if we use the Epanechnikov kernel with $\sigma_E^2 = 30$. Without any people on the link line, $D_K(\mathbf{p}^n, \mathbf{q}^n) = 0$, since the STH is the same as the LTH. For the moving people case in Figure 4.1(b), $D_K(\mathbf{p}^n, \mathbf{q}^n) = 1.2$ between the LTH and the STH with people, while $D_K(\mathbf{p}^n, \mathbf{q}^n) = 0.2$ if no people near the link. These two examples show that the presence of a stationary and moving person significantly increases the kernel distance.

As another example, we show in Figure 4.2 both the RSS, y^n, and kernel distance, $D_K(\mathbf{p}^n, \mathbf{q}^n)$, for a period of time in which a person crosses the link twice. Kernel distance is very close to zero except when the person crosses the link at $n = 23$ and $n = 120$, when it exceeds 1.0. Note that $0 \leq D_K(\mathbf{p}^n, \mathbf{q}^n) \leq 2$. The kernel distance indicates clearly the link crossings by its high value.

4.3.3 Detection of a person on link line

In this section, we quantify the ability of RSS histogram difference to detect a person on a link line. As we find out, not all links are able to detect line crossings.

First, we define what we mean by a person being on a link line. We denote the transmitting node and receiving node of link l as i_l and j_l, with coordinates $\mathbf{s}_{i_l}$ and $\mathbf{s}_{j_l}$, respectively. We denote the person's true location as $\mathbf{z}$. Our definition of "person on the link line" (POLL) is that the person's center coordinate $\mathbf{z}$ is in an ellipse of excess path length $\lambda > 0$ with foci at the node locations, that is,

$$\text{POLL} : \|\mathbf{s}_{i_l} - \mathbf{z}\| + \|\mathbf{s}_{j_l} - \mathbf{z}\| < \|\mathbf{s}_{i_l} - \mathbf{s}_{j_l}\| + \lambda. \tag{4.13}$$

Note that we use $\lambda = 0.06m$ in our results, so that the elliptical area includes only positions very close to the line between the two nodes.

We want to decide between two hypotheses, H_0 that the NPOLL condition is true, and H_1 that POLL is true. To avoid making assumptions about the distribution of histogram differences given H_0 or H_1, we simply suggest that histogram differences will be higher under H_1 than under H_0. Thus, we decide whether we believe NPOLL or POLL is true by comparing the histogram difference to a threshold:

$$D(\mathbf{p}_l, \mathbf{q}_l) \underset{H_0}{\overset{H_1}{\gtrless}} \eta, \tag{4.14}$$

where η is a user-defined detection threshold, $\mathbf{p}_l$ and $\mathbf{q}_l$ are the STH and LTH from link l, respectively, and $D(\mathbf{p}_l, \mathbf{q}_l)$ is calculated from either KLD or kernel distance. Detection results are shown in Section 4.5.1.

4.3.4 Histogram difference radio tomography

Let $\mathbf{d} = [d_0, \ldots, d_{L-1}]^T$ denote a histogram difference vector with L directional link histogram distances, $d_l = D(\mathbf{p}_l, \mathbf{q}_l)$. Let $\mathbf{x} = [x_0, \ldots, x_{M-1}]^T$ denote an image vector, where x_m is a measure of the current presence of a person or object in pixel m that was not typically present in the past. In other words, x_m is the "novelty" of human presence in pixel m. We assume that $\mathbf{d}$ can be expressed as a linear combination of $\mathbf{x}$, as has been assumed for other RTI systems [76, 77, 22, 26, 24, 15]:

$$\mathbf{d} = \mathbf{W}\mathbf{x} + \mathbf{n}, \tag{4.15}$$

where $\mathbf{n}$ is a vector of measurement noise and model error. We use the elliptical weight model $\mathbf{W}$ given in [22, 15], in which the weight $W_{l,m}$ for pixel m is nonzero only if the pixel center is in an ellipse with foci at the link transmitter and receiver locations.

A radio tomographic image $\hat{\mathbf{x}}$ be estimated from histogram difference measurements $\mathbf{d}$ using:

$$\hat{\mathbf{x}} = (W^T C_{\mathbf{n}}^{-1} W + C_{\mathbf{x}}^{-1})^{-1} W^T C_{\mathbf{n}}^{-1} \mathbf{d}, \tag{4.16}$$

where $C_{\mathbf{x}}$ is the covariance matrix of $\mathbf{x}$, and $C_{\mathbf{n}}$ is the covariance matrix of the link measurement noise. Here we use a least squares formulation, which has been shown to outperform the Tikhonov regularization method [27]. The covariance matrix of the link measurement noise, $C_{\mathbf{n}}$, is not generally known here, thus we assume the noise vector has i.i.d. elements. Thus $C_{\mathbf{n}}$ becomes an identity matrix multiplied by σ_n^2. We propose to use the following modified least squares formulation:

$$\hat{\mathbf{x}} = \Pi_K \mathbf{d} \quad \text{where } \Pi_K = (W^T W + \sigma_n^2 C_{\mathbf{x}}^{-1})^{-1} W^T. \tag{4.17}$$

We model the scaled image covariance the same as in [27], where the (i, j) element of $\sigma_n^2 C_{\mathbf{x}}$ is given by

$$\left[\frac{1}{\sigma_n^2} C_{\mathbf{x}}\right]_{i,j} = \frac{\sigma^2}{\delta} \exp\left(-\frac{\|\mathbf{r}_j - \mathbf{r}_i\|}{\delta}\right), \tag{4.18}$$

where $\sigma^2 = \sigma_x^2/\sigma_n^2$ is the ratio of variance of human presence σ_x^2 to the variance of noise σ_n^2, which we use as a regularization parameter, δ is a correlation distance parameter, $\mathbf{r}_i$ and $\mathbf{r}_j$ are the center coordinates of the ith and jth pixels, and $\|\cdot\|$ indicates Euclidian distance. From (4.17) we see the image estimate is the product of $\mathbf{d}$ with a projection matrix Π_K which can be calculated ahead of time. This product can be calculated in real-time.

In Section 4.5.4, we compare the performance of KLD and kernel distance for calculation of $\mathbf{d}$ in (4.17), and show that the kernel distance consistently outperforms the KLD. Thus we generally call our method *kernel distance-based radio tomographic imaging*, or KRTI.

4.3.5 Localization and tracking

In this section, we describe how to use the image in (4.17) to perform localization and tracking, which is the focus of this chapter. We assume, for localization and tracking purposes, that only one person is present in the network area. When multiple people are in the area, they can be seen in the KRTI image, however, multitarget tracking from the image estimate is a very difficult problem and is not the focus of this chapter. We assume that if our contributions improve tracking performance with one person in the network, then future multitarget tracking methods will also benefit.

From the KRTI image estimate $\hat{\mathbf{x}}$, the position of the person is estimated as the center coordinate of the pixel with maximum value. That is,

$$\hat{\mathbf{z}} = \mathbf{r}_q \quad \text{where} \quad q = \arg\max_p \hat{x}_p$$

where $\hat{x}_p$ is the pth element of vector $\hat{\mathbf{x}}$ from (4.17). The localization error of this estimate is defined as: $e_{loc} = \|\hat{\mathbf{z}} - \mathbf{z}\|$, where $\mathbf{z}$ is the actual position of the person.

To increase accuracy when locating moving people, we apply a Kalman filter to the localization estimates to track people's locations over time. In the state transition model of the Kalman filter, we include both mobile people's location and velocity in the state vector, and the observation inputs of the Kalman filter are the localization estimates. We use the same Kalman filter implementation as in [23].

We evaluate both localization and tracking performance in Section 4.5.

4.4 Experiments

In this section, we describe experiments that we use in evaluating our new framework. In our experiments, we use TelosB nodes and we program nodes with a token passing protocol [7] so that at any particular time, only one node is broadcasting while all the other nodes are measuring pairwise RSS. All nodes are operating on the 26th channel of IEEE 802.15.4. A basestation connected to a laptop listens to the broadcast on that channel and collects RSS measurements from these nodes.

Experiments 1 and 2 are performed on a calm day by Wilson et al. [15]. 34 radio nodes are deployed outside the living room of a residential house with a deployment area of about 9 m by 8 m [15]. During the first experiment (Experiment 1), they ask a person to stand motionless at 20 different known locations inside the living room. Experiment 2 is performed on the same day with the same settings, but the task is to locate a person walking inside the living room. A person walks around a marked path at a constant speed using a metronome so that the location of the person at any particular time is known. An important fact about Experiment 2 is after recording offline calibration measurements, a node (node ID 32) on the PVC stand was moved to a different location. This system change affects the system performance, which we discuss later.

The third and fourth experiments (Experiment 3 and Experiment 4) are new datasets, performed on a windy day at the same location as before. Since a recent study [23] demonstrated the degrading effect of wind-induced motion on a variance-based localization system, we choose a windy day and we also place three rotating fans at three locations in the living room to create more motion to increase the background noise. Experiments 3 and 4 are performed in the same condition, and both are used to locate a person walking inside the house. The difference is that we observe significant environmental difference between the offline calibration period and the online localization period in Experiment 4. During offline calibration period, wind blows strongly causing a lot of RSS variations, but it becomes much weaker during online period. We investigate the effect of system and environment changes on the system performance in Section 4.5.5.

The last experiment (Experiment 5) is performed by Wilson et al. [16] in the University of Utah bookstore in an area of about 12 m by 5 m with 34 nodes deployed on book shelves and display tables. In this experiment, a person walks clockwise around a known path twice from Point A to Point D as shown in the experimental layout Figure 4.3(a). The bookstore environment is cluttered with shelves, tables and books, as shown in Figure 4.3(b).

In sum, the first four experiments are performed at the same environment and are all ”through-wall” experiments with nodes deployed outside walls. All five experimental environments should be multipath-rich environments.

4.5 Results

In this section, we first evaluate detection via histogram difference, then we show imaging and localization results of a stationary person. After that, we show localization and tracking results of a moving person. Finally, we discuss the performance of using KLD and kernel distance, we also discuss the effect of environment and system change on KRTI performance.

4.5.1 Detection results

We first quantify the ability of histogram difference to distinguish whether a person is on the link line (POLL) or not (NPOLL). We use the EWMA scheme to calculate both long-term histogram $\mathbf{q}$ and short-term histogram $\mathbf{p}$. We use data from Experiment 1 and parameters as given in Table 4.2.

First, we record all kernel distances during H_0 (NPOLL). The distribution of $D_K(\mathbf{p}^n, \mathbf{q}^n)$ given H_0 is shown in Figure 4.4(a). Approximately half of kernel distances are zero, and the vasty majority are below 0.5. For the data recorded on links where H_1 (POLL) is true, the kernel distance distribution is shown in Figure 4.4(b). Now, fewer kernel distances are zero, down to 20%; however, this means that we have no chance of detecting the person standing on the link line for 20% of links.

From the distributions of $D_K(\mathbf{p}^n, \mathbf{q}^n)$ given H_0 and H_1, we calculate the receiver operating characteristic (ROC) curve in Figure 4.4(c). Even for a probability of false alarm (P_{FA}) of 40%, the probability of detection is below 80%. Similarly, we test the use of KLD as the difference metric, with the resulting ROC curve shown in Figure 4.4(c). For low P_{FA}, kernel distance has higher detection performance, while for high P_{FA}, KLD performs better.

The results show the difficulties in detecting human presence using only one link's RSS data. This motivates the use of a network of many links, rather than just a single linke, in order to infer the presence and location of people in an area.

4.5.2 Imaging and localization of a stationary person

In this section, we demonstrate that KRTI can not only locate moving people, but also stationary people, a major advantage of KRTI over variance-based methods [15, 18]. We use measurements from Experiment 1, in which a person stands motionless inside a house, and compare imaging results from KRTI and VRTI [15]. In Figure 4.5(a), the KRTI image has relatively high pixel values near the true location of the person, and the pixel with maximum value is very close to the true location. Since a stationary human body does not cause much RSS variance, VRTI cannot correctly image the person's location, as shown in Figure 4.5(b). Note that we use the EWMA scheme for both long-term and short-term histograms, and the kernel distance, with parameters listed in Table 4.2.

A recent method able to locate a stationary person in a multipath-rich environment is the sequential Monte Carlo (SMC) approach developed by [16]. The method of [16] requires an empty-room (offline) calibration, and is substantially more computational complex than the KRTI method. Further, across experiments, we show that KRTI is more accurate in localization. We run SMC using three hundred particles using data from Experiment 1. In Experiment 1, a person sequentially stands at each of 20 known locations for a constant period τ. At each location we have about 50 KRTI estimates. For these twenty locations, we calculate the overall average error $\bar{e}_{loc} = \sum_{i=1}^{20} \|\hat{\mathbf{z}}_a - \mathbf{z}\|$, where $\hat{\mathbf{z}}_a$ is the average location estimates from KRTI and SMC during period τ. The average location estimates $\hat{\mathbf{z}}_a$ from

KRTI are shown in Figure 4.6, in which the line between the average estimate (shown as triangle) and the true location (shown as cross) indicates the estimation error. We see the errors from KRTI are generally below 1 m, more accurate than the results from SMC shown in Figure 10 of [16]. The average error $\bar{e}_{loc}$ from SMC is 0.83 m, while $\bar{e}_{loc}$ from KRTI is 0.71 m, a 14.5% reduction. On the same 2.4 GHz Core 2 Duo processor-based laptop, it takes 0.03 seconds to produce one estimate from our KRTI Python code, while it takes three to four minutes to produce one SMC location estimate. Thus, KRTI outperforms SMC both in accuracy and computational efficiency.

4.5.3 Localization and tracking of a moving person

Besides the improvement on imaging and locating stationary people, KRTI also provides better performance for locating moving people. Now we compare KRTI with two variance-based methods, VRTI [15] and SubVRT [23]. We run KRTI, VRTI and SubVRT on data from Experiments 2 - 5, and calculate the root mean squared error (RMSE), which is defined as the square root of the average squared localization error. As shown in Table 4.3, our KRTI can achieve submeter localization accuracy in all experiments. Particularly, for Experiment 3, performed on a windy day, the RMSE from VRTI is 2.1 m, while the RMSE from KRTI is 0.69 m, a 67% improvement. For Experiment 2, performed on a calm day, SubVRT has a better performance than KRTI (0.65 m vs. 0.78 m RMSE for KRTI). Since SubVRT uses offline empty-room calibration measurements to estimate the noise covariance [23], we expect it to perform particularly well during windy conditions. KRTI does not use such empty-area calibration. However, KRTI significantly outperforms SubVRT, by 30-35%, in all other experiments. Particularly, in Experiment 4, in which the environment changes between the offline calibration and the online measurements, SubVRT does not perform well. However, KRTI uses online measurements to build the long-term histogram, thus is not significantly affected by offline measurements. The RMSE of KRTI is 0.76 m in this case, a 33% improvement on SubVRT. We discuss the effect of environmental changes in more detail in Section 4.5.5. For Experiment 5, due to the strong multipath environment of the cluttered bookstore (as shown in Figure 4.3(b)), neither VRTI nor SubVRT perform very well. However, KRTI is particularly robust to non-LOS environments and achieves 0.73 m RMSE, a similar error as in other experiments. To summarize, KRTI does not just use RSS variance or RSS mean. Instead, it uses histogram difference to include both the effect of a stationary person and a moving person. It is particularly robust to the multipath environment, working just as well in strong multipath environments.

Finally, we show the Kalman filter tracking results of Experiment 5 in Figure 4.7. We see that tracking results have highest errors when the person is far from the closest radio node. For example, the tracking error is about 1 m when the person is located at the upper left corner of the path. However, KRTI with a Kalman filter is capable of tracking a person in a large multipath-rich environment with submeter accuracy in general. We also compare the cumulative distribution functions (CDFs) of tracking errors from KRTI and VRTI in Figure 4.8. For VRTI, 95% of tracking errors are below 1.7 m, while 95% of errors from KRTI are below 1.2 m, a 29% improvement. We also see the median tracking RMSE from VRTI is 1.0 m, while it is 0.6 m for KRTI, a 40% improvement.

4.5.4 Kernel distance vs. KLD

In this section we compare kernel distance and Kullback-Leibler divergence (KLD) as histogram difference metrics in localization. Using an Epanechnikv kernel defined in (4.8), we test different kernel width parameters σ_E^2. Figure 4.9 shows that KRTI performance is not sensitive to this parameter. RMSEs from Experiments 2 and 3 are both shallow functions of σ_E^2, as long as $\sigma_E^2 \geq 10$. A wider kernel makes the distance more robust to measurement noise, whereas a narrower kernel makes it more sensitive to the noise because it does not smooth the nearby measurements as much to act similarly with respect to the distance.

To calculate KLD, we use parameter ϵ in (4.5) to avoid division by zero. As shown in Figure 4.10, if $\epsilon < 0.1$, the localziation RMSE is only mildly sensitive to this parameter. However, from a comparison of Experiments 2 and 3, the RMSEs when using KLD are generally above 0.8 m, while most RMSEs from kernel distance are below 0.8 m. From Figure 4.9 and Figure 4.10, we see both histogram difference metrics can achieve submeter localization accuracy, however, kernel distance is less sensitive to its parameter σ_E^2, and consistently outperforms KLD in localization accuracy.

4.5.5 Effects of environment and system changes

In the above tests, we use the EWMA filter to calculate the online LTH $\mathbf{q}$. We can also use the offline empty-room calibration in order to calculate the LTH. We compare the two in this section.

Note that if the environment changes or sensors change positions after the offline empty-room calibration, the changes diminish system performance. As described in Section 4.4, the location of a single node is accidentally changed after the offline empty-room calibration period in Experiment 2, prior to the online period. Even if a receiver node moves by only a fraction of its wavelength, its measured RSS values may vary by tens of dB as a result of small-scale fading [61]. We apply the offline empty-room LTH in KRTI to generate the image in Figure 4.12, in which a person is walking and is at the position indicated by the cross. The figure shows two hot spot areas – besides the one close to the true location of the person, there is another one at the lower left corner of the network, close to node 32 indicated by the red circle. A similar false image, not shown, is seen during Experiment 4, in which the environment changes after the offline empty-room calibration. We avoid this false image problem by using the EWMA for online calculation of the LTH.

In our KRTI method, we use solely the EWMA filter for online calculation of both long-term and short-term histograms. We do, however, require initialization of the histograms at time zero. In real-time operation, we would simply run the system for a short period to allow the LTH to "settle" prior to using its results. For experiments, we do not have a settling period, and instead, we initialize the LTH with the (uniform windowed) average over the empty-room measurements, that is, the offline LTH. Our online LTH then quickly "settles" to the LTH of the online measurements.

We see the relative RMSE performance of empty-room LTH (offline FIR) vs. online LTH (online EWMA) in Table 4.4. We see that the online LTH is as good or better than the offline LTH in every case. While the RMSEs are similar in Experiments 3 and 5, the online LTH performs significantly better for Experiments 2 and 4, for which there were either sensor position changes or environmental changes between the empty-room calibration and the online operation, as described earlier. Since the offline empty-room measurements are used to initialize the online LTH, the effect of corrupted link measurements is present at the very beginning of the online period in Experiment 4. However, after updating the LTH for a while, KRTI image can clearly show the location of the person, since more online measurements replace offline calibration measurements. If we control the updating speed appropriately by choosing $\beta_q = 0.05$, the "online EWMA" method can achieve submeter accuracy for all experiments. Since Experiments 3 and 5 do not have much environment and system change effect, both methods have similar performance.

For KRTI using the online LTH, we test the effect of EWMA forgetting factor β_q. The RMSEs from KRTI with different β_q values are shown in Figure 4.11. The RMSEs are very shallow functions of β_q and are all below 1 m in the range of 0.01 to 0.1. If β_q is below 0.01, the weight of the latest measurement becomes very small, that is, the update process of the LTH is very slow. If $\beta_q = 0$, it is equivalent to no update. At the other extreme, if β_q is too high, i.e., above 0.1, then the update speed becomes too fast. If β_q approaches 1, then almost all previous RSS measurements are removed from the memory. To keep sufficient history measurements in memory and also balance between these two extremes, we choose $\beta_q = 0.05$ as listed in Table 4.2. We also test the effect of EWMA factor β_p for updating the STH $\mathbf{p}$, we find KRTI performance is best in the range of 0.8 to 1.

4.5.6 Discussion

Results from five different experiments show that our KRTI method has new features that other methods do not. Moreover, KRTI demonstrates better performance in imaging, localization and tracking. Compared with variance-based methods [15, 23], KRTI has the ability of imaging a stationary person as well as a moving person. For tracking a moving person, KRTI also outperforms VRTI and SubVRT. In addition, KRTI can use an EWMA filter to update the long-term histogram continuously during an online period, and is more robust to environmental and system changes. The advantage of KRTI over SMC [16] is that KRTI does not require any empty-area offline calibration, and performs better both in localization accuracy and computational efficiency. We know that shadowing-based radio tomographic imaging (RTI) can locate both stationary and moving people at line-of-sight (LOS) environments, but does not work at multipath-rich environments. To our knowledge, KRTI is the first method that can locate both stationary and moving people in both LOS and non-LOS environments without any offline calibration.

To summarize, KRTI has new properties that other methods do not. We list features of different methods in Table 4.5.

4.6 Conclusion

In this chapter, we propose a new network RF environment sensing (NRES) framework that uses histogram difference and online calibration to perform network RF sensing of people. Specifically, we propose a kernel distance-based RTI (KRTI), which uses the histogram distance between a short-term histogram and a long-term histogram to image and locate a moving or stationary person. We explore the framework using three reported measurement sets and two new measurement sets. We evaluate detection, imaging and tracking using our framework. Our experimental results show that KRTI provides robust imaging and tracking capabilities at multipath-rich environments, even though detection from individual links is unreliable. Compared with previous NRES methods, our KRTI is the only real-time method that is capable of imaging and locating both stationary and moving people in both LOS and non-LOS environments without any empty-room offline calibration.

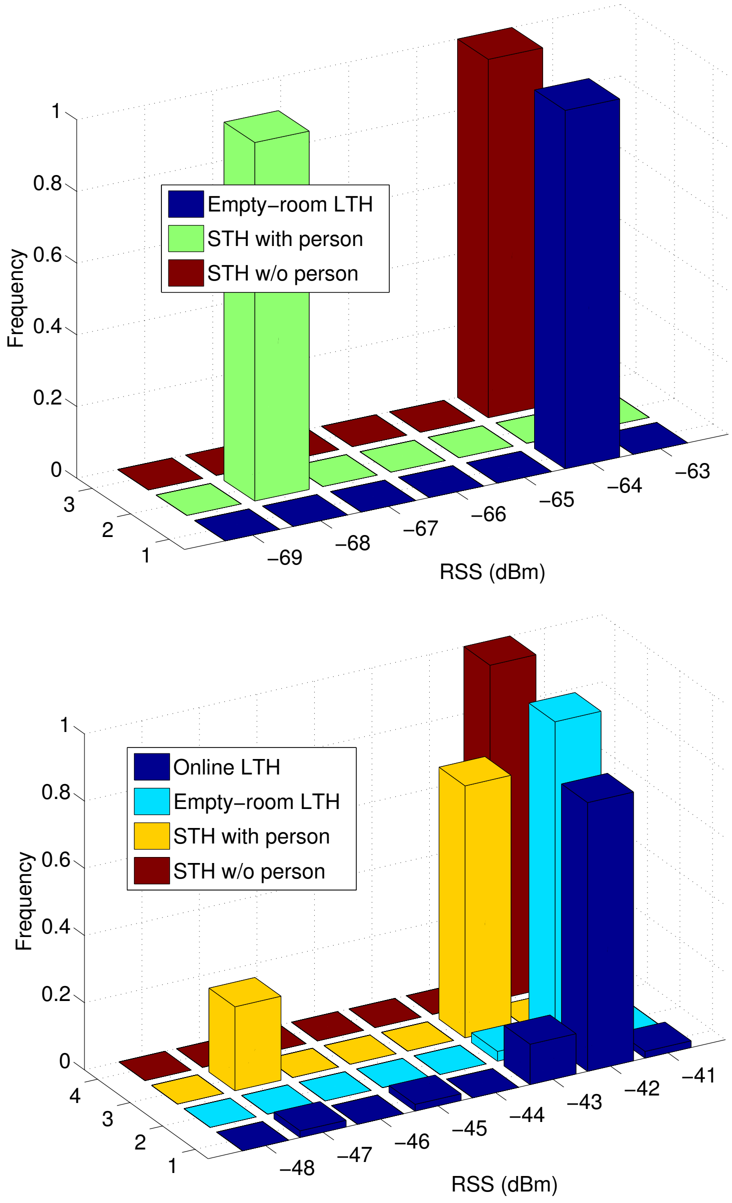

(a)

(b)

Figure 4.1: Long-term histogram (LTH) from offline calibration measurements and short-term histograms (STH) with and without (a) a stationary person; (b) a moving person.

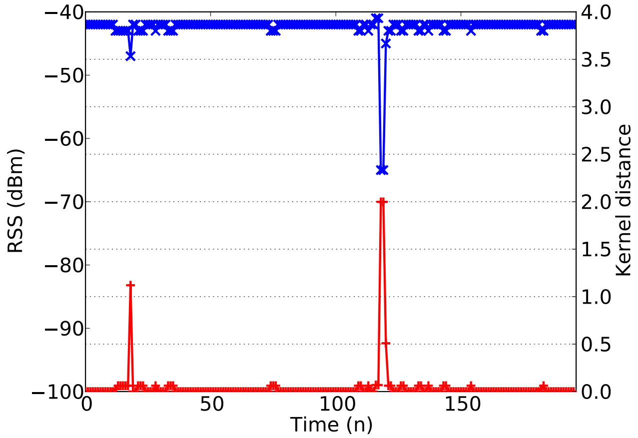

Figure 4.2: RSS (×) and kernel distance (+) time series for a link which a person crosses at $n = 23$ and $n = 120$.

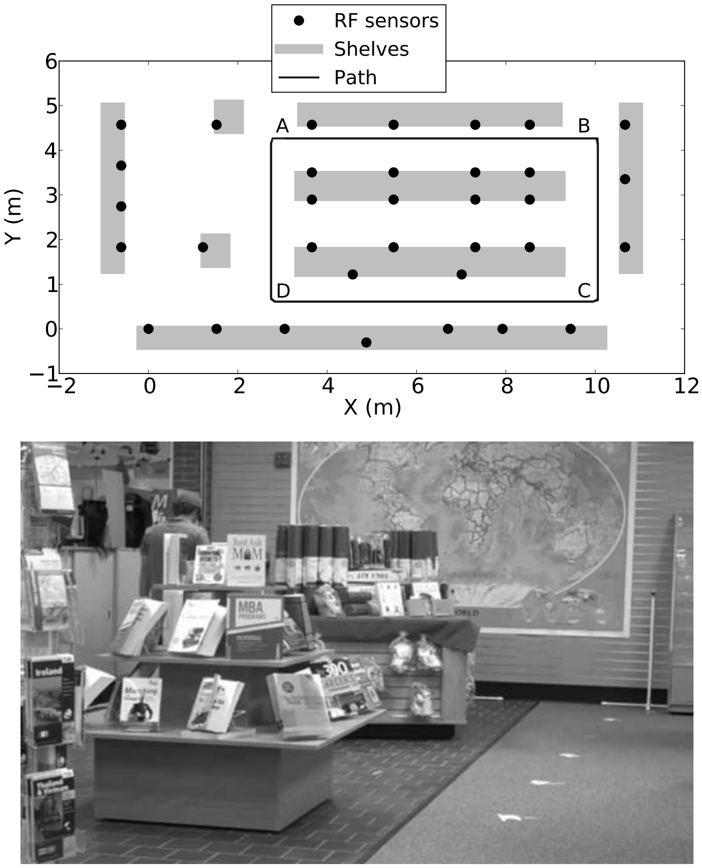

Figure 4.3: Experiment layout and environment of Experiment 5.

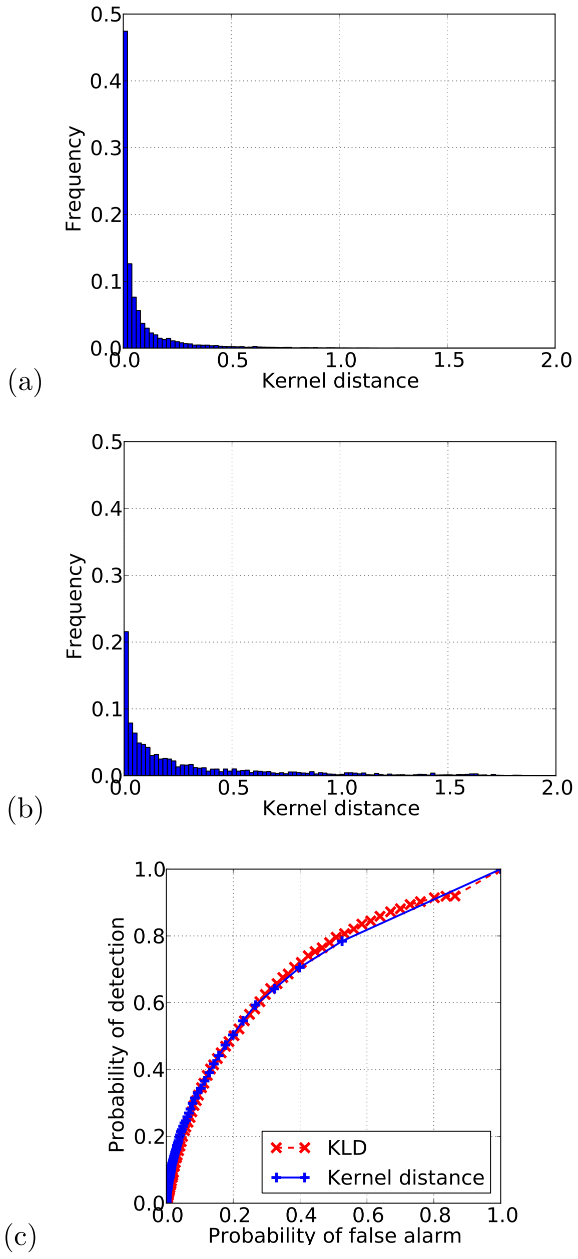

Figure 4.4: Detection results of using histogram distance to detect a person on link line or not (a) Kernel distance PDF from NPOLL; (b) Kernel distance PDF from POLL; (c) ROC curve.

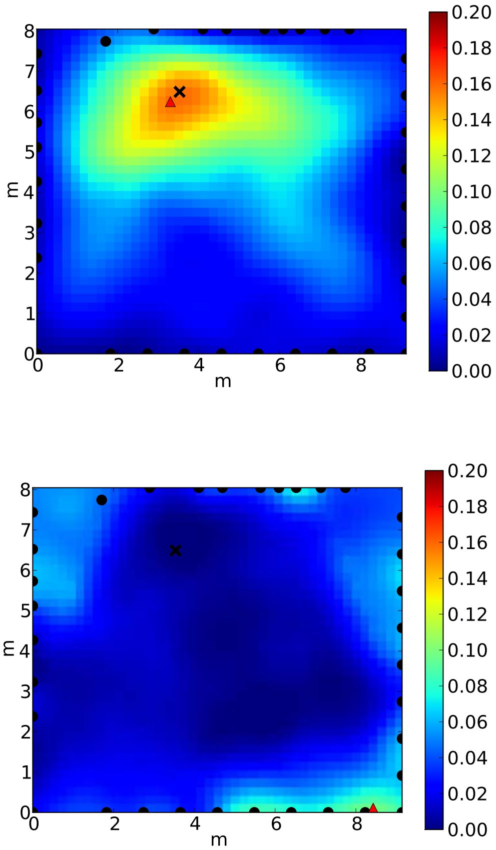

(a)

(b)

Figure 4.5: Imaging results of a stationary person (true location shown as ×) from (a) KRTI and (b) VRTI.

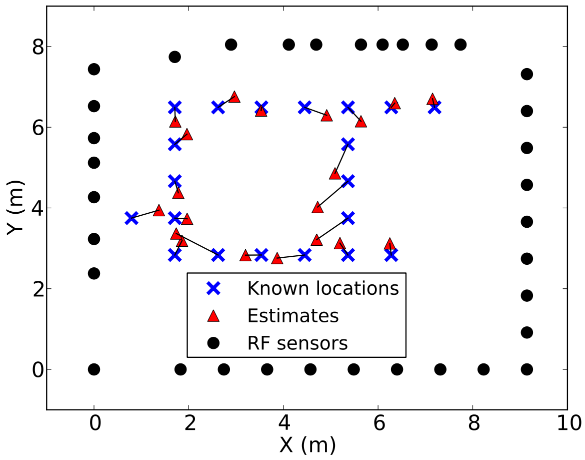

Figure 4.6: KRTI location estimates of a person standing at twenty locations.

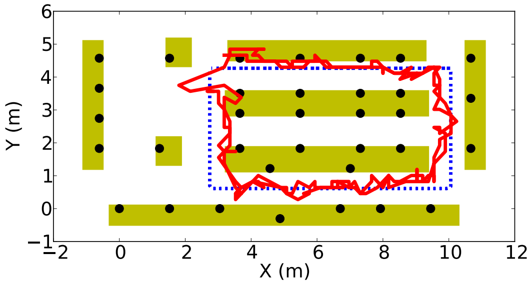

Figure 4.7: Kalman filter tracking results for Experiment 5 (true path shown as dash line).

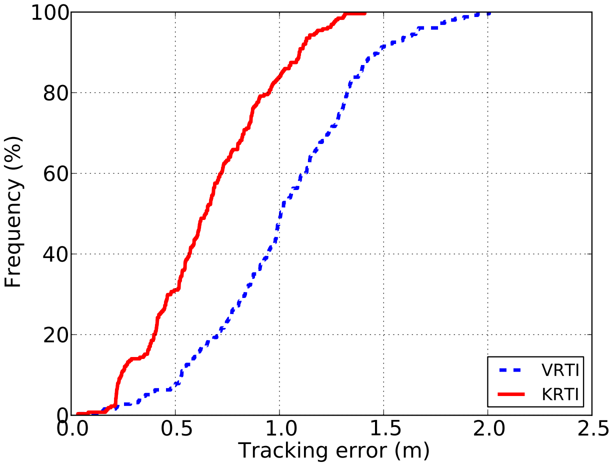

Figure 4.8: Kalman filter tracking CDFs from VRTI and KRTI for Experiment 5.

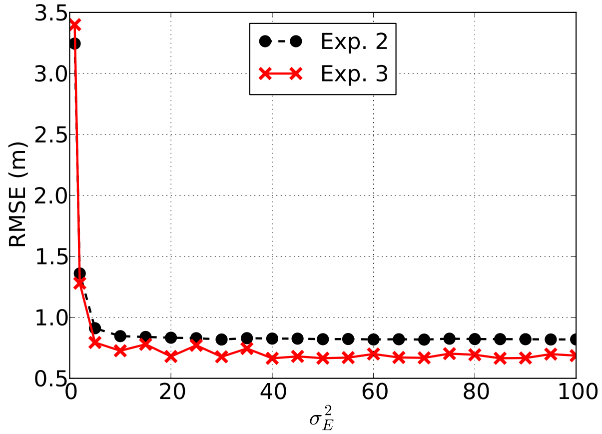

Figure 4.9: Kernel parameter σ_E^2 vs. RMSE from KRTI.

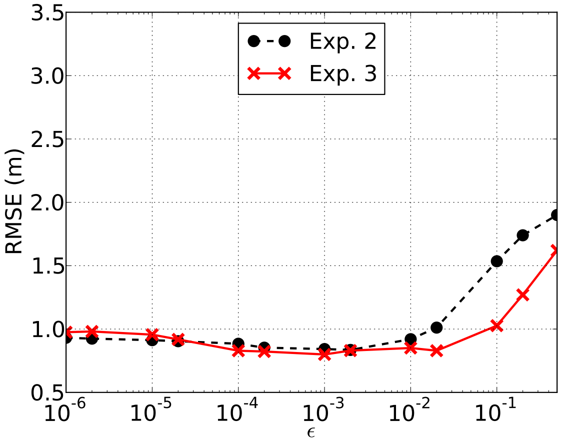

Figure 4.10: KLD parameter ϵ vs. RMSE from KRTI using KLD.

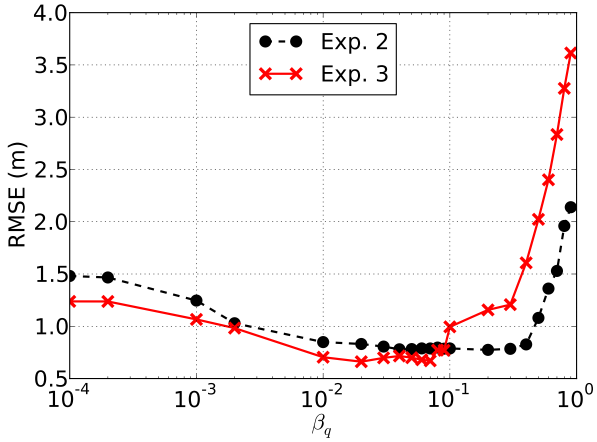

Figure 4.11: EWMA coefficient β_q vs. RMSE from KRTI.

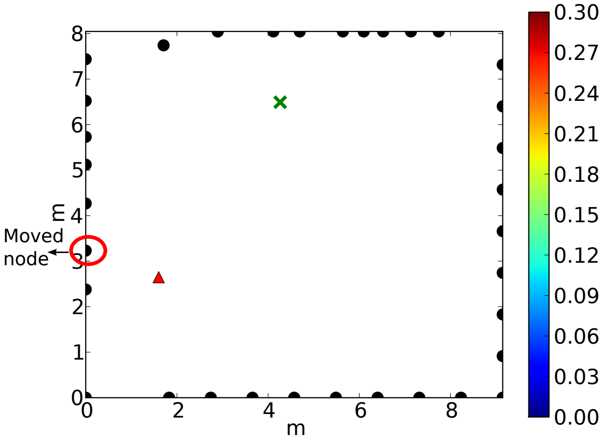

Figure 4.12: Effect of a moved node on KRTI when using the offline empty-room LTH.

Table 4.1: Experimental datasets.

Name	Task	Description
Exp.1	stationary person	calm day through-wall
Exp.2	moving person	calm day through-wall
Exp.3	moving person	windy day with fans
Exp.4	moving person	environment changes
Exp.5	moving person	at a cluttered bookstore

Table 4.2: Parameters used in detection and localization.

Parameter	Value	Description
σ^2	50	Regularization parameter
δ	2	Space parameter (m)
σ_E^2	30	Epanechnikov kernel width
ϵ	0.001	KLD parameter
β_q	0.05	EWMA factor for $\mathbf{v}$
β_p	0.9	EWMA factor for $\mathbf{u}$

Table 4.3: RMSEs of locating a moving person.

RMSE (m)	Exp. 2	Exp. 3	Exp. 4	Exp. 5
VRTI	0.70	2.12	1.46	1.09
SubVRT	0.65	1.05	1.14	1.08
KRTI	0.78	0.69	0.79	0.74

Table 4.4: RMSEs from KRTI using online IIR and offline FIR methods.

RMSE (m)	Exp. 2	Exp. 3	Exp. 4	Exp. 5
Offline FIR	1.49	0.74	5.02	0.74
Online EWMA	0.78	0.69	0.79	0.74

Table 4.5: Features of different NRES methods.

Features	RTI	VRTI	SMC	KRTI
Through-wall?	No	Yes	Yes	Yes
Online calibration?	No	NA	No	Yes
Stationary people?	Yes	No	Yes	Yes
Real-time?	Yes	Yes	No	Yes

CHAPTER 5

CONCLUSION

This dissertation is concluded with a summary of key research findings and opportunities for future work.

5.1 Key findings

For localization of a person in a wireless sensor network, the human body has a considerable effect on the RF signals transmitted from a radio device that the person is carrying. The human body also affects wireless measurements from links in the vicinity of the person. Both effects of the human presence are treated as "noise" in traditional real-time location systems and wireless communication systems. This dissertation aims at using the human body effects on radio signal and the correlated wireless measurements from many radio devices in a network to improve the performance of localization systems with or without requiring a person to carry radio devices. The key findings in radio device localization and device-free localization are summarized next.

5.1.1 Radio device localization

The first few key findings involve radio device localization in which the localization system requires people to wear active RFID badges. In many radio device localization experiments, we find that position estimates are often biased because of a non-isotropic gain pattern. If a person wears a transmitter badge on their chest, the position estimates from model-based maximum likelihood estimators (MLE) that assume isotropic gain pattern are often biased towards the directions that the person is facing. Essentially, the MLE estimates that the badge is closer to receivers that measure more power, and receivers in the direction the person is facing receive more power than would be predicted by an isotropic model. To remove the unrealistic isotropic gain pattern assumption in model-based localization, an empirical model for the directionality of a transmitter badge when worn by a person is proposed and verified based on measurements performed by five different people at two different indoor and outdoor environments. Based on this empirical gain pattern model, we find we can estimate the model parameters using only RSS measurements between anchor nodes and the badge. We propose a gain pattern estimator assuming the location of the badge is known. For joint position and gain pattern estimation, we propose an alternating gain and position estimation (AGAPE) algorithm to efficiently estimate both the position and orientation of a person wearing a badge in an RF sensor network. One might think that the introduction of an additional unknown gain pattern model would increase the lower bound of the variance of an estimator. We derive the Bayesian CRB [32] by including the gain pattern model parameters as nuisance parameters. We show that the CRB with an isotropic gain pattern assumption derived in [10] is a special case of the derived Bayesian CRB, and the introduction of a gain pattern model decreases the lower bound on the variance of a position estimator. After we have the location and orientation estimates of a person, we develop a novel Kalman filter which additionally tracks user orientation, and uses this to further improve coordinate tracking.

To summarize, the key findings in radio device localization are listed as follows:

- Find an empirical first-order gain pattern model that can represent the effect of the orientation (facing direction) of a human body on the RSS from a transmitter badge worn by the person based on the measurements performed in different environments.
- Propose a gain pattern estimator using only RSS measurements from a static wireless sensor network.
- Propose an alternating gain and position estimation (AGAPE) algorithm [1] to jointly estimate RFID badge location and badge gain pattern.
- Derive the Bayesian Cramér-Rao bound (CRB) [32] for the joint estimation problem. Comparison with CRB derived with an isotropic gain pattern assumption [10] shows that the accuracy of position estimates can be greatly improved by including orientation estimates in the localization system.
- Develop a robust tracking algorithm, orientation-enhanced extended Kalman filter (OE-EKF) that accepts orientation estimate as input to track mobile users in RF sensor networks.

5.1.2 Device-free localization

For device-free localization, the first few new findings are on the variance-based RTI. We know variance-based DFL systems including VRTI use the fact that human motion in the vicinity of a wireless link causes RSS variations to locate and track people in the area of the network. However, intrinsic motion, such as branches moving in the wind and rotating or vibrating machinery, also causes RSS variations which degrade the performance of a localization system.

The finding of the effect of intrinsic motion is from our inability to achieve the performance of 0.6 m average tracking error reported in [15]. In a repeat of the identical experiment at the same location and using the identical hardware, number of nodes, and software, VRTI does not always locate the person walking inside the house as accurately as reported in [15]. Investigation of the experimental data and video taken during the experiments indicates the reason for the degradation: intrinsic motion caused by periods of high wind.

Since intrinsic motion is an intrinsic part of an environment, we assume calibration measurements contain the type of intrinsic motion that we experience during the real-time operation. We use calibration measurements and propose two estimators to improve the robustness of VRTI. The first one uses the subspace decomposition method, which has been used in spectral estimation, sensor array processing, and network anomaly detection [62, 63, 64, 65]. We apply this method to VRTI, which leads to a new estimator we refer to as subspace variance-based radio tomography (SubVRT) [23]. Inspired by the fact that SubVRT makes use of the covariance matrix of link measurement and significantly reduces the impact of intrinsic motion, we also formulate a least squares (LS) solution [66] for VRTI which uses the inverse of the covariance matrix. We call this estimator least squares variance-based radio tomography (LSVRT). We find that by using the covariance matrix from the offline calibration measurements, both estimators are significantly more robust to intrinsic motion than VRTI. Experimental results show that both estimators reduce the RMSE of the location estimate by more than 40% compared to VRTI.

A new device-free localization system, which we call kernel distance-based RTI (KRTI) is another new finding in DFL. The motivation of this new DFL system is that many DFL systems cannot locate stationary people in a multipath-rich environment. Instead of using the absolute change and the variance of RSS measurement, we propose to use a new metric – the histogram difference between two RSS histograms to be able to locate both stationary and moving people. We explore different histogram difference metrics including the Kullback-Leibler divergence (KLD) [79] and we find the kernel distance is a good measure of histogram difference to locate people.

To be able to locate stationary people, KRTI requires an empty-room calibration as reference measurements, similar to shadowing-based RTI. However, a second finding of this work is that we find an empty-room calibration can be replaced with a "long-term histogram" which is calculated during localization operation, regardless of the presence or absence of people. By enabling online calibration, we allow the DFL system to operate without any empty-room calibration, and thus be used for emergency applications in which operators do not know *a priori* whether an area is empty or not. We show that simple filtering of online RSS measurements allows one to keep a long-term histogram in memory without significant computational complexity. This long-term histogram is close enough to the histogram which would have been measured in an empty-room calibration to perform as well as with empty-room calibration.

In summary, the findings of this dissertation on DFL include:

- Observe how intrinsic motion, such as motion of tree leaves, increases RSS variation in a way that is "noise" to a variance-based DFL system, and discover the noise has a spatial signature, which can be removed by the subspace decomposition method.
- Propose two robust estimators, subspace variance-based radio tomography [23] and least square variance-based radio tomography [30] to reduce the impact of the variations caused by intrinsic motion.
- Propose a new device-free localization method called kernel distance-based RTI [31], which uses the kernel distance between two RSS histograms (short-term histogram and long-term histogram) to locate both moving and stationary people. The exponentially weighted moving average is used on long-term histogram built during online period so that KRTI does not require "empty-room" offline calibration, and can be implemented without much computational complexity.

5.2 Future work

This dissertation explores locating people in sensor networks using both radio device localization method and device-free localization method. This section discusses the idea of combining these two methods and possible future work in radio tomographic localization.

5.2.1 Joint radio device and device-free localization

One suggestion for future work is joint radio device localization and device-free localization. Specifically, it is possible to combine the estimates from DFL with the AGAPE algorithm to better locate people wearing active RFID transmitter badges. The AGAPE algorithm developed in [1] is capable of estimating both the location of the orientation (facing direction) of people wearing transmitter badges in an outdoor environment. However, AGAPE suffers from an ambiguity problem. Since AGAPE has additional two parameters – people orientation and gain pattern directionality to estimate besides people location, severe multipath effects can cause AGAPE to converge to a wrong location estimate with a wrong orientation estimate in indoor environments. To solve this ambiguity problem, it is feasible to use location estimates from device-free localization methods, such as KRTI, in the AGAPE algorithm. Since the location estimate is confined, AGAPE can estimate both orientation and position without ambiguity in an indoor environment.

Since radio device localization like RFID localization provides identity of people carrying radio devices, combining radio device localization with DFL enables locating and identifying people for the multiple people localization scenario. For example, in the rescue scenario, joint radio device and device-free localization is capable of locating and identifying firefighters wearing RFID badges and victims without carrying any radio devices. However, it is difficult to identify victims from firefighters by only looking at the estimated RTI images. Another benefit of using estimates from DFL in radio device localization (AGAPE) is that additional information of a person's facing direction can be estimated as well. From a human activity recognition perspective, the orientation information of people is helpful in recognizing what kind of activities that people are doing. For example, if two people are facing to each other in a short distance in a hallway, it is more likely that a conversation is going on between them. Besides additional estimates of people's orientations, location estimates from radio device localization such as AGAPE and device-free localization like KRTI can be combined to improve the localization accuracy. While small scale fading has effects on both radio device localization and DFL, at certain environments with certain network configurations (i.e., topology and number of nodes), DFL may perform better than device-based localization, and at other conditions, it could be the opposite. It is an interesting future work to investigate in what kind of conditions, DFL outperforms radio device localization, and vice versa. Then certain data fusion method [82] can be used to adaptively combine two methods for a better estimate based on different environments and configurations.

However, practical issues also need to be addressed to combine two methods in real-world localization systems. As illustrated in Figure 1.2, all pairwise links of a network are used in a radio tomographic system. While for an emergency situation that does not last a long time, the energy consumption is not an important issue. Collecting all link measurements from a large network with hundreds or thousands of nodes would consume a lot of energy and is not practical for a real-time location system (RTLS) that is supposed to last for months or years without changing batteries for radio sensors. Thus, an energy-efficient way of performing DFL is also an interesting future research topic. Next, we focus on the future work particularly on DFL.

5.2.2 Future work in DFL

As an emerging technology, device-free localization using wireless sensor networks has many possible future research topics. Here, we only focus on model-based DFL method, that is, radio tomographic localization.

The major advantage of radio tomographic localization over fingerprint-based DFL method is that a statistical model is used to relate RSS measurements with the locations of the human motion or human presence so that it is not necessary to have a training period in which a person stands at each possible location in the network. However, the linear model used in radio tomographic localization is just an approximation of the real-world human motion or presence effects on RSS measurements. Recall the model as expressed in (1.3) in Chapter 1. Essentially the model tells us that if a person is inside an elliptical area, the human presence has certain effect (related to the link length and a scaling constant ϕ) on the link RSS measurement; if not, then the person has no effect on that link. Although this model is shown to be effective in both outdoor and indoor environments, the localization performance of RTI still has space to be improved in certain situations. For example, from many through-wall experiments performed at the same residential house, it is found that if a person walks close to a big TV set in the living room, the variance-based methods including VRTI, SubVRT and LSVRT cannot locate the person correctly within submeter accuracy. Thus, it is an important future research topic to investigate the possible use of other models in RTI. From previous RTI experiments, it is also found that the performance of radio tomographic localization could be very sensitive to the choice of the elliptical width parameter. At some environments, RTI performs better with a small elliptical width parameter; at other environments, a big value should be used to achieve the best localization performance. Thus it is important to be able to automatically choose model parameters of RTI in the future.

In this dissertation, two robust estimators SubVRT and LSVRT are developed to improve the robustness of the variance-based RTI. However, both estimators need offline empty-room calibration measurements. For practical applications, especially in emergency and rescue situations, an empty-room calibration is often not available. To be able to use the two robust estimators in those scenarios, it is necessary to identify the intrinsic motion from online calibration period, in which people are present in the area. A recent study has used background subtraction techniques from computer vision field to perform online calibration of baseline RSS measurements in RF sensor networks [83]. Various background subtraction methods are investigated including background subtraction with temporal background modeling, foreground-adaptive background subtraction, and foreground-adaptive background subtraction with Markov modeling of change labels. Thus, it is a possible future research topic to use online calibration to capture intrinsic motion with the help of these background subtraction methods.

Finally, in many indoor experiments, we have observed that if we place radio nodes on the surface of walls with their radio antennas very close to the walls (almost touching the walls), then the performance of RTI is not as good as when we place nodes a few inches away from the walls. Sometimes RTI does not work at all if all radio nodes are too close to the walls. A reasonable explanation is that walls can significantly change the gain pattern of the radio antenna if the walls are in the near field of the antenna. As investigated in Chapter 2 of the dissertation, if an active RFID node is worn by a person as a badge, the human body significantly changes the gain pattern of the RFID node. Thus, for walls built with concrete, the same effect happens to the radio nodes attached onto the walls. While in RTI experiments and demonstrations, we can always place radio nodes a little further away from the walls or any big obstacles, in real applications, it is convenient to simply plug radio nodes to the power outlet on walls. For some applications such as surveillance and monitoring, it is even desirable to place radio sensors inside walls so that intruders and attackers cannot find them and the system is protected from possible attacks. Thus, it is an important future topic to study how to remove or even use the effect of walls on the gain pattern of radio nodes to improve the sensing ability and localization performance of a radio tomographic system.

APPENDIX

DERIVATION OF INFORMATION MATRIX

A.1 Derivation of information matrix

We derive the information matrix $\boldsymbol{I_\theta}$ expressed in (19) in Section 3.6.1 of this submission.

As an example, we derive the first element $[\boldsymbol{I_\theta}]_{11}$. From (19), we see $[\boldsymbol{I_\theta}]_{11} = [I_D]_{11} + [I_P]_{11}$. So first, we calculate $[I_D]_{11}$ from (17).

The second derivative of the log-likelihood function w.r.t. x_t is written as:

$$\frac{\partial^2 \ln f_D}{\partial x_t^2} = \frac{1}{\sigma^{2N}} \sum_{i=0}^{N-1} \left[(P_i - \mu)\frac{\partial^2 \mu}{\partial x_t^2} - \left(\frac{\partial \mu}{\partial x_t}\right)^2 \right] \tag{A.1}$$

where μ is short for $\mu(\boldsymbol{\theta}) = P_0 - 10n_p \log_{10}(\frac{d_i}{d_0}) + g(\alpha_i)$.

Because $E_D\left[P_i - \mu\right] = 0$, the expectation w.r.t. data E_D of the above second derivative becomes:

$$E_D\left[\frac{\partial^2 \ln f_D}{\partial x_t^2}\right] = -\frac{1}{\sigma^{2N}} \sum_{i=0}^{N-1} E_D\left[\left(\frac{\partial \mu}{\partial x_t}\right)^2\right]. \tag{A.2}$$

The first derivative of μ to x_t in (A.2) is:

$$\frac{\partial \mu}{\partial x_t} = -\left(c\frac{\Delta x_i}{d_i^2} + T(G)\right) \tag{A.3}$$

where $T(G) = G_I\left(\frac{\Delta x_i^2}{d_i^3} - \frac{1}{d_i}\right) + G_Q\frac{\Delta x_i \Delta y_i}{d_i^3}$, $c = 10\frac{n_p}{\ln 10}$, $\Delta x_i = x_i - x_t$, and $\Delta y_i = y_i - y_t$.

Next, we take the expectation w.r.t. prior knowledge E_P to (A.2), and we have:

$$\begin{aligned}[I_D]_{11} &= E_P\left[E_D\left(\frac{\partial^2 \ln f_D}{\partial x_t^2}\right)\right] \\ &= \frac{1}{\sigma^{2N}}\left[\left(c\frac{\Delta x_{it}}{d_i^2}\right)^2 + f_1(g)\right]\end{aligned} \tag{A.4}$$

where

$$f_1(g) = \sigma_G^2\left(\frac{1}{d_i^2} + \frac{\Delta x_i^4}{d_i^6} + \frac{\Delta x_i^2 \Delta y_i^2}{d_i^6} - 2\frac{\Delta x_i^2}{d_i^4}\right).$$

Since we have no prior knowledge of x_t, $[I_P]_{11} = 0$. Thus the first element of the information matrix $[I_{\boldsymbol{\theta}}]_{11}$ becomes:

$$[I_{\boldsymbol{\theta}}]_{11} = \frac{1}{\sigma^{2N}} \left[\left(c\frac{\Delta x_{it}}{d_i^2} \right)^2 + f_1(g) \right]. \tag{A.5}$$

The other elements of the information matrix can be derived in a similar manner. One difference in deriving $[I_{\boldsymbol{\theta}}]_{mn}$ for $m \in \{3,4\}$ and $n \in \{3,4\}$ is $[I_P]_{mn}$ is non-zero, because prior knowledge of G_I and G_Q is available. For example, $[I_P]_{33}$ is:

$$[I_P]_{33} = -E_P \left(\frac{\partial^2 \ln f_P}{\partial G_I^2} \right) = \frac{1}{\sigma_G^2}. \tag{A.6}$$

Finally, since the information matrix is symmetric, all the elements in the upper triangular of the information matrix are listed in the following:

$$[I_{\boldsymbol{\theta}}]_{11} = \frac{1}{\sigma^{2N}} \sum_{i=0}^{N-1} \left[\left(c\frac{\Delta x_i}{d_i^2} \right)^2 + f_1(g) \right] \tag{A.7}$$

$$[I_{\boldsymbol{\theta}}]_{12} = \frac{1}{\sigma^{2N}} \sum_{i=0}^{N-1} \left[\left(c\frac{\Delta x_i}{d_i^2} \right) \left(c\frac{\Delta y_i}{d_i^2} \right) + f_2(g) \right] \tag{A.8}$$

$$[I_{\boldsymbol{\theta}}]_{13} = \frac{1}{\sigma^{2N}} \sum_{i=0}^{N-1} \left(c\frac{\Delta x_i}{d_i^2} \right) \left(\frac{\Delta x_i}{d_i} \right) \tag{A.9}$$

$$[I_{\boldsymbol{\theta}}]_{14} = \frac{1}{\sigma^{2N}} \sum_{i=0}^{N-1} \left(c\frac{\Delta x_i}{d_i^2} \right) \left(\frac{\Delta y_i}{d_i} \right) \tag{A.10}$$

$$[I_{\boldsymbol{\theta}}]_{22} = \frac{1}{\sigma^{2N}} \sum_{i=0}^{N-1} \left[\left(c\frac{\Delta y_i}{d_i^2} \right)^2 + f_3(g) \right] \tag{A.11}$$

$$[I_{\boldsymbol{\theta}}]_{23} = \frac{1}{\sigma^{2N}} \sum_{i=0}^{N-1} \left(c\frac{\Delta y_i}{d_i^2} \right) \left(\frac{\Delta x_i}{d_i} \right) \tag{A.12}$$

$$[I_{\boldsymbol{\theta}}]_{24} = \frac{1}{\sigma^{2N}} \sum_{i=0}^{N-1} \left(c\frac{\Delta y_i}{d_i^2} \right) \left(\frac{\Delta y_i}{d_i} \right) \tag{A.13}$$

$$[I_{\boldsymbol{\theta}}]_{33} = \frac{1}{\sigma^{2N}} \sum_{i=0}^{N-1} \left(\frac{\Delta x_i}{d_i} \right)^2 + \frac{1}{\sigma_G^2} \tag{A.14}$$

$$[I_{\boldsymbol{\theta}}]_{34} = \frac{1}{\sigma^{2N}} \sum_{i=0}^{N-1} \frac{\Delta x_i}{d_i} \frac{\Delta y_i}{d_i} \tag{A.15}$$

$$[I_{\boldsymbol{\theta}}]_{44} = \frac{1}{\sigma^{2N}} \sum_{i=0}^{N-1} \left(\frac{\Delta y_i}{d_i} \right)^2 + \frac{1}{\sigma_G^2} \tag{A.16}$$

where

$$f_2(g) = \sigma_G^2 \left(\frac{\Delta x_i^3 \Delta y_i}{d_i^6} + \frac{\Delta y_i^3 \Delta x_i}{d_i^6} - 2\frac{\Delta x_i \Delta y_i}{d_i^4} \right)$$

$$f_3(g) = \sigma_G^2 \left(\frac{1}{d_i^2} + \frac{\Delta y_i^4}{d_i^6} + \frac{\Delta x_i^2 \Delta y_i^2}{d_i^6} - 2\frac{\Delta y_i^2}{d_i^4} \right).$$

REFERENCES

[1] Y. Zhao, N. Patwari, P. Agrawal, and M. G. Rabbat, "Directed by directionality: Benefiting from the gain pattern of active RFID badges," *IEEE Transactions on Mobile Computing*, vol. 11, pp. 865–877, May 2012.

[2] P. Bahl and V. N. Padmanabhan, "RADAR: an in-building RF-based user location and tracking system," in *IEEE Int. Conf. Computer Communications*, Tel Aviv, Israel, 2000, pp. 775–784.

[3] A. Savvides, C. Han, and M. Strivastava, "Dynamic fine-grained localization in ad-hoc networks of sensors," in *Proc. 7th int. conf. Mobile computing and networking*, Rome, Italy, 2001, pp. 166–179.

[4] N. Patwari, J. Ash, S. Kyperountas, R. M. Moses, A. O. Hero III, and N. S. Correal, "Locating the nodes: Cooperative localization in wireless sensor networks," *IEEE Signal Process.*, vol. 22, no. 4, pp. 54–69, July 2005.

[5] TelosB mote website. http://www.memsic.com/products/wireless-sensor-networks/wireless-modules.html.

[6] TI CC2531 USB dongle website. http://www.ti.com/tool/cc2531emk.

[7] Sensing and Processing Across Networks (SPAN) Lab, Spin website. http://span.ece.utah.edu/spin.

[8] G. Mao, B. Fidan, and B. D. O. Anderson, "Wireless sensor network localization techniques," *Comput. Networks*, vol. 51, no. 10, pp. 2529–2553, 2007.

[9] *IEEE Standard for Information Technology - Telecommunications and Information Exchange Between Systems - Local and Metropolitan Area Networks - Specific Requirement. Part 11: Wireless LAN Medium Access Control (MAC) and Physical Layer (PHY) specifications: Higher-Speed Physical Layer Extension in the 2.4 GHz Band.* IEEE Std 802.11, 1999.

[10] N. Patwari, A. O. Hero III, M. Perkins, N. Correal, and R. J. O'Dea, "Relative location estimation in wireless sensor networks," *IEEE Trans. Signal Process.*, vol. 51, no. 8, pp. 2137–2148, Aug. 2003.

[11] T. S. Rappaport, *Wireless Communications: Principles and Practice.* New Jersey: Prentice-Hall Inc., 1996.

[12] C. Chang and A. Sahai, "Object tracking in a 2D UWB sensor network," in *38th Asilomar Conf. Signals, Systems and Computers*, Pacific Grove, CA, 2004, pp. 1252–1256.

[13] L.-P. Song, C. Yu, and Q. H. Liu, "Through-wall imaging (TWI) by radar: 2-D tomographic results and analyses," *IEEE Transactions on Geoscience and Remote Sensing*, vol. 43, no. 12, pp. 2793–2798, Dec. 2005.

[14] M. Youssef, M. Mah, and A. Agrawala, "Challenges: device-free passive localization for wireless environments," in *ACM Int. Conf. Mobile Computing and Networking*, Montréal, Québec, Canada, 2007, pp. 222–229.

[15] J. Wilson and N. Patwari, "See-through walls: Motion tracking using variance-based radio tomography networks," *IEEE Transactions on Mobile Computing*, vol. 10, no. 5, pp. 612–621, May 2011.

[16] ——, "A fade level skew-laplace signal strength model for device-free localization with wireless networks," *IEEE Transactions on Mobile Computing*, vol. 11, pp. 947 – 958, June 2012.

[17] K. Woyach, D. Puccinelli, and M. Haenggi, "Sensorless Sensing in Wireless Networks: Implementation and Measurements," in *2nd Int. Workshop Wireless Network Measurement*, Boston, MA, 2006, pp. 1–8.

[18] D. Zhang, J. Ma, Q. Chen, and L. M. Ni, "An RF-based system for tracking transceiver-free objects," in *5th IEEE Int. Conf. Pervasive Computing and Communications*, White Plains, New York, 2007, pp. 135–144.

[19] M. Moussa and M. Youssef, "Smart services for smart environments: Device-free passive detection in real environments," in *IEEE Int. Conf. Pervasive Computing and Communications*, Galveston, Texas, 2009, pp. 1–6.

[20] M. Seifeldin and M. Youssef, "Nuzzer: A large-scale device-free passive localization system for wireless environments," Arxiv.org, Tech. Rep. arXiv:0908.0893, Aug. 2009.

[21] C. Xu, B. Firner, Y. Zhang, R. Howard, J. Li, and X. Lin, "Improving RF-based device-free passive localization in cluttered indoor environments through probabilistic classification methods," in *Proc. 11th Int. Conf. Information Processing in Sensor Networks*, 2012, pp. 209–220.

[22] J. Wilson and N. Patwari, "Radio tomographic imaging with wireless networks," *IEEE Transactions on Mobile Computing*, vol. 9, no. 5, pp. 621–632, May 2010.

[23] Y. Zhao and N. Patwari, "Noise reduction for variance-based device-free localization and tracking," in *Proc. IEEE 8th Conf. Sensor, Mesh and Ad Hoc Communications and Networks*, Salt Lake City, Utah, June 2011.

[24] O. Kaltiokallio and M. Bocca, "Real-time intrusion detection and tracking in indoor environment through distributed RSSI processing," in *IEEE 17th Int. Conf. Embedded and Real-Time Computing Systems and Applications*, Toyama, Japan, 2011, pp. 61–70.

[25] M. A. Kanso and M. G. Rabbat, "Compressed RF tomography for wireless sensor networks: Centralized and decentralized approaches," in *IEEE 5th Int. Conf. Distributed Computing in Sensor Systems*, Marina Del Rey, CA, June 2009, pp. 173 – 186.

[26] X. Chen, A. Edelstein, Y. Li, M. Coates, M. Rabbat, and A. Men, "Sequential monte carlo for simultaneous passive device-free tracking and sensor localization using received signal strength measurements," in *Proc. ACM/IEEE Int. Conf. Information Processing in Sensor Networks*, Chicago, U.S., 2011, pp. 342 – 353.

[27] Y. Zhao and N. Patwari, “Robust estimators for variance-based device-free localization and tracking,” Arxiv.org, Tech. Rep. arXiv:1110.1569v1, Oct. 2011.

[28] ——, “Histogram distance-based radio tomographic localization,” in *Proc. 11th int. conf. Information Processing in Sensor Networks*, Beijing, China, 2012, pp. 129–130.

[29] J. M. Phillips and S. Venkatasubramanian, “A gentle introduction to the kernel distance,” Arxiv.org, Tech. Rep. arXiv:1103.1625, 2011.

[30] Y. Zhao and N. Patwari, “Robust estimators for variance-based device-free localization and tracking,” *IEEE Transactions on Signal Processing*, August 2011, (submitted).

[31] Y. Zhao, N. Patwari, J. M. Phillips, and S. Venkatasubramanian, “Radio tomographic imaging and tracking of stationary and moving people via histogram difference,” in *The 8th International Conference on emerging Networking EXperiments and Technologies (CoNEXT)*, June 2012, (submitted).

[32] H. L. Van Trees, *Detection, Estimation, and Modulation Theory, Part I.* John Wiley & Sons, 1968.

[33] Y. Zhao and N. Patwari, “Noise reduction for variance-based radio tomographic localization,” in *Proc. IEEE 8th Conf. Sensor, Mesh and Ad Hoc Communications and Networks*, Salt Lake City, Utah, June 2011.

[34] M. Jensen and Y. Rahmat-Samii, “EM interaction of handset antennas and a human in personal communications,” *Proceedings of the IEEE*, vol. 83, no. 1, pp. 7–17, 1995.

[35] J. Griffin and G. Durgin, “Complete link budgets for backscatter radio and RFID systems,” *IEEE Antennas and Propagation Magazine*, vol. 51, no. 2, pp. 11–25, 2009.

[36] T. King, S. Kopf, T. Haenselmann, C. Lubberger, and W. Effelsberg, “COMPASS: A probabilistic indoor positioning system based on 802.11 and digital compasses,” in *Proc. 1st Int. Workshop Wireless network testbeds, experimental evaluation and characterization*, Los Angeles, CA, 2007, pp. 34 – 40.

[37] T. Roos, P. Myllymki, H. Tirri, P. Misikangas, and J. Sievnen, “A probabilistic approach to WLAN user location estimation,” *International Journal of Wireless Information Networks*, vol. 9, no. 3, pp. 155–164, 2002.

[38] A. Ladd, K. Bekris, G. Marceau, A. Rudys, L. Kavraki, and D. Wallach, “Robotics-based location sensing using wireless ethernet,” in *ACM Conf. Mobile Computing and Networking*, Atlanta, Georgia, 2002, pp. 227–238.

[39] A. Howard, S. Siddiqi, and G. Sukhatme, “An experimental study of localization using wireless ethernet,” in *Proc. Int. Conf. Field and Service Robotics*, Mt. Fuji, Japan, 2003, pp. 201–206.

[40] K. Kaemarungsi and P. Krishnamurthy, “Properties of indoor received signal strength for WLAN location fingerprinting,” in *Proc. 1st Int. Conf. Mobile and Ubiquitous Systems: Networking and Services*, Boston, Massachusetts, 2004, pp. 14–23.

[41] A. Awad, T. Frunzke, and F. Dressler, “Adaptive distance estimation and localization in wsn using rssi measures,” in *10th EUROMICRO Conf. Digital System Design - Architectures, Methods and Tools*, Lübeck, Germany, 2007, pp. 471–478.

[42] W. L. Stutzman and G. A. Theile, *Antenna Theory and Design.* John Wiley & Sons, 1981.

[43] A. V. Oppenheim and R. W. Schafer, *Discrete-time Signal Processing.* Prentice Hall, 2009.

[44] *CC2431: System-on-Chip for 2.4 GHz ZigBee / IEEE 802.15.4 with Location Engine*, Sept. 2005.

[45] N. Lomb, "Least-squares frequency analysis of unequally spaced data," *Astrophysics and space science*, pp. 447–462, 1976.

[46] A. Gunawardana and W. Byrne, "Convergence theorems for generalized alternating minimization procedures," *Journal of machine learning research*, vol. 6, pp. 2049–2073, 2005.

[47] S. Miller and D. Childers, *Probability and Random Processes: With Applications to Signal Processing and Communications.* Academic Press, 2004.

[48] S. M. Kay, *Fundamentals of Statistical Signal Processing.* New Jersey: Prentice Hall, 1993.

[49] M. Friedmann, T. Stamer, and A. Pentland, "Device synchronization using an optimal linear filter," in *Symp. Interactive 3D Graphics*, Cambridge, Massachusetts, 1992, pp. 57–62.

[50] K. Yedavalli, B. Krishnamachari, S. Ravula, and B. Srinivasan, "Ecolocation: A sequence based technique for RF-only localization in wireless sensor networks," in *Proc. 4th Int. Conf. Information Processing in Sensor Networks*, Los Angeles, CA, 2005.

[51] D. Kotz, C. Newport, and C. Elliott, "The mistaken axioms of wireless-network research," Dept. of Computer Science, Dartmouth College, Tech. Rep. TR2003-467, July 2003.

[52] G. Zhou, T. He, S. Krishnamurthy, and J. Stankovic, "Impact of radio irregularity on wireless sensor networks," in *Proc. 2nd Int. Conf. Mobile Systems, Applications, and Services*, Boston, Massachusetts, 2004, pp. 125–138.

[53] C. Röhrig and F. Künemund, "Estimation of position and orientation of mobile systems in a wireless LAN," in *Proc. 46th IEEE Conf. Decision and Control*, New Orleans, Louisiana, 2007, pp. 4932–4937.

[54] I.-E. Liao and K.-F. Kao, "Enhancing the accuracy of WLAN-based location determination systems using predicted orientation information," *Information Sciences*, vol. 178, pp. 1049–1068, 2008.

[55] N. Patwari and J. Wilson, "RF sensor networks for device-free localization: Measurements, models and algorithms," *Proceedings of the IEEE*, vol. 98, no. 11, pp. 1961–1973, Nov. 2010.

[56] M. C. Wicks, "RF tomography with application to ground penetrating radar," in *41st Asilomar Conf. Signals, Systems and Computers*, Pacific Grove, CA, 2007, pp. 2017–2022.

[57] A. M. Haimovich, R. S. Blum, and L. J. Cimini, “MIMO radar with widely separated antennas,” *IEEE Signal Processing*, vol. 25, no. 1, pp. 116–129, Jan. 2008.

[58] F. Viani, L. Lizzi, P. Rocca, M. Benedetti, M. Donelli, and A. Massa, “Object tracking through RSSI measurements in wireless sensor networks,” *IEE Electronics Letters*, vol. 44, no. 10, pp. 653–654, 2008.

[59] F. Viani, P. Rocca, G. Oliveri, D. Trinchero, and A. Massa, “Localization, tracking, and imaging of targets in wireless sensor networks: An invited review,” *Radio Science*, vol. 46, no. 5, 2010.

[60] B. Sklar, “Rayleigh fading channels in mobile digital communication systems .i. characterization,” *IEEE Communications Magazine*, vol. 35, no. 7, pp. 90–100, July 1997.

[61] G. D. Durgin, *Space-Time Wireless Channels.* Prentice Hall PTR, 2002.

[62] P. Stoica and R. L. Moses, *Introduction to Spectral Analysis.* New Jersey: Prentice-Hall Inc., 1997.

[63] R. Schmidt, “Multiple emitter location and signal parameter estimation,” *IEEE Transactions on Antennas and Propagation*, vol. 34, pp. 276–280, March 1986.

[64] R. Roy and T. Kailath, “ESPRIT - estimation of signal parameters via rotational invariance techniques,” *IEEE Transactions on Acoustics, Speech, and Signal Processing*, vol. 37, no. 7, pp. 984–995, July 1989.

[65] A. Lakhina, M. Crovella, and C. Diot, “Diagnosing network-wide traffic anomalies,” in *ACM SIGCOMM*, Portland, Oregon, 2004, pp. 219–230.

[66] A. Tarantola, *Inverse Problem Theory and Methods for Model Parameter Estimation.* Society for Industrial and Applied Mathematics, 2004.

[67] I. Jolliffe, *Principal Component Analysis*, 2nd ed. Springer-Verlag New York, 2002.

[68] M. Turk and A. Pentland, “Eigenfaces for recognition,” *Journal of Cognitive Neuroscience*, vol. 3, no. 1, pp. 71–86, 1991.

[69] G. Xu and T. Kailath, “Fast subspace decomposition,” *IEEE Transactions on Signal Processing*, vol. 42, no. 3, pp. 539–551, March 1994.

[70] O. Ledoit and M. Wolf, “A well-conditioned estimator for large-dimensional covariance matrices,” *Journal of multivariate analysis*, vol. 88, pp. 365–411, February 2004.

[71] Y. Chen, A. Wiesel, Y. C. Eldar, and A. O. Hero III, “Shrinkage algorithms for MMSE covariance estimation,” *IEEE Transactions on Signal Processing*, vol. 58, no. 10, pp. 5016–5029, October 2010.

[72] P. Agrawal and N. Patwari, “Correlated link shadow fading in multi-hop wireless networks,” *IEEE Trans. Wireless Commun.*, vol. 8, no. 8, pp. 4024–4036, Aug. 2009.

[73] Sensing and Processing Across Networks (SPAN) Lab, RTI website. http://span.ece.utah.edu/radio-tomographic-imaging.

[74] Y. Mostofi, “Compressive cooperative sensing and mapping in mobile networks,” *IEEE Transactions on Mobile Computing*, vol. 10, no. 12, pp. 1769–1784, December 2011.

[75] L. Rabiner, “A tutorial on hidden markov models and selected applications in speech recognition,” *Proceedings of the IEEE*, vol. 77, no. 2, pp. 257–286, Feburary 1989.

[76] N. Patwari and P. Agrawal, “Effects of correlated shadowing: Connectivity, localization, and rf tomography,” in *IEEE/ACM Int. Conf. on Information Processing in Sensor Networks*, St. Louis, Missouri, 2008, pp. 82–93.

[77] M. A. Kanso and M. G. Rabbat, “Efficient detection and localization of assets in emergency situations,” in *3rd Intl. Symp. Medical Information and Communication Technology*, Montréal, Québec, Feb. 2009.

[78] A. Gretton, K. Borgwardt, M. Rasch, B. Scholkopf, and A. Smola, “A kernel method for the two-sample problem,” arXiv.org, Tech. Rep. arXiv:0805.2368, 2008.

[79] T. Cover and J. A. Thomas, *Elements of Information Theory.* John Wiley & Sons, 1991.

[80] S. Joshi, R. V. Kommaraji, J. M. Phillips, and S. Venkatasubramanian, “Comparing distributions and shapes using the kernel distance,” in *Proc. 27th ACM Symp. Computational geometry*, Paris, France, 2011, pp. 47–56.

[81] D. Comaniciu and P. Meer, “Mean shift: A robust approach toward feature space analysis,” *IEEE Transactions on Pattern Analysis and Machine Intelligence*, vol. 24, no. 5, pp. 603–619, 2002.

[82] D. Hall and J. Llinas, “An introduction to multisensor data fusion,” *Proceedings of the IEEE*, vol. 85, no. 1, pp. 6–23, 1997.

[83] A. Edelstein and M. Rabbat, “Background subtraction for online calibration of baseline rss in rf sensing networks,” arXiv.org, Tech. Rep. arXiv:1207.1137v1, July 2012.